INVESTIGATING FORWARD FLIGHT MULTIROTOR WIND TUNNEL TESTING IN A 3-BY 4-FOOT WIND TUNNEL

A Thesis

presented to

the Faculty of California Polytechnic State University,

San Luis Obispo

In Partial Fulfillment

of the Requirements for the Degree

Master of Science in Aerospace Engineering

by

Reed Danis

June 2018

COMMITTEE MEMBERSHIP

TITLE:	Investigating Forward Flight Multirotor Wind Tunnel Testing in a 3-by 4-foot Wind Tunnel
AUTHOR:	Reed Anthony Danis
DATE SUBMITTED:	June 2018
COMMITTEE CHAIR:	Graham Doig, Ph.D. Professor of Aerospace Engineering
COMMITTEE MEMBER:	Robert McDonald, Ph.D. Head of Vehicle Engineering (Elevate), Uber
COMMITTEE MEMBER:	Aaron Drake, Ph.D. Professor of Aerospace Engineering
COMMITTEE MEMBER:	Russell Westphal, Ph.D. Professor of Mechanical Engineering

ABSTRACT

Investigating Forward Flight Multirotor Wind Tunnel Testing in a 3-by 4-foot Wind Tunnel

Reed Anthony Danis

Investigation of complex multirotor aerodynamic phenomena via wind tunnel experimentation is becoming extremely important with the rapid progress in advanced distributed propulsion VTOL concepts. Much of this experimentation is being performed in large, highly advanced tunnels. However, the proliferation of this class of vehicles extends to small aircraft used by small businesses, universities, and hobbyists without ready access to this level of test facility. Therefore, there is a need to investigate whether multirotor vehicles can be adequately tested in smaller wind tunnel facilities. A test rig for a 2.82-pound quadcopter was developed to perform powered testing in the Cal Poly Aerospace Department's Low Speed Wind Tunnel, equipped with a 3-foot tall by 4-foot wide test section. The results were compared to data from similar tests performed in the U.S. Army 7-by 10-ft Wind Tunnel at NASA Ames. The two data sets did not show close agreement in absolute terms but demonstrated similar trends. Due to measurement uncertainties, the contribution of wind tunnel interference effects to this discrepancy in measurements was not able to be properly quantified, but is likely a major contributor. Flow visualization results demonstrated that tunnel interference effects can likely be minimized by testing at high tunnel speeds with the vehicle pitched 10-degrees or more downward. Suggestions towards avoiding the pitfalls inherent to multirotor wind tunnel testing are provided. Additionally, a modified form of the conventional lift-to-drag ratio is presented as a metric of electric multirotor aerodynamic efficiency.

Keywords: Electric Propulsion, Distributed Propulsion, Multirotor, Quadcopter, Wind Tunnel Testing

TABLE OF CONTENTS

Page

LIST OF TABLES

Table Page

LIST OF FIGURES

Figure Page

NOMENCLATURE

BEMF	=	back electromotive force
BLDC	=	brushless DC motor
CFD	=	computational fluid dynamics
CG	=	center of gravity
COTS	=	commercial off-the-shelf
CSR	=	current sense resistor
D	=	drag, lbs
DAQ	=	data acquisition
DC	=	direct current
ESC	=	electronic speed controller
f	=	frequency, Hz
FFT	=	fast Fourier transform
F_X	=	force along the wind tunnel reference frame X-axis
F_Y	=	force along the wind tunnel reference frame Y-axis
F_Z	=	force along the wind tunnel reference frame Z-axis
I	=	current, A
L	=	lift, lbs
L/D	=	conventional lift-to-drag ratio
$L/D\|_{Eq}$	=	equivalent lift-to-drag ratio
N_P	=	number of motor poles
PID	=	proportional-integral-derivative control
P_{Input}	=	DC bus input power, W
P_{Req}	=	power required to maintain given flight state
PWM	=	pulse width modulation
q	=	dynamic pressure, lb/ft^2
R	=	resistance, ohms
RPM	=	revolutions per minute
T	=	rotor thrust, lbs
T_X	=	torque about the wind tunnel reference frame X-axis
T_Y	=	torque about the wind tunnel reference frame Y-axis
T_Z	=	torque about the wind tunnel reference frame Z-axis
V	=	velocity
V_∞	=	tunnel freestream velocity, ft/s
V_{High}	=	voltage at current sense resistor input, V
V_{Low}	=	voltage at current sense resistor output, V
VTOL	=	vertical take-off and landing
W	=	vehicle weight, lbs
η	=	efficiency
σ	=	standard deviation

1. INTRODUCTION

The impact of ongoing improvements in electric propulsion technology over the last decade can be seen in the proliferation of small unmanned aircraft of ever increasing capability. The future potential of electric or hybrid-electric powered aircraft is a subject of intense research and development within the aerospace industry. One such focus within this greater research effort is the potential for electric propulsion to increase the feasibility of distributed propulsion concepts that utilize a large number of propulsors to improve maneuverability or aerodynamic efficiency. Effective use of these design concepts may allow for transformational aircraft designs that combine the VTOL capability of rotorcraft with the aerodynamic efficiency of fixed-wing aircraft [1]. Additionally, distributed propulsion designs may yield aerodynamic benefits when paired with conventional lift devices, such as blown wing concepts [2].

While the synergy of electric propulsion and distributed propulsion hints at a new era of technologically and economically feasible aircraft concepts, the development of these vehicles is hindered by a lack of reference data from which to make informed design decisions. Engineers seeking to design an aircraft utilizing these concepts are thus without the analytical and empirical models – and derived rules of thumb - that guide conceptual aircraft development. One critical field in which research is lacking is knowledge of how the aerodynamic interaction of multiple rotors in close proximity can improve or worsen overall performance. An intensively distributed multirotor concept carries a high degree of design risk due to the novelty of the unique aerodynamic effects it exhibits.

Multirotor helicopters are one configuration of VTOL aircraft that use a relatively high number of propulsors to maintain controlled flight. Existing multirotor designs have between 2-18 rotors and are commonly categorized by the number of rotors they use (quadcopter, octocopter, etc.). Designs with three or more rotors nearly universally utilize electrical power transmission. While the vast majority of electric multirotors are small, unmanned vehicles, there are several vehicles in late development designed for manned flight [3][4]. While there is little published data on the hover and flight performance of electric multirotor vehicles, wind tunnel test data reinforces the common impression that current designs exhibit an overall level of performance much lower than what is achievable with a conventional helicopter design [5]. Improving the performance of multirotor designs will require a better understanding of the complex

aerodynamic phenomena they exhibit. Additionally, within the context of advancing VTOL rotorcraft design in general, small multirotors such as quadcopters can serve as a low-cost platform for investigating distributed propulsion concepts that are applicable to more complex designs.

1.1 UAS Multirotor Aerodynamics

The design space for small, multirotor UAS vehicles exists at the conjunction of several complex aerodynamic phenomena. Rotors in close proximity to one another and to fuselage elements generate mutual wake interaction effects. The mutual wake interference effects for dual-rotor tandem and coaxial rotorcraft designs has been thoroughly explored and analytical models for optimizing spacing or determining correction factors are available in varying degrees of fidelity [6][7][8]. However, these models cannot be extended to cover vehicle designs with an arbitrary number and positioning of propulsors. In addition to their mutual interaction, the operational envelope of each "proprotor" encompasses propeller-like axial flow when in a straight climb, but rotor-like edgewise flight at low forward speeds, and also intermediate disc plane inclination angles at high speed forward flight. Disc plane inclination impacts the normal thrust force of the propeller and generates a yawing moment (P-factor) perpendicular the propeller axis [9]. These effects, and their impact on vehicle performance, have not been well characterized for the extreme inclination angles that quadcopters operate at during high-speed forward flight. Small multirotor craft also often utilize propellers of 11" diameter or less, with the blade airfoil sections operating under a corresponding Reynolds Number (Re) range of around 50,000-100,000. Conventionally designed small multirotor propellers have been shown to often yield lower-than-expected performance results which seem to correlate with their low Re [10]. These and other aerodynamic phenomena exhibited by small multirotor vehicles tend to degrade vehicle performance - but may also offer opportunities to boost the performance of knowledgeably designed vehicles.

Small multirotor vehicles require creative solutions to surmount the difficult problems the vehicle type faces. The facilitation of distributed propulsion architectures via electrical power transmission has reignited much interest in understanding whether the aforementioned aerodynamic phenomena can be used to improve vehicle performance. A major contributing factor to the recent reexamination of these complex aerodynamic phenomena is the proliferation of Computational Fluid Dynamic (CFD) simulation software

packages that can often provide numerical estimates of aerodynamic performance relatively cheaply and quickly [11][12]. An example use of CFD to analyze a distributed propulsion design is shown in Figure 1; in this image the effects of ground proximity on rotor wake streamlines is being numerically simulated.

However, a CFD simulation of poorly understood aerodynamic phenomenon without independent validation of the computationally derived results does little to reduce design risk. Wind tunnel data can serve as validation of CFD models and results. There is much ongoing experimental research into small-scale electric VTOL propulsion. The data from this research will provide the validation needed to reduce the risk of distributed propulsion design concepts. Increasingly complex powered wind tunnel test models will be needed to fully explore the aerodynamic effects of these distributed propulsion concepts in depth.

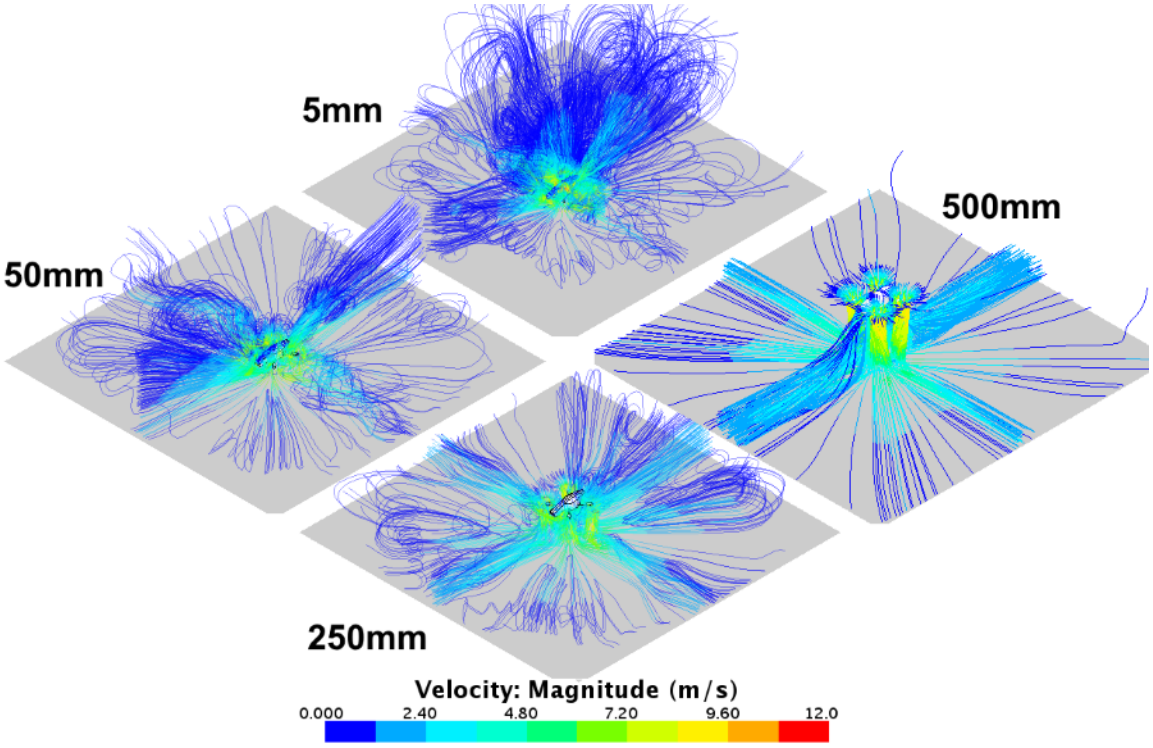

Figure 1. An Example of CFD Methods Applied to Distributed Propulsion Research - Simulated Rotor Wake Streamlines for a Quadcopter in Ground Effect (Author's Own Work).

1.2 Multirotor Wind Tunnel Testing Considerations

The complexity of multirotor aerodynamics, along with their generally small size, encourages the use of full-vehicle or near-full-vehicle tests to determine performance. However, multirotor wind tunnel models

require significantly different test hardware and procedures than traditional aircraft models. Because the rotors and their corresponding wake interactions are a major source of uncertainty, they cannot be readily decoupled from the airframe or from each other, as is common in airplane design wind tunnel tests. The multirotor as a test article is essentially a highly-actuated, powered high-lift device. Providing power to the motors and controlling rotor speed requires a suite of support hardware and software. Additionally, the strong downward wake from the rotors requires special consideration (and where possible mitigation) with regard to wall tunnel interference effects.

Wind tunnel testing of multirotor vehicles requires power and speed management for every single motor. Even small multirotor vehicles can have demanding max power requirements that exceed the limits of many portable bench power supplies; for example, the 3.3 lb 3DR SOLO quadcopter at full power can consume 80W per motor [5]. Additionally, each brushless motor requires either its own 3-phase power supply or an electronic speed controller that requires both DC power and a pulse-width-modulation command signal. The multirotor can be operated wirelessly or modified to allow for power and signal cabling. The former method may require less modification and reduces interference drag from cabling. However, such a test rig would require regular battery replacement and the potential for electromagnetic interference of vehicle command and data telemetry signals would be a concern. The latter method requires modifications to internal hardware, but a DC bench power supply provides a significant advantage in power longevity and stability over a battery. The designer can also use an intermediate method in which some interfaces with the vehicle are wireless while others are wired.

The wind tunnel itself affects the flow of air past the vehicle, resulting in some level of non-equivalence between testing conditions and open-air flight. The level of this non-equivalence, and any correction factors that can be applied, have generally only been well categorized for a small subset of test types and tunnel conditions that assume a lightly loaded model that is of small size relative to the wind tunnel. Powered high-lift devices such as rotors, fan-in-wings, or blown flaps generate a large downward wake that tends to impinge on the tunnel floor, possibly even recirculating within the test section and greatly altering the overall nature of the “wall effects” influencing the test data [13]. Given the relative novelty of vehicles featuring three or more rotors, there is a lack of existing test data with which to develop or evaluate

analytical methods of wind tunnel wall effects. The most pragmatic approach towards mitigating the effect of wake impingement is to limit recirculation through the use of a tunnel with a very large test section relative to the size and thrust capability of the test article. Some other potential methods for reducing wake rollup would be to use a tunnel equipped with a "rolling road" moving floor, or a completely open test section floor. However, a thorough treatment of the wind tunnel effects would still require characterizing the impact of these features themselves.

The flight path of a multirotor is directly coupled to airspeed, pitch angle, and distributed rotor thrust. Thus, steady-level flight at any particular airspeed occurs at a singular vehicle pitch angle and set of rotor speeds. Within a wind tunnel, these factors affect the location of wake impingement on the tunnel floor and therefore influence the severity of wall effects. At low forward speeds, because of the near-horizontal vehicle pitch angle and low tunnel speed, the wake will blow down more vertically. At higher forward speeds, the thrust required for steady-level flight is greater, but the vehicle is inclined forward, which tilts the wake off-vertical. Additionally, the higher tunnel speeds impart more momentum on the rotor wake and thus the location of wake impingement on the tunnel floor will move rearward. Assuming a given wind tunnel test section is not so large as to render the wake recirculation of a given test vehicle insignificant, the vehicle can only be tested within a limited region of its flight envelope, bounded by where the wake floor impingement and rollup results in tunnel flow not approximating free-air conditions [14].

The high degree of actuation that multirotors exhibit greatly increases size of the potential test space. Along with the staple wind tunnel input metrics of dynamic pressure and test rig orientation, the multirotor experiment designer must also contend with a vast combination of rotor speed settings - and if the vehicle is capable of reconfiguration - different operational flight modes. Efficient wind tunnel testing of advanced VTOL designs, such as models of the GL-10 Greased Lightning, compress the vast test space into as few test points as possible through the use computational Design of Experiment tools. Additionally, the test rig and mounting hardware are highly actuated and the test procedure is highly automated, which allows the performance data to be quickly gathered as the vehicle automatically sweeps through different flight states and configurations [15]. This level of command over test procedure requires a tunnel with very centralized and integrated test control hardware. These automation and actuation capabilities may not be commonly

found at smaller wind tunnel test facilities. In such a case, the experimenter must carefully choose the type and fidelity of test parameters necessary to complete their experiment, lest the number of required test cases become infeasible.

2. LITERATURE REVIEW

2.1 Notable Multirotor Wind Tunnel Tests

2.1.1 Addressing High-Lift Device Wake Impingement in Wind Tunnel Tests

NACA/NASA multirotor wind tunnel research throughout the 1950's and 1960's focused heavily on evaluating the accuracy of rotor inflow and lifting device wake theories for different designs and arrangements of rotors. Much of the work from this timeframe was performed at Langley Research Center under the direction of Harry H. Heyson, who published an authoritative volume of work detailing the challenges involved in analytical and wind tunnel modeling of multirotorcraft and other high-lift device aerodynamics. A major early finding of these research efforts was that high-lift devices such as rotors violated the small force coefficient assumption relied upon by methods for estimating the wind tunnel wall interference for more conventional lift devices, such as airfoils. The wake of a high-lift device such as a rotor cannot be assumed to pass directly downstream, as the lifting force significantly skews the resultant wake off-centerline, in the direction opposite of the lifting force. The rotor wake impinges on the tunnel floor, and then flows outward towards and up along the walls, creating a recirculation vortex behind the model. In extreme cases, the recirculation can envelop the model itself, in which case the tunnel flow does not adequately approximate free-air conditions [13]. An illustration of this flow circulation is shown in Figure 2.

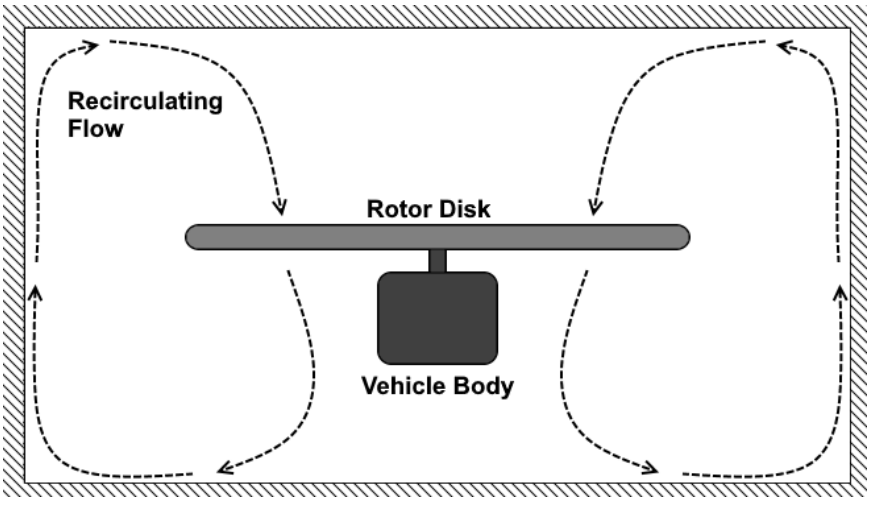

Figure 2. Sketch of Looking Down Wind Tunnel at Rotor Wake Recirculating Within the Test Section (Based on an Illustration by Heyson) [13].

Experiments by William Rae at the University of Washington investigated the recirculation phenomenon using a large, single-rotor setup in an attempt to determine the point at which flow through the test section breaks down and wake recirculation envelops the model. Through the use of tuft boards, static pressure taps embedded in the tunnel wall, and force balance measurements, Rae developed a method for estimating the limit of rotor downwash angle beyond which flow breakdown would occur - dependent on tunnel speed, tunnel geometry, and model size (occasionally referred to as Rae's Limit). The experiments demonstrated several important trends affecting the downwash limit - rectangular tunnel cross-sections with width-to-height ratios of 1.5 and 0.67 allowed for more downwash than a square tunnel, while adding fillets to the corners of the wind tunnel decreased the amount of allowable downwash [14]. Together, Rae and Heyson's research demonstrated that powered lift experiments could be performed successfully even in tunnels with comparatively cross-sectional test area, provided the scope of the tests included only conditions under which the rotor wake would impinge the tunnel floor well aft of the rotor.

2.1.2 Modern Multirotor Wind Tunnel Testing

Subscale and full-scale wind tunnel testing have played a critical role throughout the last 60 years in the development of transformational VTOL concepts such as the NASA XV-15 and its predecessor prototypes[16]. Wind tunnel tests continue to be a critical tool in evaluating the complex aerodynamic, aeroelastic, and structural loading characteristics of these vehicles [17]. More recently, the rapid proliferation in electric distributed propulsion experimental designs over the last decade has seen a corresponding rise in wind tunnel evaluation of these concepts. Subscale testing of a GL-10 Greased Lightning model in the NASA Langley 12-Foot Low Speed Tunnel is one such example of wind tunnel tests being used to validate model predictions for these aerodynamically complex concepts [15].

Some recent wind tunnel experiments seek to better evaluate the current performance level of commercially available, hobbyist-level electric multirotor vehicles - which are often designed without great consideration given to rotor-rotor and rotor-airframe aerodynamic interactions. A 2016 project at NASA Ames sought to provide a set of reference data for this class of small electric multirotors by performing a series of powered tests with 5 COTS multicopters in the U.S. Army 7-by 10-ft Wind Tunnel. The vehicles, which included a DJI Phantom 3, varied 9.8 to 31.4 inches in rotor-to-rotor length and 2.8 to 12.8 lbs in nominal flight

weight. The vehicles were internally retrofitted to allow for man-in-the-loop control over motor RPM and mounted to a sting stand with integral load cell. Aerodynamic forces and electrical power was measured for a parameter set of different motor speeds, tunnel speeds, and pitch angles for each vehicle. Data from powered and unpowered tests was used to develop a set of lift, drag, and pitching moment vs. pitch angle plots for each vehicle. Static stand tests were performed to develop hover performance data. Additionally, the forward flight and hover figure of merit for an isolated rotor from each vehicle was evaluated [5]. The resulting performance data likely represents the most in-depth and professionally gathered published data for hobbyist-level multirotor vehicles.

The large size and well-characterized nature of the tunnel used in the Ames tests indicates that the force data acquired during these tests likely provides the most flight-like performance data available. The DJI Phantom 3 force data from these tests provides a comparative dataset with which to evaluate the force data obtained from similar tests performed in the Cal Poly Low Speed Wind Tunnel. This comparison will provide understanding on the feasibility of performing powered multirotor testing in smaller wind tunnels.

2.2 An Equivalent Lift-to-Drag Ratio Metric for Electric Multirotors

The lift-to-drag ratio (*L/D*) is a fundamental metric of an aircraft's aerodynamic efficiency. The lift-to-drag ratio of a typical heavy utility helicopter such as the UH-60 is 3 to 5 at cruise speed; a typical fixed wing aircraft of similar weight could achieve a lift-to-drag ratio of more than 4 times greater [18]. The aerodynamic efficiency of small multirotor vehicles such as commercial quadcopters has long been understood to be quite poor. There is a lack of published data on metrics equivalent or similar to the lift-to-drag ratio for this class of vehicle. Determining the lift-to-drag ratio of a rotorcraft is less straightforward than it is for a conventional airplane because the rotor couples the lift and thrust forces. However, if the entire rotorcraft is conceptualized as a single point, then the forces on the vehicle can be analyzed solely in terms of lift, weight, thrust, and drag forces. The thrust in this case would be the forward flight force component of the overall rotor thrust.

In many cases it may be more advantageous to determine an aerodynamic efficiency metric from the power at some point within the propulsion system. For instance, system power is much more readily measurable than propulsor thrust for many test setups. Secondly, such an approach may be more useful in the

conceptual design of small, distributed propulsion electric vehicles - where propulsor and powertrain losses across the flight envelope are not well characterized. In such a situation, a designer would have difficulty mapping the thrust-derived aerodynamic efficiency metric to system level efficiency. An aerodynamic efficiency metric derived from propulsion system power - for example, required battery power - provides the designer of an electric UAS a more immediate sense of the system efficiency of a particular type of system. Because propulsive system losses are incorporated into this metric, an attempt to generalize this metric to a class of vehicles would have to account for the quality of the propulsion system components (i.e. cheap, relatively low-efficiency motors vs. expensive, high-efficiency motors).

This project uses the metric "equivalent lift-to-drag ratio" ($L/D|_{Eq}$), which is a function of the vehicle weight, airspeed, and DC bus power. For a free-flying test vehicle the counterpart to the bus power would be the battery terminal power. Under the condition of steady, level flight (zero specific excess power), the power required to maintain the flight state is:

$$\boldsymbol{P_{Req} = DV} \tag{2.1}$$

Where P_{Req} is the vehicle output power required, D is the total drag force acting on the vehicle, and V is the vehicle's airspeed. Dividing both sides of the equation by the vehicle weight gives:

$$\boldsymbol{\frac{P_{Req}}{W} = \frac{D}{W}V} \tag{2.2}$$

Where W is the vehicle weight. Under the aforementioned steady, level conditions, lift produced is equal to the weight of the vehicle which can be used to alter the equation such that:

$$\boldsymbol{\frac{P_{Req}}{W} = \frac{D}{L}V} \tag{2.3}$$

Where L is the lift force. Inverting either side of the equation and multiplying by airspeed yields:

$$\boldsymbol{\frac{WV}{P_{Req}} = \frac{L}{D}} \tag{2.4}$$

Which indicates that the lift-to-drag ratio for a rotorcraft conceptualized as a point origin can be determined from the vehicle's weight, airspeed, and the output power. Because P_{Req} is simply the product of thrust and airspeed this is still a statement of the conventional lift-to-drag ratio. Given a well-characterized propulsor

inclined perpendicular to the flow, P_{Req} could be related to the power at the propulsor shaft, P_{prop} with a propeller efficiency map. However, no efficiency maps are available for a set of mutually interfering rotors operating across a broad range of rotor plane inclinations.

Power at the DC bus, P_{Input} is related to required output power by the vehicle's net input-to-output system level efficiency:

$$\boldsymbol{P_{Req} = P_{Input}\eta_{System}} \quad 2.5$$

Where η_{System} is the total efficiency of the vehicle. The total system efficiency is the product of all the power losses between the input power and power output into the atmosphere:

$$\boldsymbol{\eta_{System} = \eta_{Cabling} * \eta_{Controllers} * \eta_{Motors} * \eta_{Propulsors} \cdots * \eta_n} \quad 2.6$$

Where η_{System}, $\eta_{Controllers}$, η_{Motors}, and $\eta_{Propellers}$ are the power loss in the power cables, motor controllers, motors, and propulsors, respectively. η_n represents potential other power loss terms a designer may deem significant, such as the impact of subsystem power draw. This system efficiency term is used to establish the lift-to-drag equivalent metric:

$$\frac{\boldsymbol{WV}}{\boldsymbol{P_{Input}}} = \frac{\boldsymbol{L}}{\boldsymbol{D}}\boldsymbol{\eta_{System}} = \frac{\boldsymbol{L}}{\boldsymbol{D}}\Big|_{\boldsymbol{Eq}} \quad 2.7$$

This equation is only valid under the following conditions and assumptions:

- The side force, yaw moment, and roll moment are negligible.
- The measured lift force (F_Z) is equivalent to the assumed vehicle weight.
- The net drag force (F_X) is zero.
- The pitching moment (T_Y) is zero.

3. TEST SETUP

3.1 Test Hardware

The required test hardware includes the wind tunnel and its actuation and instrumentation suite, as well as the custom, powered quadcopter test rig. Additionally, a large amount of additional support equipment is needed to interface the tunnel hardware, the test rig, and the computer command and data logging interface.

3.1.1 Wind Tunnel

The Cal Poly Low Speed Wind Tunnel has provided Cal Poly students and faculty with an on-site wind tunnel facility for more than 30 years. It has been continually retrofitted and refurbished to support countless student and industry projects. The tunnel features a 4 ft. wide x 3 ft. high x 14 ft. long test section with a top airspeed of 130 MPH. Its instrumentation and test hardware includes electrically actuated position control, 6-DOF force-torque measurement capability, a 64-channel pressure transducer, a particle image velocimetry (PIV) laser scanning system, and a moving belt floor with a top speed of 100 MPH [19].

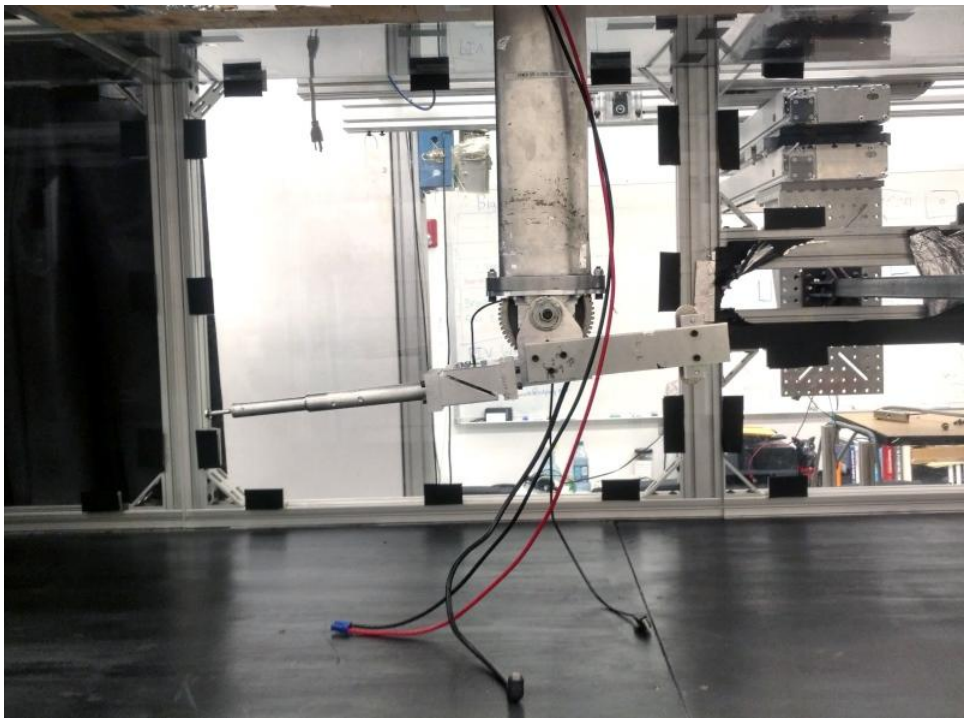

Figure 3. Wind Tunnel Test Section with View of Variable Pitch Sting Mount and Boom.

The test data frame of reference is shown in Figure 4. All force and moment data is provided in the wind axes reference frame - positive F_Z points upwards, positive F_X points downstream, and positive F_Y points

out the starboard side of the test vehicle. Correspondingly, lift is a positive F_Z force, drag is a positive F_X force, and a positive T_Y moment indicates an upwards pitching moment.

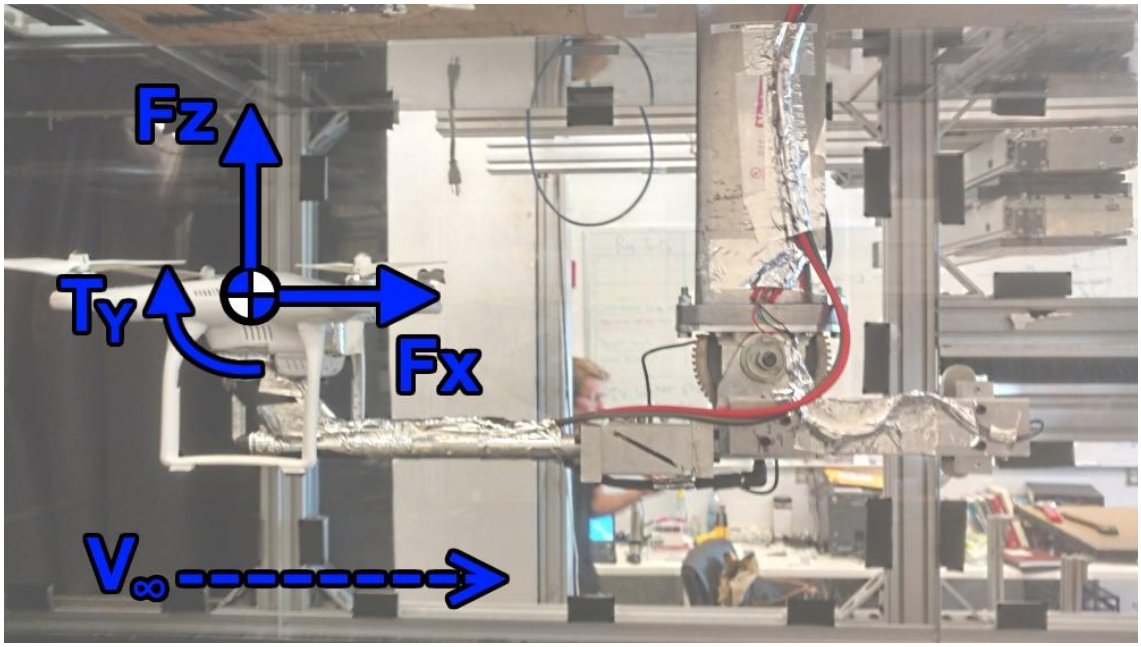

Figure 4. Principal Longitudinal Plane Forces acting on Test Rig Vehicle.

3.1.2 Test Vehicle

The test rig is based upon a DJI Phantom 3 quadcopter with the Vision Positioning System (VPS) module and landing gear mounted. The DJI Phantom 3 is a 2.82 lb "X-configuration" quadcopter widely used to capture HD aerial photography. The camera and camera mount were removed to maintain the same outer mold line as previous wind tunnel tests at NASA Ames featuring this vehicle. Most of the external hardware is identical to a stock DJI Phantom 3; however, internally the test rig is fabricated from entirely custom hardware. Several critical aircraft specifications are listed Table 1 [20].

Table 1. DJI Phantom 3 Quadcopter Performance and Dimensional Specifications [20].

	Value	Units
Gross Weight	2.82	lbs
Max Speed	31.1	kts
Service Ceiling	20000	ft
Flight Endurance	23	minutes
Airframe		
Weight	2.31	lbs
Width	11.5	in
Length	11.5	in
Height	7.6	in
Props (Each)		
Weight	0.03	lbs
Diameter	9.5	in
Camera and Mount		
Weight	0.4	lbs

The center of gravity (CG) of the DJI Phantom 3 was determined using a stock vehicle. The CG was measured to be equidistant from all four rotor axles in X-Y plane and approximately 0.55 inches below the seam line between the upper and lower plastic casings that make up the fuselage. The modified test rig used the stock vehicle CG location to set the origin for torque measurements.

External Vehicle

The test rig's outer fuselage shell, landing gear, propellers, motors, VPS module, and various fasteners were all constructed from standard DJI OEM parts. The OEM battery module was not used due to the need to reserve internal volume for the command handling hardware and sensors. A 3D printed plastic cap approximates the external housing of the battery that protrudes from the rear of the vehicle. A view of the external features of the vehicle can be seen in Figure 5. Additional pictures of the test vehicle can be found in the appendix.

Figure 5. Exterior of the Test Rig Vehicle.

A critical aspect of these tests was the ability to swap the position of motor pairs that share the same direction of rotation. Thus, it was critical to be able to quickly reference the position of each motor when in their default and swapped positions, referred to as Configuration A and Configuration B, respectively. Figure 6 shows the numbering of each ESC-motor-rotor set in each position.

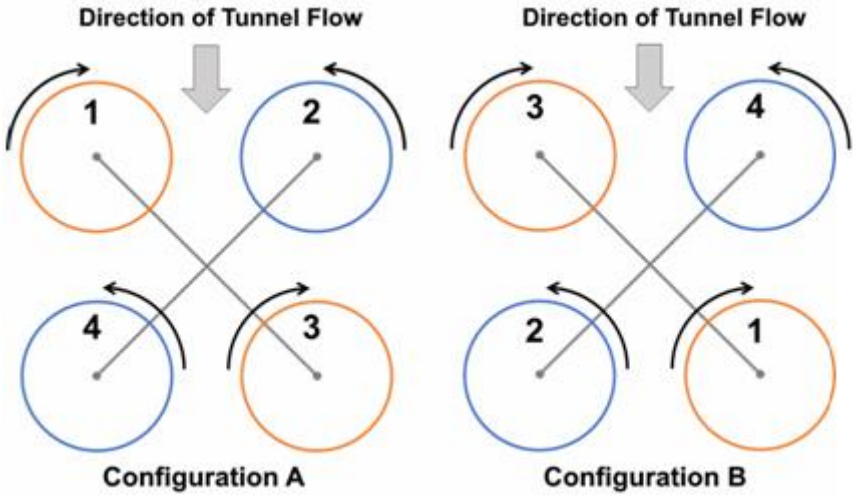

Figure 6. Position of Numbered Motor-Rotor Pairs in Default and Swapped Vehicle Configurations.

Internal Hardware

The original internal hardware of the DJI Phantom 3 was not installed into the test rig due to the difficulty of interfacing the necessary test control hardware and instrumentation with the OEM integrated controller boards. An aluminum plate bolted to the floor of the battery tray provides the mounting surface for the custom internal hardware setup. A 2-pole terminal block splits the main DC power cables to each of the four motor controllers. Motor control is managed with a set of Castle Creation Talon 25 ESC boards and a servo controller board with USB interface. A Pololu Micro Maestro servo controller board generates the pulse-width signals that the ESCs reference to set the motor speed. The specific ESC model used was selected to maintain similarity with the Phantom 3 wind tunnel reference data previously collected at NASA Ames [5]. A red LED mounted in one of the motor arms serves as an arming light to warn personnel when the motors are receiving power. An annotated image of the internal test vehicle hardware can be seen in Figure 7. A wiring diagram of the internal test rig hardware can be seen in Figure 8.

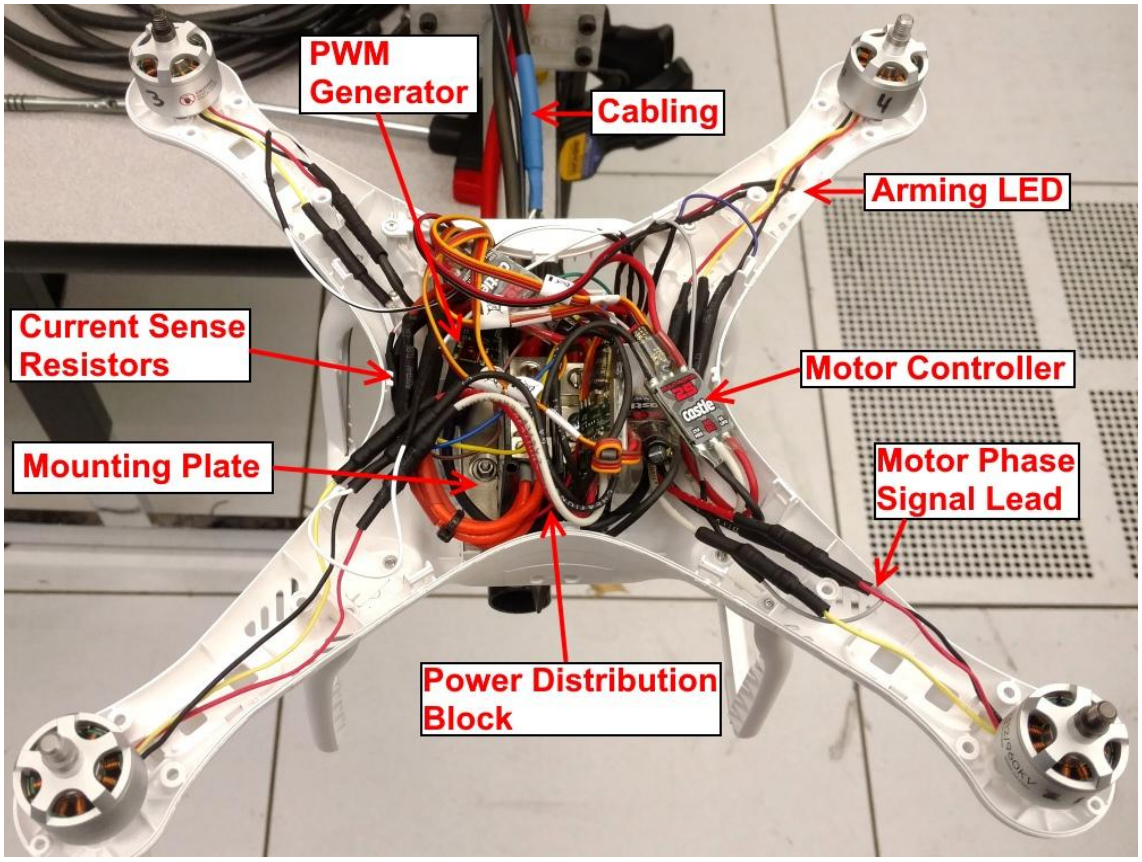

Figure 7. Internal Hardware Setup of Test Rig Vehicle.

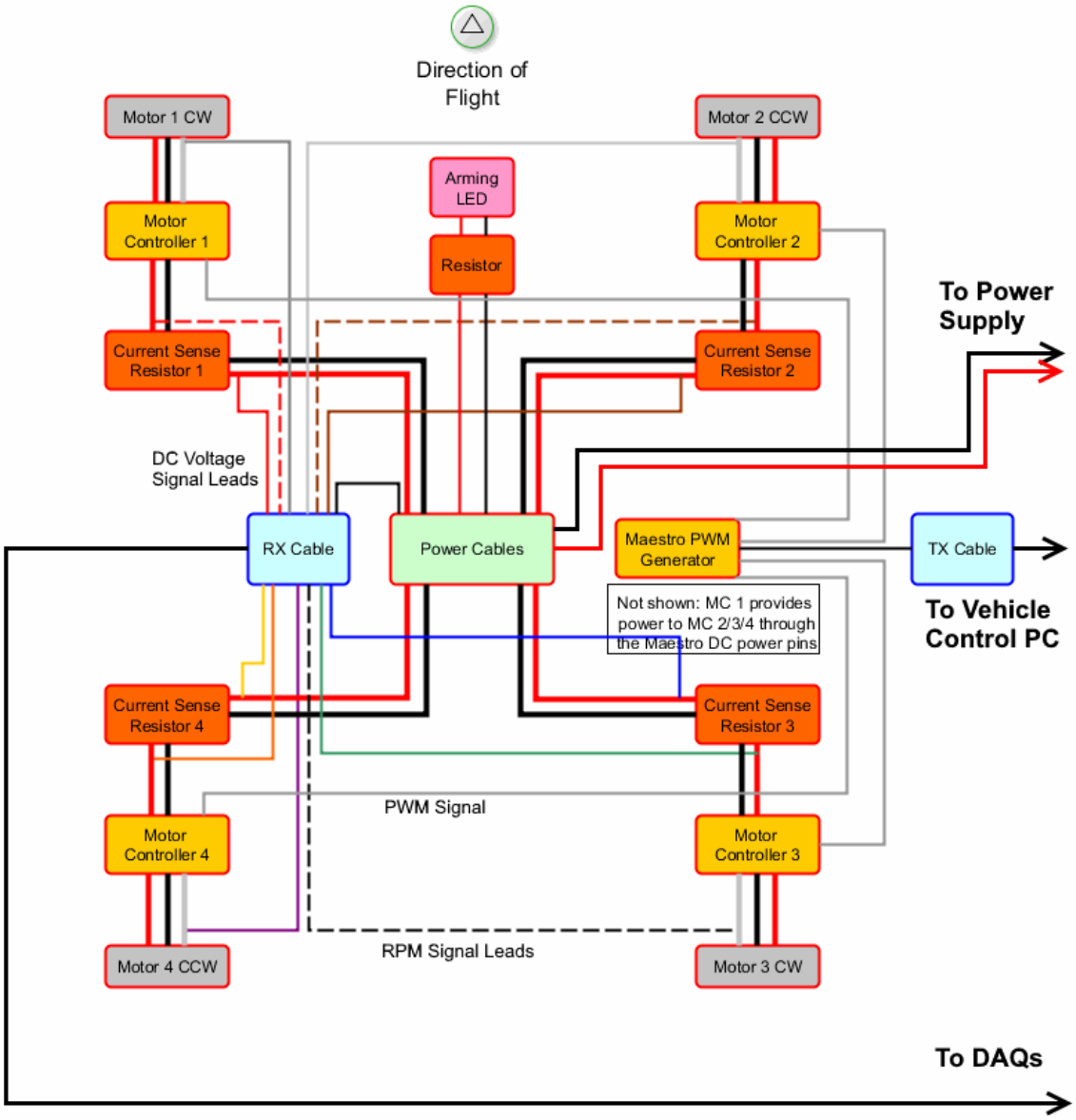

Figure 8. Test Rig Internal Hardware Wiring Diagram.

3.1.3 Hardware Interface

Power Interface

DC power is supplied to the test vehicle via 8-gauge wire; a high gauge cable was selected to minimize power loss in the cabling between the power supply and the test rig. The last 3 feet of the cable is extremely high flex to avoid wire strain from impacting the load cell readings. Power is distributed internally to the controller boards via a Schneider Electric 9080LB series power distribution block. DC power is supplied via an HP 6012B bench power supply providing a nominal 14.8V and up to 50A of current.

Command and Data Interface

Motor commands to the test rig are handled via a USB interface that connects to the servo controller board. Test rig sensor data is transferred via a 13 position, 26 AWG shielded cable assembly to the data acquisition board mounted on top of the tunnel. Both the data and the command cable assemblies have a disconnect assembly near the test rig that allows for easier installation and removal. Similarly, the force torque transducer's signal line is routed to the DAQ board.

The DAQ board itself is a plywood mounting surface for the two data acquisition modules and their support hardware. The Measurement Computing USB-1608HS is a 16-bit simultaneous DAQ configured for reading the differential output signals of the force transducer sensor. The National Instruments NI-USB-6210 is a 16-bit sequential DAQ configured to read the single-ended voltage outputs from the test rig sensors. Because the test rig is powered at 14.8V, the sensor lead voltage needs to be stepped down to the ±10V operating range of the NI DAQ. This step down is managed by a set of voltage divider / RC low-pass filter circuits that reduce the max nominal voltage to 7.4V and filter out signals with a frequency above the sample rate limit, which is discussed further in Section 3.3. A picture of the data acquisition board is shown in Figure 9.

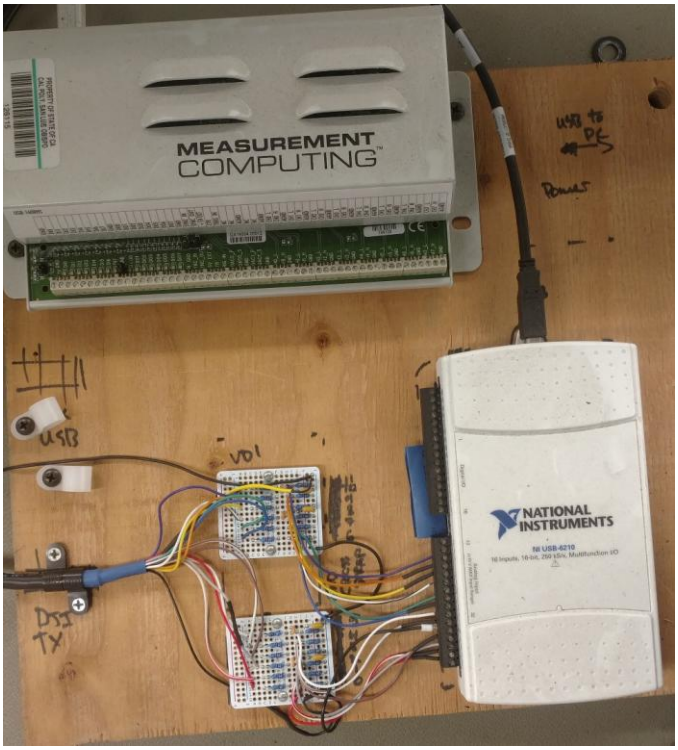

Figure 9. Data Acquisition Board.

Because determination of motor current draw relies on measurements compared across two DAQ channels, measurement uncertainty introduced by the 0.1% tolerances of the 10 kΩ resistors used in the voltage divider boards was a concern. To minimize this, the actual resistance of each resistor was measured to five significant figures using an Agilent U3402A digital multimeter, which allowed the resistance to be determined down to 100 milliohms. These resistance readings were referenced by the LabVIEW signal processing methods to calculate the original voltage.

Mounting Setup

The test rig is mounted via a bent sting blade bolted to the bottom of the vehicle. The steel blade is covered in a 3D printed symmetrical airfoil which provides a fairing for the cable runs into the test rig. A 3D printed conical nose cone insert covers the sting fastener point. The sting blade is bolted to the model support mechanism which consists of an armature that incorporates the force torque load cell. The armature is connected to an airfoil-shaped strut through a worm screw assembly which provides powered pitch control via a stepper motor. The entire strut moves up and down via a linear actuator above the tunnel to provide control over the vertical positioning of the test rig. An annotated view of the vehicle mounting setup can be seen in Figure 10.

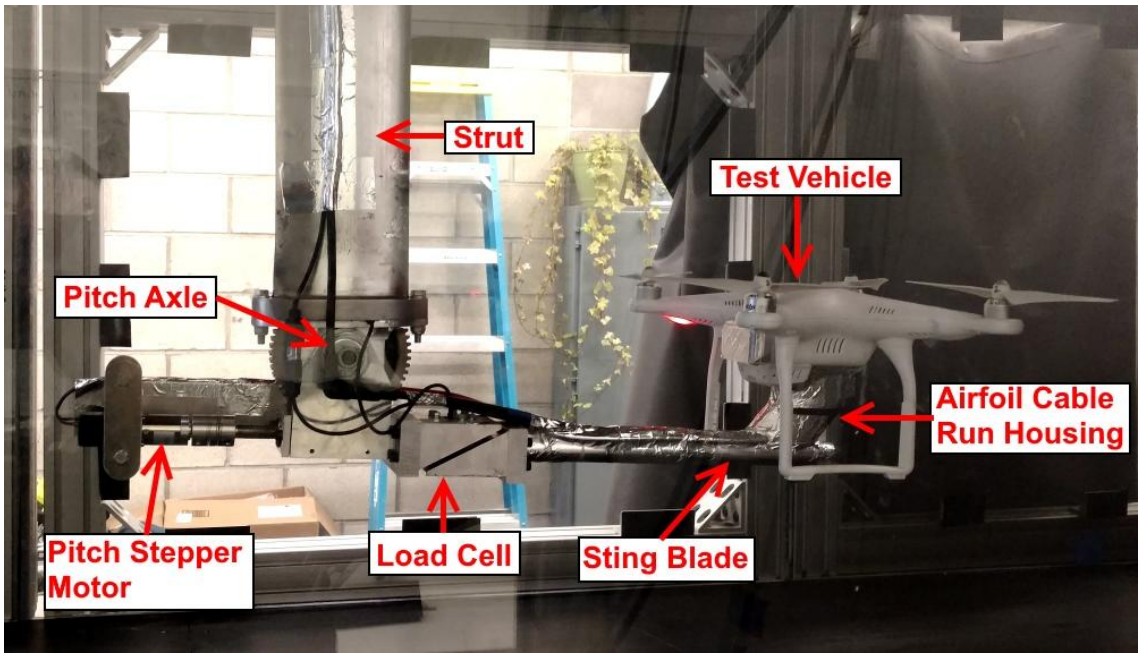

Figure 10. Test Vehicle Mounting Setup.

3.1.4 Instrumentation

Electrical Power

Electrical power to the ESC-motor-rotor sets is measured via a current sense resistor (CSR) placed in-line with each ESC positive DC lead. Current sense resistors have a high tolerance and low resistance, and in accordance with Ohm's law the voltage drop across their leads is proportional to the current passing through the resistor. The resistors installed in the test rig have a nominal resistance of 0.01 Ω and a tolerance of ±1%. DAQ sensor leads attached to either end of each current sense resistor allow the current flowing to each motor to be calculated from the sensor lead voltage using the equation provided in Equation 3.1:

$$\boldsymbol{I = \frac{\left(V_{High} - V_{Low}\right)}{R}} \tag{3.1}$$

Where I is the current flowing through the current sense resistor, V_{High} is the DC voltage between the power distribution block and the current sense resistor, V_{Low} is the voltage between the current sense resistor and the ESC, and R is the nominal resistance of the current sense resistor. As shown in Equation 3.2, these two voltage measurements also allow the power usage of each ESC-motor pair to be calculated:

$$\boldsymbol{P = IV_{Low}} \tag{3.2}$$

Where P is the power going into each ESC and I is the current.

Motor Speed

Motor speed was tracked by monitoring the back electromotive force (BEMF) on a single power lead of each motor. The test rig's 2312 motors are typical 3-phase brushless DC motors with 14 magnet poles (7 pole pairs) and 12 stator poles. The number of signal cycles a phase completes in one mechanical rotation is equivalent to the number of magnet pole pairs on the rotor. In other words, the frequency of motor rotation can be determined by dividing the phase commutation frequency by the number of pole pairs (or by half the number of magnet poles). BEMF frequency is equivalent to the commutation frequency [21]. Accounting for conversion factors, the motor speed can be calculated from the BEMF frequency via:

$$RPM = \frac{120 * f_{BEMF}}{N_p} \quad (3.3)$$

Where f_{BEMF} is the back EMF frequency of the motor lead and N_p is the number of poles of the motor. The trapezoidal shape of the back EMF makes it easy to reconstruct from a set of voltage samples. The BEMF voltage on a single phase of each motor was tracked by DAQ sensor leads. Within LabVIEW, a fast Fourier transform (FFT) method was used to reconstruct the BEMF frequency from a streaming set of voltage samples. As the back EMF signal was quite noisy, the motor lead signal was run through a LabVIEW software bandpass filter with 350 Hz and 850 Hz roll-off frequencies, which corresponds via Equation 3.3 to a detectable motor speed range of about 3000-7286 RPM. The accuracy of this speed measurement method was verified through tests using an AGPtek handheld laser tachometer measuring rotor revolutions per second. The test was performed by using the LabVIEW motor command methods described in Section 3.2.4 to set a desired motor RPM, then taking a 10 second average of data gathered with both the LabVIEW FFT method and the laser tachometer. A comparison of these results is provided in Table 2. Note that the tachometer counts are twice the measured RPM due to each of the two propeller blades being counted by the optical tachometer. The method is shown to provide less than 1% error in both measured RPM and matching commanded RPM.

Table 2. A Comparison of RPM data collected via LabVIEW and Handheld Tachometer.

LabVIEW		Tachometer		
Commanded RPM	Measured RPM	Counts	RPM	LabVIEW % Error
4000	3997	8047	4024	0.652
5000	4998	10005	5003	0.099
6000	5984	11984	5992	0.130
7000	6996	13979	6990	0.088

Force and Torque

Force and torque measurements are provided by a six degree-of-freedom ATI Mini58 Force/Torque Sensor System. The system hardware consists of the load cell module shown in Figure 11, an interface/power supply box (IFPS), and interconnecting cable assemblies. The load cell operates through a series of internal

strain gauge circuits that change their resistance as load is applied or removed. The corresponding change in voltage through each circuit is monitored by the MC DAQ, which reads the differential voltage between each signal wire pair. A LabVIEW program is used to apply a calibration and transformation matrix to the signals to find the tunnel reference frame forces and torques. The sensing ranges and resolutions along all three sensor frame axes are provided in Table 3.

Figure 11. ATI Mini58 Load Cell.

Table 3. Mini58 Sensing Range and Resolution.

Measurement	Range	Resolution
F_X, F_Y (lbs)	157	0.037
F_Z (lbs)	382	0.066
T_X, T_Y (in-lbs)	265	0.05
T_Z (in-lbs)	265	0.03

Wake Visualization Tools

A 4 x 4-ft long tuft board was built to facilitate visualization of the wake impingement location on the tunnel floor. The tuft board was constructed out of two 2-foot long plywood sheets with a white gloss surface finish. The tufts consisted of 3” long red wool string taped to the board at 3” intervals.

Visualization of wake rollup along the walls was accomplished with a smoke streamline generated by a commercial smoke machine vented into the front of the tunnel through a flexible hose. A green line laser pointer was also used to illuminate cross-sections of smoke flow.

3.1.5 Computer Hardware

A computer with LabVIEW installed is required to operate the control and data gathering methods. Test runs performed for this project were run on two separate computers, with one computer managing the wind tunnel sting position and the other computer running the load cell, Scanivalve pressure sensor, and test rig controller LabVIEW simulations. Running three simulations at once can be computationally intensive – this setup was managed on a laptop with an i5-2520M processor at 2.5 GHz, but required setting the LabVIEW process to a high priority to avoid occasional software race conditions.

3.2 Test Software

The primary software used for testing consisted of a suite of LabVIEW projects that provided a UI for handling test vehicle control, wind tunnel, control, and sensor data acquisition. LabVIEW is a graphical programming environment that provides a relatively easy platform for generating a user interface for test instrument control and data acquisition.

3.2.1 Wind Tunnel Aerodynamic Control

The Wind Tunnel LabVIEW program was primarily responsible for tracking tunnel speed and dynamic pressure. The program was developed by Cal Poly students working in the Low Speed Wind Tunnel facility. The program acted as a command and control center for the wind tunnel instrumentation; primarily the Scanivalve pressure transducer and the ATI force transducer, although for this project transducer data was collected by a separate LabVIEW program. The functional purpose of the Wind Tunnel Aerodynamic Control program in this project was to track tunnel speed to allow for man-in-the-loop adjustments to tunnel fan RPM. It was run on the tunnel control computer. A screenshot of the relevant parts of the wind tunnel control program while under operation can be seen in Figure 12.

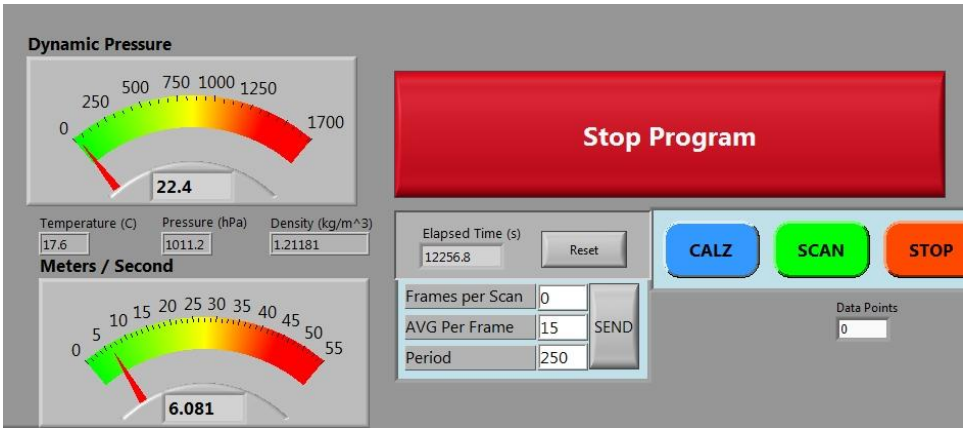

Figure 12. Screenshot of Wind Tunnel Speed Controller User Interface.

3.2.2 Wind Tunnel Actuation

The Wind Tunnel Actuation Program interfaced with the test sting's linear drive and stepper pitch motor, allowing the test rig a single axis of translation (Z-axis) and a single axis of rotation (vehicle pitch angle). The program allowed the user to manually adjust z-height and pitch independently, or set a desired pitch angle and have the mounting boom automatically raised or lowered to maintain the same relative height within the tunnel.

3.2.3 Force Transducer Data Recording Program

A LabVIEW program developed by ATI served as the basis for the program responsible for processing and logging force transducer data. It was slightly modified to pass the force and torque measurements to a global variable that could be read by the master control program. The program was run on the Test Vehicle Control computer. An image of the transducer data recorder front panel in its idle, uncalibrated state is shown in Figure 13. The left side of the front panel provided controls for interfacing with the load cell DAQ and data and calibration files. For test runs data was sampled at 10000 Hz, with samples read in and averaged in blocks of 1000 points. The center of the panel provided a matrix of raw voltages, a subset of the last read-in data set, and of the average values from the last data set. The bias and unbias radio buttons allowed the user to tare the current sensor readings – taring before each test run became critical as the sensor unfortunately experienced a great deal of drift, which is described further in Section 4. A final critical aspect of the force transducer controller is the transform matrix located at the center bottom of the front panel. The transform matrix allowed the user to translate the origin of the force and moment readings

to a point away from the sensor's physical origin. For the tests runs, the origin was translated to the point in the test vehicle corresponding to an unmodified DJI 3 Phantom's center of gravity. Because the transducer was mounted on the same arm as the test vehicle, the distance of the transform doesn't change as the sting pitch was changed. However, since the test procedure called for the principal force axes to always be aligned with the wind axes of the tunnel, the y-axis rotation input had to be adjusted whenever the pitch angle of the sting was changed.

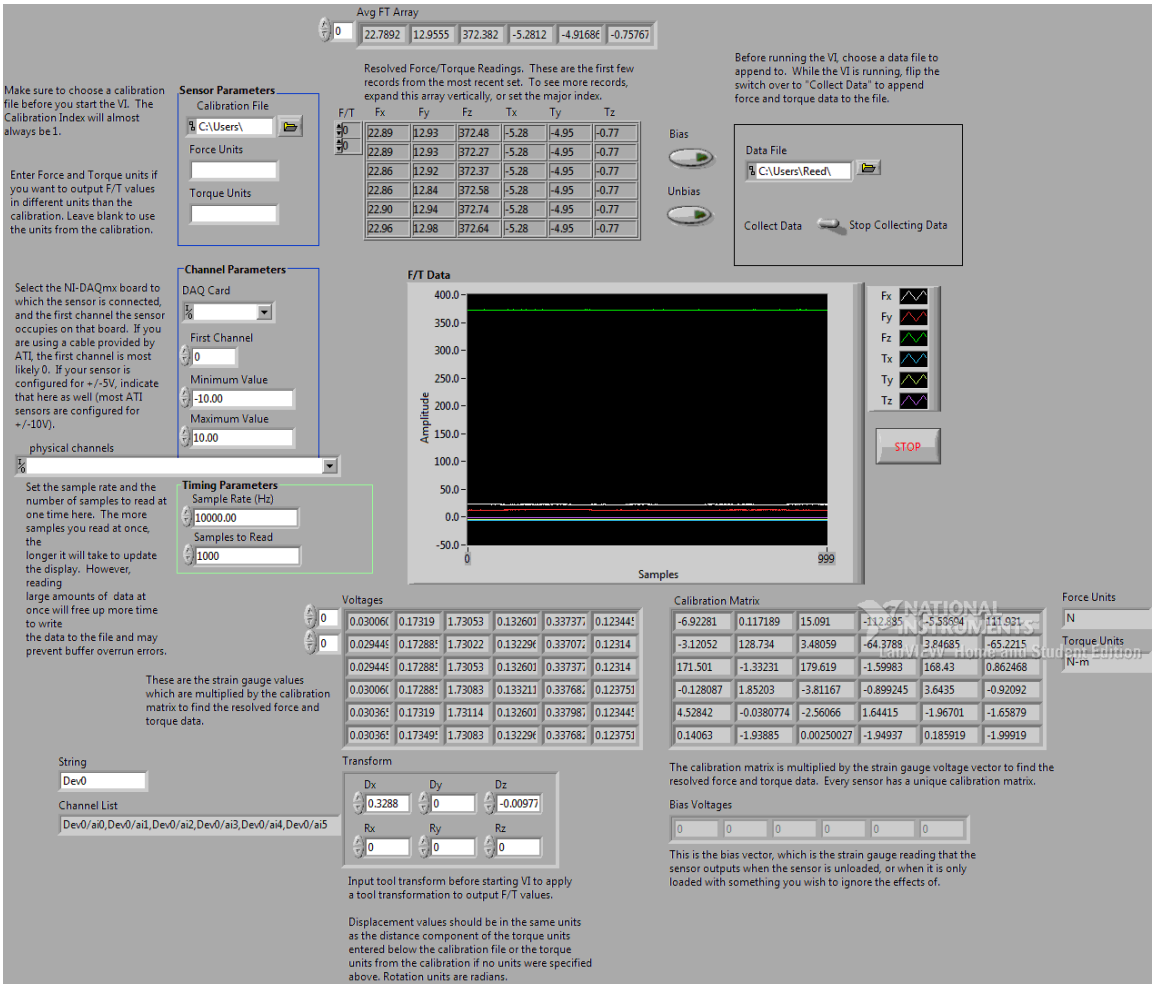

Figure 13. ATI Force Transducer LabVIEW Control Front Panel.

3.2.4 Test Vehicle Master Control and Data Recording Program

The Test Vehicle Master Control and Data Recording Program (referred to as QuadMotorCommand in the LabVIEW project) was the script responsible for communicating with the test vehicle, tracking test vehicle state, and processing and logging test vehicle data. Command packages were sent via USB interface to the

onboard Micro Maestro board controlling ESC PWM signal. Data was received over the USB interface from the Test Vehicle Data DAQ. Figure 14 shows an annotated view of the master control program front panel during operation. Features of the individual panels are described in further detail below.

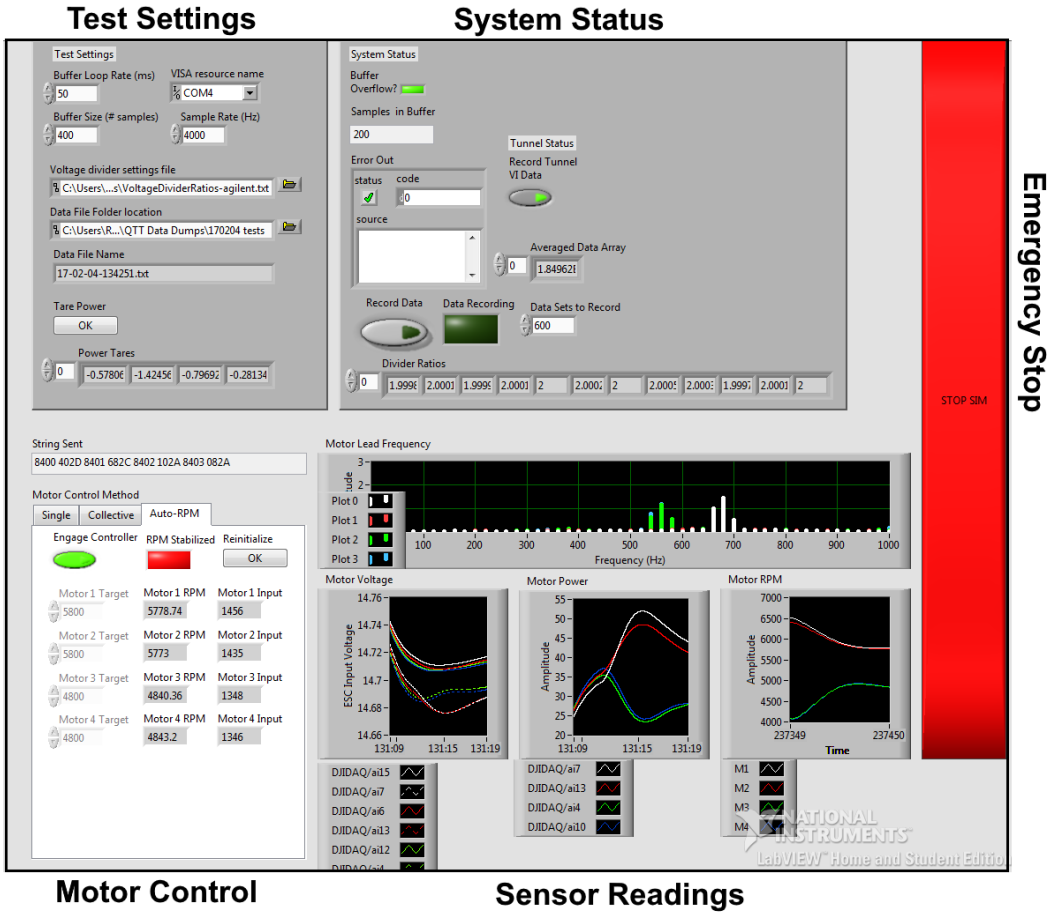

Figure 14. Screenshot of Master Control Program during Operation.

Test Settings Panel

The test settings panel allowed the user to specify DAQ sample rate and program settings such as data buffer size, the rate at which the buffer is cleared, and the USB communications port that connects to the NI DAQ. Additionally, the user could select the location of the file containing the voltage divider board resistance data measurements and the directory to save test run data to. Data files were automatically created with a date and timestamp filename whenever the Record Data button was pressed. The Tare Power button allowed the user to tare the current voltage readings as zero for each channel – typically this was done to remove a millivolt range bias as the test rig electronics warmed up after being powered on.

System Status Panel

Current system status was provided on the System Status panel. The current number of samples in the data buffer was provided along with a status light of whether the data buffer overflowed, indicating a program fault and the loss of test data. The Error Out subpanel served as a debugger by providing a trace of program fatal errors encountered. The large Record Data toggle switch began a 30 second data gathering test run – while data was being gathered the Data Gathering light is illuminated. A smaller toggle switch directed the program whether to collect force/torque and tunnel flow data from the global workspace and log it in the data file. The remaining space in this panel was utilized for various system state displays useful for debugging program performance.

Motor Control Panel

The Motor Control Panel provided several modes for controlling the speed of the test vehicle's motors. The Single and Collective tabs provided both a slider and text field for controlling the motor RPM singly or together, respectively. The final method shown in detail in Figure 15 automatically ramped the motors up to a set of user specified speeds and maintained that RPM via PID loop until disengaged. This was the primary control method used for the test runs as it provided highly stable motor speed. The RPM Stabilized indicator turns green once the motors are up to speed. The Reinitialize button reset the control in the event that the program loses tracking of the motor speed. The right-most data fields displayed the current pulse width in microseconds being generated by the Maestro servo controller for each channel.

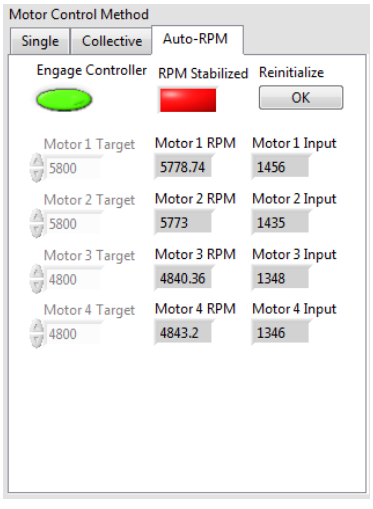

Figure 15. Detail of Automatic Motor RPM Control Feature.

Sensor Readings Panel

The sensor readings panel, shown in detail in Figure 16, provided time-lapse displays of the filtered motor sensor data. The bar chart at the top of the panel provided the real-time power spectrum of the signals on the motor lead sensors generated by the fast Fourier transform method. Each peak corresponds to the BEMF frequency of a motor; while this value was converted to motor RPM before being logged, the real-time spectrum plot served as a useful tool for monitoring whether motor RPM was stable or if the model was behaving erratically. The three scrolling waveform charts at the bottom of the panel provided the last 10 seconds worth of filtered data for the voltage and motor RPM measurements as well as the corresponding calculated motor power. In the voltage chart, V_{High} is a solid line while V_{Low} is dashed. As described in Equation 3.1, a greater distance between these two values indicated higher power consumption.

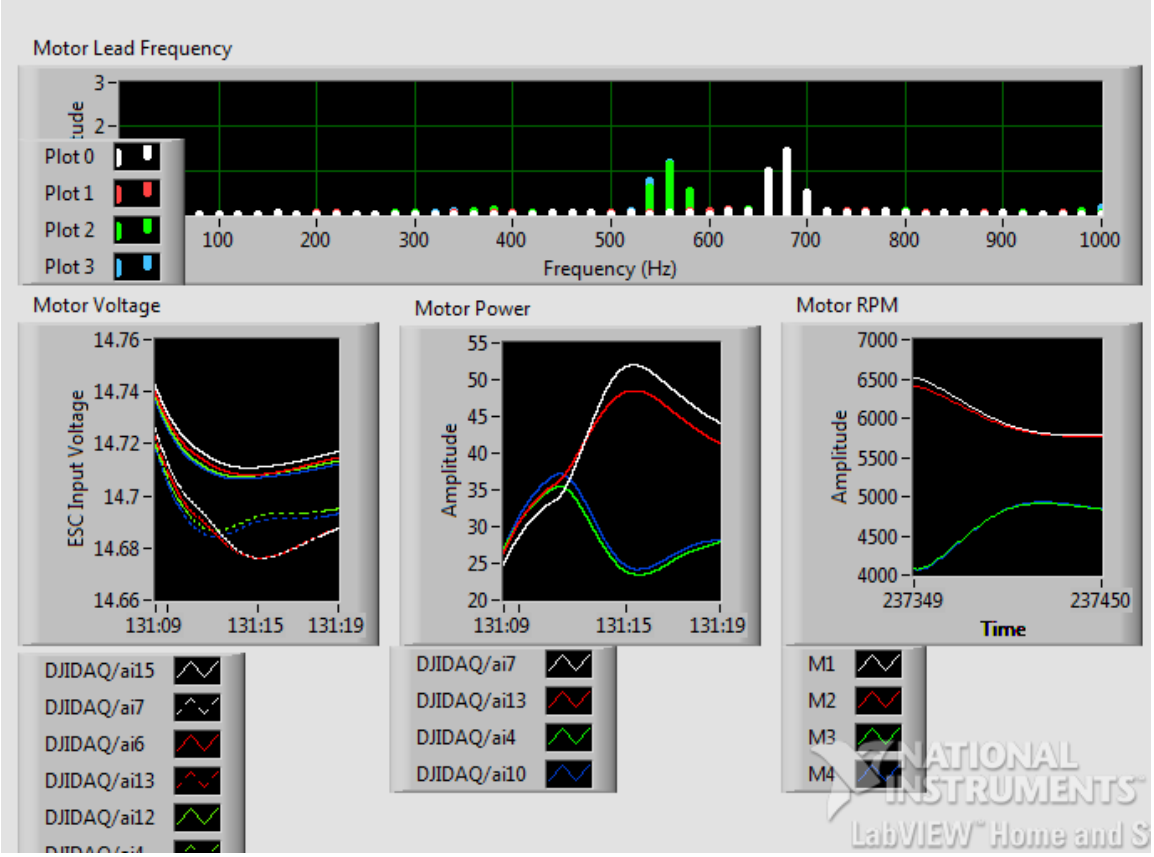

Figure 16. Detail of Sensor Readings Panel During Operation.

Emergency Stop Panel

A large emergency stop button provided rapid shutdown of motors by exiting any ongoing process and repeatedly directing the servo controller board to stop all motors. As a secondary safety measure, test operations could be safely ended by turning off the power supply.

3.3 Signal Processing

Running multiple brushless motors and actuators within the wind tunnel test section resulted in an electrically noisy environment; as such, the raw voltage levels from the signal leads were filtered to recover usable test data. The test setup used both a resistor-capacitor lowpass filter setup as well as a series of lowpass and bandpass filters implemented in the LabVIEW simulation software.

Hardware Filters

The NI DAQ monitoring the test vehicle motor and voltage leads utilized a fairly low sample rate of 4000 Hz to mitigate any settling error caused by the high impedance introduced by the voltage divider boards. This low sample rate was acceptable as the test methodology was to reduce all data taken in a 30 second run to a single averaged value. However, because noise on the signal lines may have a frequency beyond the Nyquist limit of the sample rate, there was a concern of the readings being affected by aliasing of high frequency noise signals. To avoid this, the voltage divider board incorporated a set of 10 nF ceramic capacitors, which together with the first resistor in the divider form a RC-lowpass filter with a cutoff frequency of 1600 Hz.

Software Filters

Raw data readings were further processed by LabVIEW signal filter emulation tools. DC voltage readings from either end of the current sense resistor were run through a lowpass filter to remove the noise caused by the motors. A fairly low cutoff frequency of around 10 Hz was found to provide stable DC voltage readings. The motor switching frequency signals used to determine the motor RPM were run through a bandpass filter; the passband was set by using equation 3.3 to determine the likely range of motor frequencies that would be encountered at the motor RPMs dictated by the test suite. Finally, the force and torque sensor readings from the load cell utilized the default ATI filter method of averaging blocks of data pulled from the data buffer. The filter methods used are tabulated by data type in Table 4.

Table 4. Methods of Software Data Filtering by Data Type.

Data Signal	Filter Type	Details
Motor Voltage	Lowpass Filter	Cutoff: 1 Hz - 10 Hz (Variable)
Motor RPM	Bandpass Filter	Passband: 350-850 Hz
Force Transducer	Averaged Data Set	Set Size: 1000 Samples

Data Logging

Clicking the Record Data button automatically created a text file in the directory specified by the user, with the filename set to the system date and time at the start of the test. Data collected was automatically streamed to the text file – all data types taken at a specific timestep were concatenated into a single row, delimited by tab characters. Time steps were delimited by a new line character. Thus, the resulting data file represented 30 seconds worth of data, with each row representing a specific timestamp and each column representing a specific data type. The first data column was a timestamp consisting of the system uptime in milliseconds.

4. TESTING PROCEDURES

4.1 Development of Test Plan

Development of a test plan had to contend with the large number of potential test conditions and vehicle configurations with a limited amount of time available to test. The primary metrics swept across within the test space were motor speed and vehicle pitch angle. The test matrix consisted of a large number of test runs varying across vehicle pitch angle and motor speeds. The testing process was broken down into several sections covering different test rig configurations or data collection methods. All powered tests were repeated with the motors in their swapped configuration. Two sets of data were gathered for the airframe-only and powered motor tests to provide a means of gauging repeatability. Tunnel speed, pitch angle, and motor speed test inputs were selected to provide similarity to tests performed on the same airframe at NASA Ames [5]. The Ames data provided a reference with which to evaluate the force and torque results from this test program. Across the length of the test program, data was collected from 272 test runs. The test matrix is summarized in Table 5.

Table 5. Test Matrix Summary.

Unpowered Tests	# Data Sets	Tunnel Speed (ft/s)	Vehicle Pitch Angle (Degrees)	Front / Rear Motor Speed (x1000 RPM)
Mounting Hardware Only	1	20	0, -2, -5, -10	-
Airframe Only (Unpowered)	2	20, 40	0, -2, -5, -10, -20, -30	-
Airframe and Props (Unpowered)	2	20	0, -2, -5, -10, -20, -30	-
Powered Tests				
Motor Configuration A - Collective	2	20	0, -2, -5, -10, -20, -30	42/42, 48/48, 53/53, 58/58, 64/64
Motor Configuration A - Cyclic	2	20	0, -2, -5, -10, -20, -30	64/42, 58/48, 48/58, 42/64
Motor Configuration B - Collective	2	20	0, -2, -5, -10, -20, -30	42/42, 48/48, 53/53, 58/58, 64/64
Motor Configuration B - Cyclic	2	20	0, -2, -5, -10, -20, -30	64/42, 58/48, 48/58, 42/64
Z-Height Interference Tests				
Centerline Mounted	1	20	0, -10, -20	42/42, 53/53, 64/64
Centerline + 4"	1	20	0, -10, -20	42/42, 53/53, 64/64
Centerline + 8"	1	20	0, -10, -20	42/42, 53/53, 64/64
Wake Visualization Tests				
Tuft and Smoke Tests	1	20, 40	0, -10, -20, -30	42/42, 53/53, 64/64

4.2 Test Categories

4.2.1 Unpowered Tests

The intention of the unpowered tests was to investigate the aerodynamic properties of the airframe. This test suite was necessitated by unpredictable drift in the load cell measurements. Despite much time-consuming effort, no method of reliably characterizing the nature of this drift was discovered. As such, the

force and torque measurements could not be simply tared with the tunnel off; instead, to mitigate the amount of drift encountered in a test run, the load cell measurements were tared prior to each powered test point. Because this method tared out forces generated by airframe aerodynamics, a suite of unpowered, airframe-only tests was needed to correct for these unaccounted aerodynamic forces. Several examples of the load cell drift behavior are provided in the appendices.

The tests were performed by positioning the test rig and setting force and torque tare with the tunnel off. The tunnel was then turned on and the fan RPM calibrated to achieve the target tunnel speed. After allowing at least 2 minutes for tunnel conditions to settle, data was gathered for a 30 second test run. The test was performed with the propellers mounted and dismounted to evaluate whether the unpowered rotors contributed significantly to the aerodynamic performance.

4.2.2 Powered Tests

The powered tests investigated the aerodynamic properties and power usage of the test rig under powered flight-like conditions. Powered testing followed a generally fixed procedure from test case to test case. With the motors unpowered, the test rig was adjusted to the pitch angle for the test. The load cell measurements were tared and 30 seconds of unpowered data was gathered to provide bias reference data for the powered test. The motors were then set to spin at their prescribed speeds and powered on. After allowing at least two minutes for the tunnel conditions to settle, the Record Data button was pressed and 30 seconds of power-on data was gathered by the LabVIEW control system. At the end of the test the motors were powered off and an additional 30 second set of unpowered data was collected to provide a second bias reference.

Powered tests consisted of two modes of motor operation – for “Collective RPM” tests all motors were run at the same target speed while for “Cyclic RPM” tests the front and rear motor pairs were operated at different target speeds. The naming convention references the common helicopter flight controls for adjusting overall rotor thrust and tilting the vehicle for forward flight. For a fixed-pitch, multirotor vehicle, this vehicle control is managed via adjustments to uniform or differential motor speeds.

4.2.3 Wake Visualization Tests

The wake visualization tests provided a set of photographs detailing the rotor wake behavior of the test rig at different pitch angles, motor speeds, and tunnel speeds. A smaller subset of test input parameters than was used for the powered tests was considered adequate for visualizing general trends of wake behavior. Wake impingement along the ground plane of the tunnel was captured using the tuft board described in Section 3.1.4. Rollup of the wake along the walls of the tunnel was visualized via the introduction of smoke. The test procedure for the visualization tests was similar to the procedure performed for the powered tests with the addition of triggering the mounted cameras during each test run.

4.2.4 Z-Height Tests

The Z-height tests investigated the impact of tunnel interference by adjusting the height of the test rig within the tunnel. Whereas all other test sets were performed with the rotor plane at the centerline of the tunnel, the Z-height tests also investigated performance with the rotor plane 4-inches and 8-inches above the centerline. Since this test set was only intended to infer general trends, the RPM and pitch angle test parameters were limited to three points each to reduce testing time.

4.3 Data Processing

4.3.1 Calculating Test Run Means and Standard Deviations

The test runs provided a set of data files containing 30-seconds worth of filtered test data taken at 50ms intervals. Each set of data had to be reduced to a single value for each data type. The primary method for achieving this was to average all of the recorded data. The standard deviation of each data type was calculated as well to provide a means for establishing the drift and scatter of data points within each test run.

4.3.2 Accounting for Fuselage Weight and Aerodynamics

The custom internal hardware of the test vehicle results in a different overall weight and center of gravity location than a stock DJI Phantom 3. The CG and weight of a stock DJI Phantom 3 are used for calculating primary torques and net lift. The default tare method for the ATI load cell sensor was found to be inadequate as it would simply zero the force and torque readings by the most recent measurement, which didn’t account for noise. To rectify this, the force and torque readings from an unpowered bias run

performed before each test run was used to provide a time-averaged tare for the force and torque data of the powered run. As mentioned in Section 4.2.1, the force and torque data of the powered test runs was tared to the tunnel-on, motors-off condition to mitigate the impact of sensor drift. Processed force and torque data from the unpowered tests was added to the powered test data to account for fuselage aerodynamic forces.

5. RESULTS

5.1 Comparison to NASA Ames Wind Tunnel Data

Data from multirotor tests performed at the NASA Ames Advanced Rotorcraft Center provided a set of independent lift and drag test data with which to evaluate the data from the tests performed at the Cal Poly Low Speed Wind Tunnel lab. A comparison of the lift and drag forces measured in the NASA tests to the forces measured in the Cal Poly tunnel is shown in Figure 17[5]. The NASA data is shown as dashed lines while the polygonal lines represent the spread of data collected in the Cal Poly Wind Tunnel for the Configuration A and Configuration B powered tests. While the force data exhibits similar trends, both lift and drag data collected by the experiments in the Cal Poly tunnel exhibit a lower magnitude across the data set. The primary cause of this discrepancy between the data sets is unknown, however the difficulties encountered with the ATI force transducer throughout testing suggests that the force and torque readings provided by the load cell may not be reliable. An additional significant source of this discrepancy could be the impact of wind tunnel effects on airflow introduced by performing these tests in a wind tunnel with a much smaller cross sectional area. Finally, the actual test parameters of each test condition may not be equivalent across both sets of data; as discussed below, the discrepancies in force and power data suggest the data sets may not share the same set of motor speeds.

A concerning aspect of the test data collected in the Cal Poly tunnel is that a negative drag value was measured at zero vehicle pitch angle, suggesting that the vehicle is producing horizontal thrust when its rotors are not inclined. This suggests that the measured force test data is offset in some manner not accounted for by taring the load cell or biasing for the power-off aerodynamic tests.

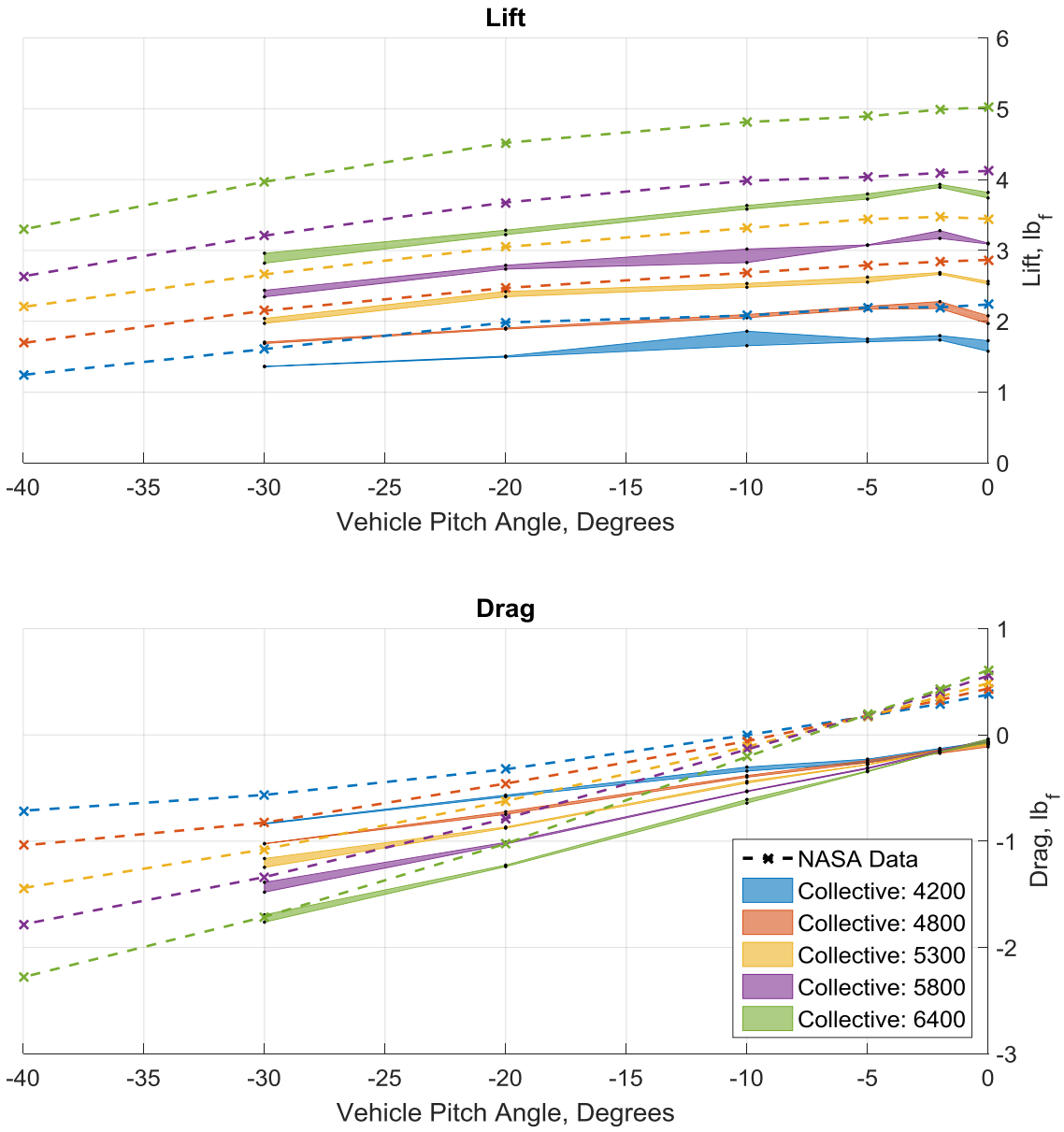

Figure 17. Aerodynamic Test Data taken at NASA Ames and in the Cal Poly Wind Tunnel [5].

A comparison of pitching moments for the same test conditions is shown in Figure 18. The origin of the moments corresponds to the location of an unmodified DJI Phantom's center of gravity. Note that the moment data taken from the NASA Ames test has been translated to this point from its original origin at the center of the rotor plane. As with the force data, a comparison between the two sets of data demonstrates similar trends in pitching moment with rotor speed and vehicle pitch angle, but a marked discrepancy in magnitude. The spread in the data gathered from the Cal Poly wind tunnel tests is representative of the unpredictable behavior of the load cell used for those tests. For a given set of matched motor speeds, the

pitching moment was seen to be greatest at zero-vehicle pitch angle, with the pitching moment trailing off in magnitude as the vehicle is pitched downwards.

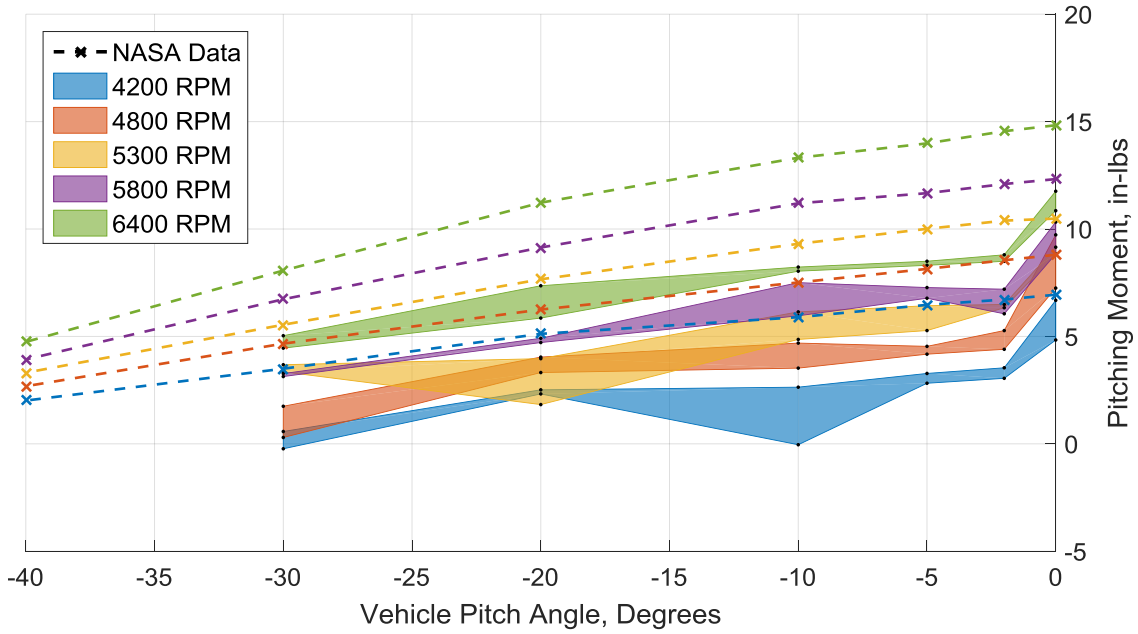

Figure 18. Pitching Moment about the CG Test Data taken at NASA Ames and Cal Poly [22].

The total input power for both the NASA Ames and Cal Poly tests is shown in Figure 19. As with the force data, the data sets demonstrate similar trends in power usage with respect to motor speed and vehicle pitch angle, but at a reduced magnitude. The similarity in this discrepancy between the data sets to the discrepancy seen between force and moment data suggests that these trends may not be coincidental.

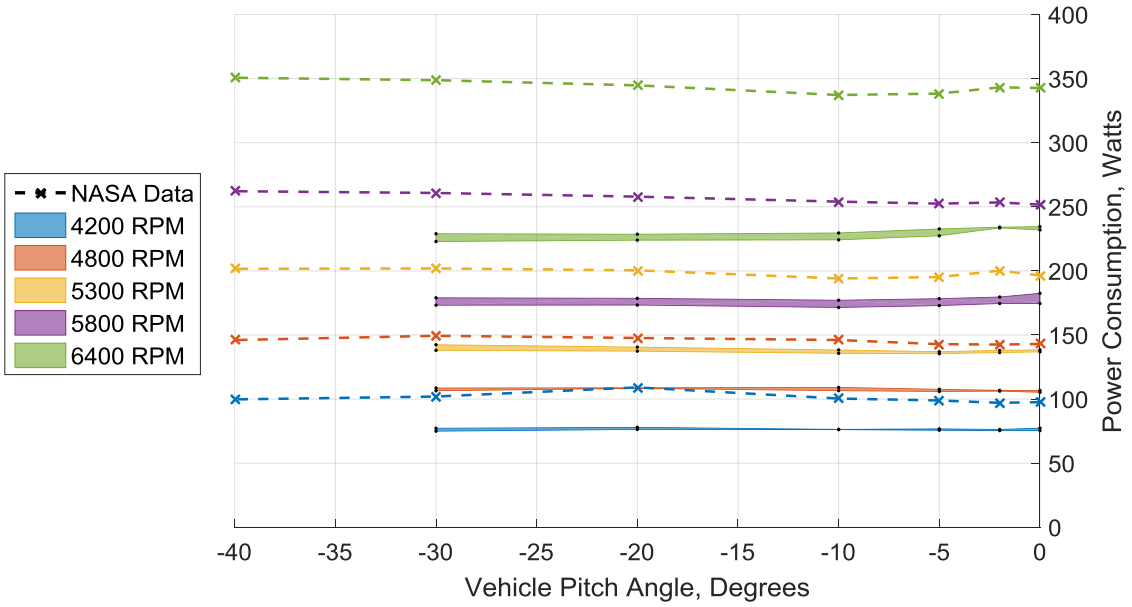

Figure 19. Total Electrical Input Power from NASA Ames and Cal Poly Wind Tunnel Tests [22].

A potential cause of these discrepancies is a mismatch in RPM speeds between the data sets, which would affect both the thrust force and motor input power. However, both the Ames test and this project utilized the commutation frequency of the motor leads to determine RPM and validated the method with measurements taken with an optical tachometer. The primary difference in instrumentation is that the Ames tests utilized an Eagle Tree motor RPM sensor to detect motor speed while this project relied on a LabVIEW FFT tone extractor implementation to calculate the frequency from the raw signal data. Additionally, this project utilized closed-loop control to maintain a target RPM throughout a test run. A discrepancy between the commanded and actual RPM in either data set would explain the consistent disparity between results, but this isn't demonstrable without further testing of both test setups. Further discussion regarding this discrepancy is provided in Appendix A.4.

A comparison of airframe lift and drag data measured in the Cal Poly wind tunnel and at NASA Ames is shown in Figure 20. The lift and drag forces are normalized by the tunnel dynamic pressure, q, because the unpowered airframe-only Ames test were performed at a nominal 1.9 lbs/ft^2 while the airframe tests at Cal Poly were performed at 0.48 lbs/ft^2. Note that the powered tests at NASA Ames were performed at a q of 0.48 lbs/ft^2. The results are not provided in terms of lift or drag coefficient because there is not a standard reference area for this class of vehicle.

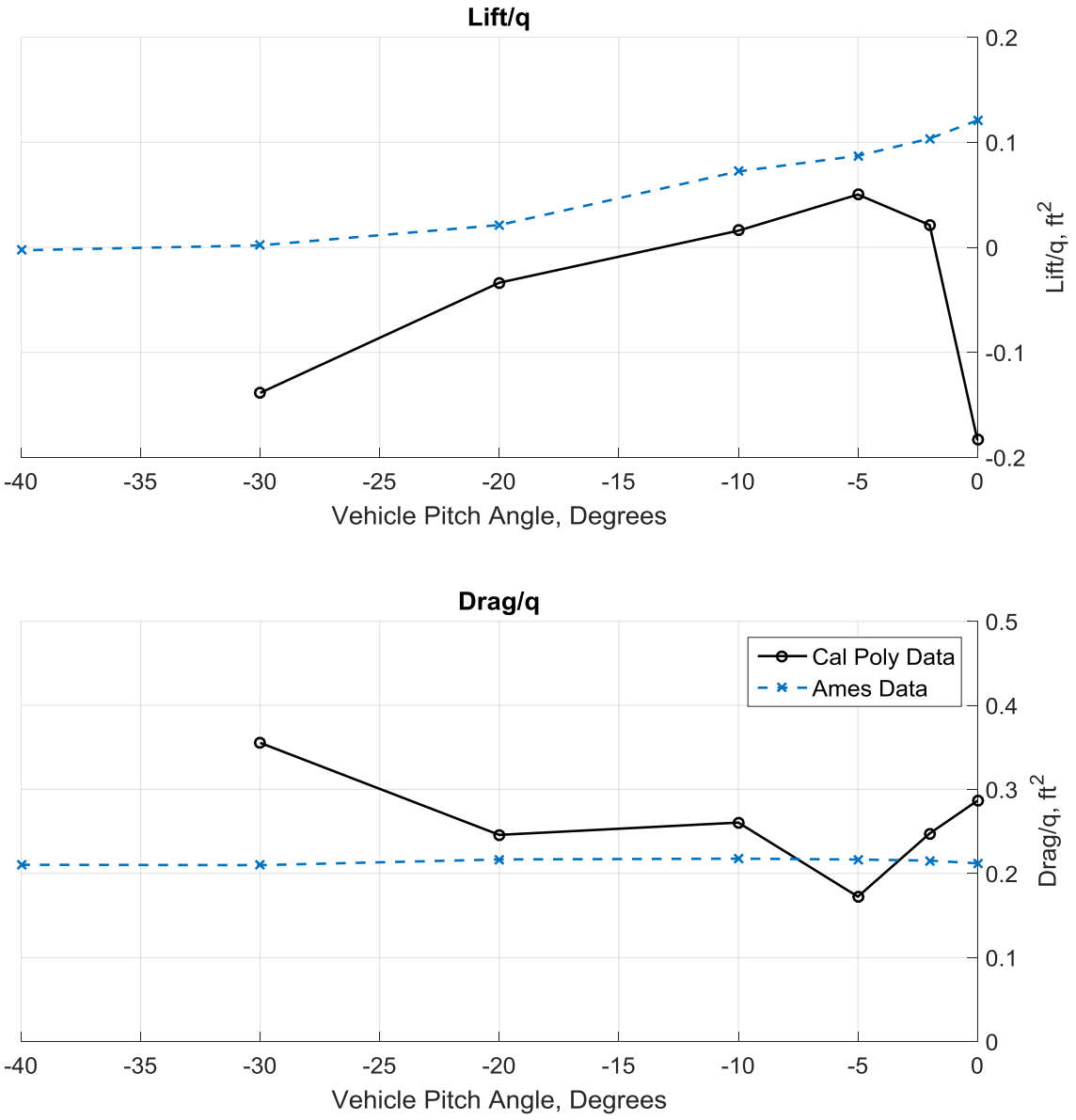

Figure 20. Airframe Lift and Drag Data, Normalized by Dynamic Pressure, taken at NASA Ames and in the Cal Poly Wind Tunnel.

5.2 Vehicle Aerodynamics

5.2.1 Collective RPM Tests

For the Collective RPM tests all motors were commanded to run at the same speed. These tests investigated the impact of vehicle pitch angle on powered lift aerodynamics for a range of motor speeds. Figure 21 shows the net lift (F_z) and net drag (F_X) forces measured with the test rig in both motor placement

configurations. The data shows similar trends to the DJI 3 aerodynamic data gathered at NASA Ames, although as discussed before a significant discrepancy was found in the overall magnitude of forces.

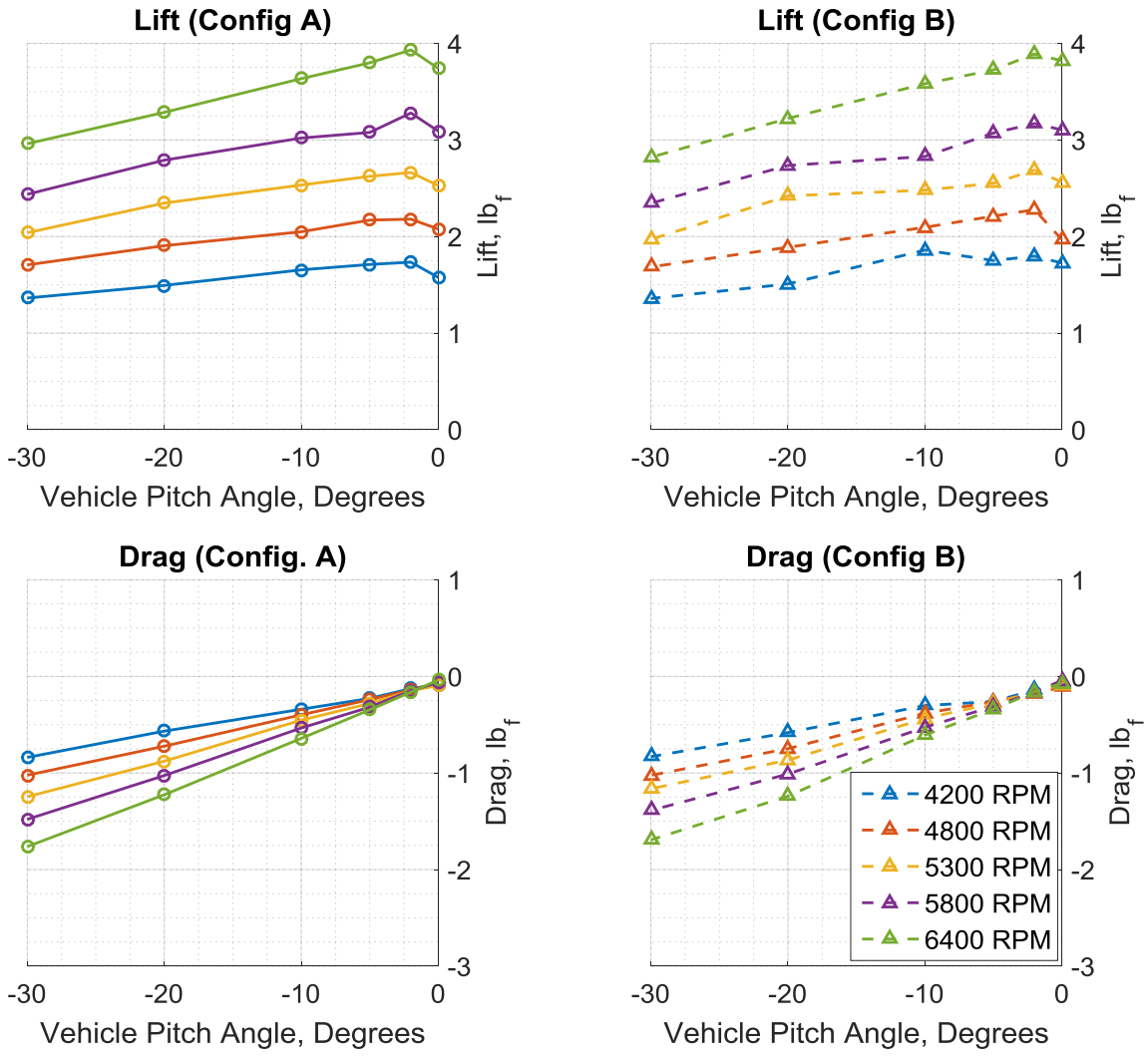

Figure 21. Aerodynamic Forces – Collective RPM Tests.

The effect of pitch angle and cyclic motor speed on the vehicle's pitching moment is shown in Figure 22 for the Collective RPM tests. The origin of the moments corresponds to the location of an unmodified DJI Phantom's center of gravity. The data suggests the vehicle is experiencing a pitch-up moment throughout the set of test parameters. Increasing rotor thrust increased the pitching moment, while pitching the vehicle downwards decreased the pitching moment. Greater variance is seen between the two data sets than was

seen with the force measurements, believed to be caused primarily by the sensitivity of torque measurements to the unpredictable drift behavior of the load cell.

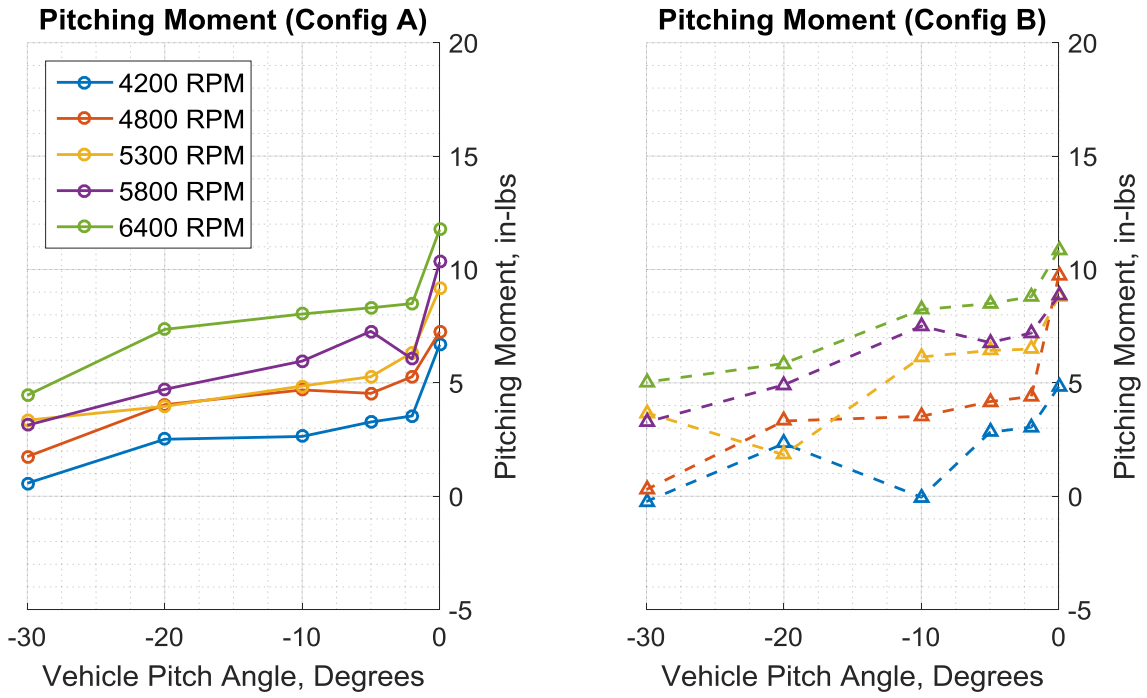

Figure 22. Pitching Moment- Collective RPM Tests.

5.2.2 Cyclic RPM Tests

The Cyclic RPM tests varied the difference in speed between the front and rear motors to investigate the impact of differential thrust on vehicle pitching moment. As seen in Figure 23, varying the front and rear motor speed around a common motor speed did not greatly impact the overall aerodynamic forces on the vehicle. Tests conducted with a common motor speed of 5300 RPM are displayed as the thickened yellow line. The differential thrust tests are distributed around the common collective test point data.

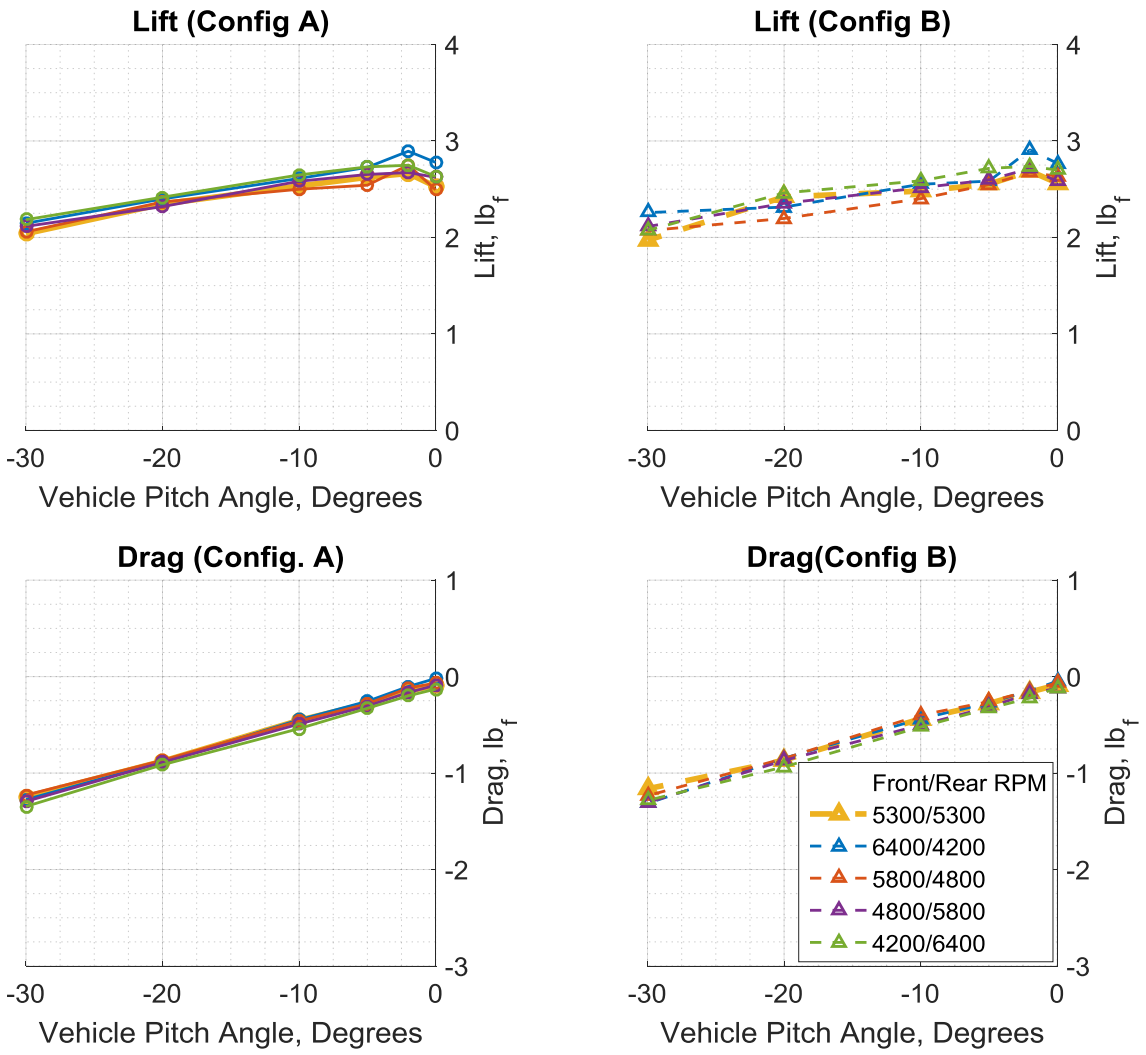

Figure 23. Aerodynamic Forces – Cyclic RPM Tests.

The effect of differential thrust is seen in the pitching moment data shown in Figure 24. As expected, commanding the forward motors at a higher speed than the rear motors increases the pitch-up moment, whereas a thrust distribution heavily weighted towards the rear rotors results in a pitch-down moment. A trend is seen that pitching the vehicle downwards reduces the upwards pitching moment.

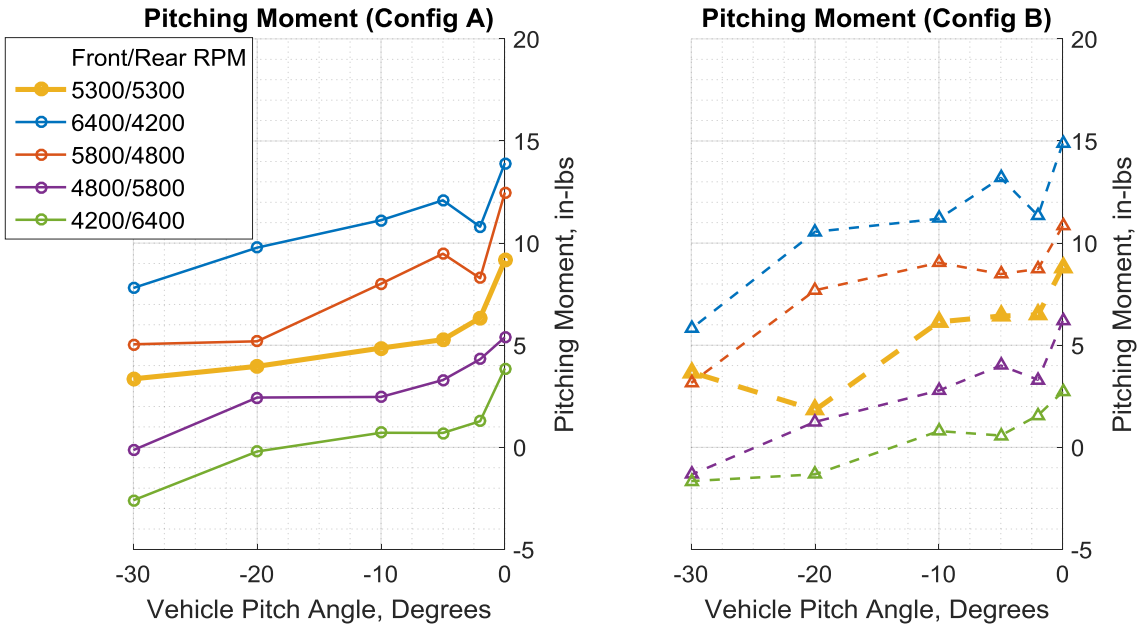

Figure 24. Pitching Moment – Cyclic RPM Tests.

5.3 Power Usage

Electrical input power to the test rig was calculated by measuring the voltage and current fed into each of the four ESC-motor-rotor pairs. This setup allowed power input to each pair to be measured independently. Determining the breakdown of power usage between power delivered to the rotor and power loss in the ESC and motor is well beyond the capability of this test rig; thus, note that "motor power" in the context of this project refers to the DC input power at a single ESC.

5.3.1 Total Power Usage

Total power usage was calculated by summing the power use of each of the four motors. Power usage from the Collective RPM tests is shown in Figure 25 for both Configurations. The Configuration B tests consistently demonstrated lower overall input power than Configuration A for the same test settings at 5300 RPM and above. This is due to Motor 1 and Motor 2 using significantly less power in the Configuration B tests, but Motor 3 and Motor 4 using approximately the same amount of power in both configurations. This asymmetrical behavior was unexpected and the cause for it is unknown, but is possibly due to the current sense resistors or voltage divider drifting out of calibration in the interim between the tests. Power Usage

per Motor plots are provided in the appendix. Total vehicle input power was not highly sensitive to vehicle pitch angle, although high RPM cases consumed more power with the vehicle at the near-horizontal.

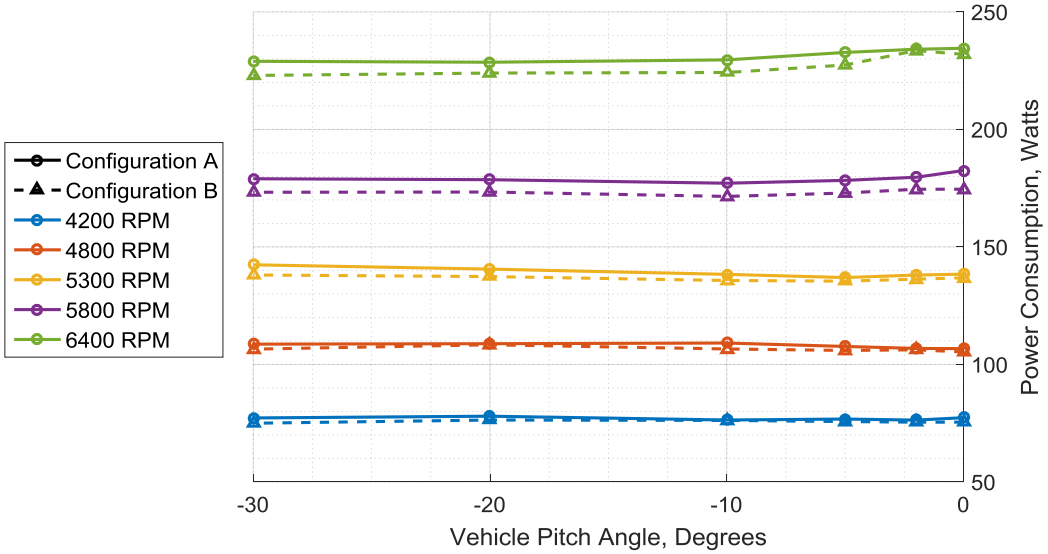

Figure 25. Total Vehicle Input Power – Collective RPM Tests.

Total power usage from the cyclic power tests is shown in Figure 26. Note that the power axis has been rescaled for the smaller range of power measurements. As with the collective RPM tests, total power usage was not highly sensitive to pitch angle, except at low angles of attack, where the front-biased cyclic RPM settings demonstrated an uptick in power usage and the rear-biased tests demonstrated a small decrease in power.

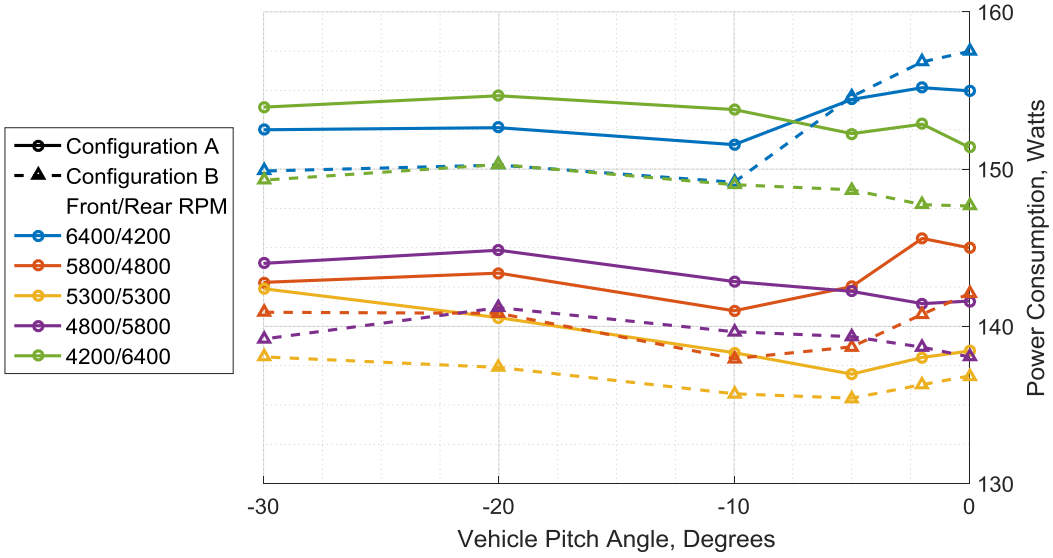

Figure 26. Total Vehicle Input Power – Cyclic RPM Tests.

5.3.2 Power Usage per Motor

Each ESC-motor-rotor pair draws a slightly different power under equivalent test conditions due to unique variations between components, such as manufacturing tolerances resulting in different motor friction losses and propeller geometry. This hardware variation makes it inadvisable to determine motor performance trends by comparing performance between different motors, as the unique physical properties of each component contribute to measurement uncertainty. The impact of rotor position on motor input power can be evaluated by comparing the relative performance of the same ESC-motor-rotor pair when mounted in different positions on the vehicle. In Figure 27 the power draw of each ESC-motor pair is presented as a fraction of the overall vehicle power usage. A general trend can be seen that for a given RPM at low pitch angles, the rear mounted motors account for most of the vehicle's input power, while at large pitch angles the front motors use more power. The effect of motor position on fractional power usage is greatest for Motor 1, with a maximum change in fractional power usage of 1.45%. The crossover point at the nominal test airspeed of 20 ft/s is at a pitch-down angle of around 18°.

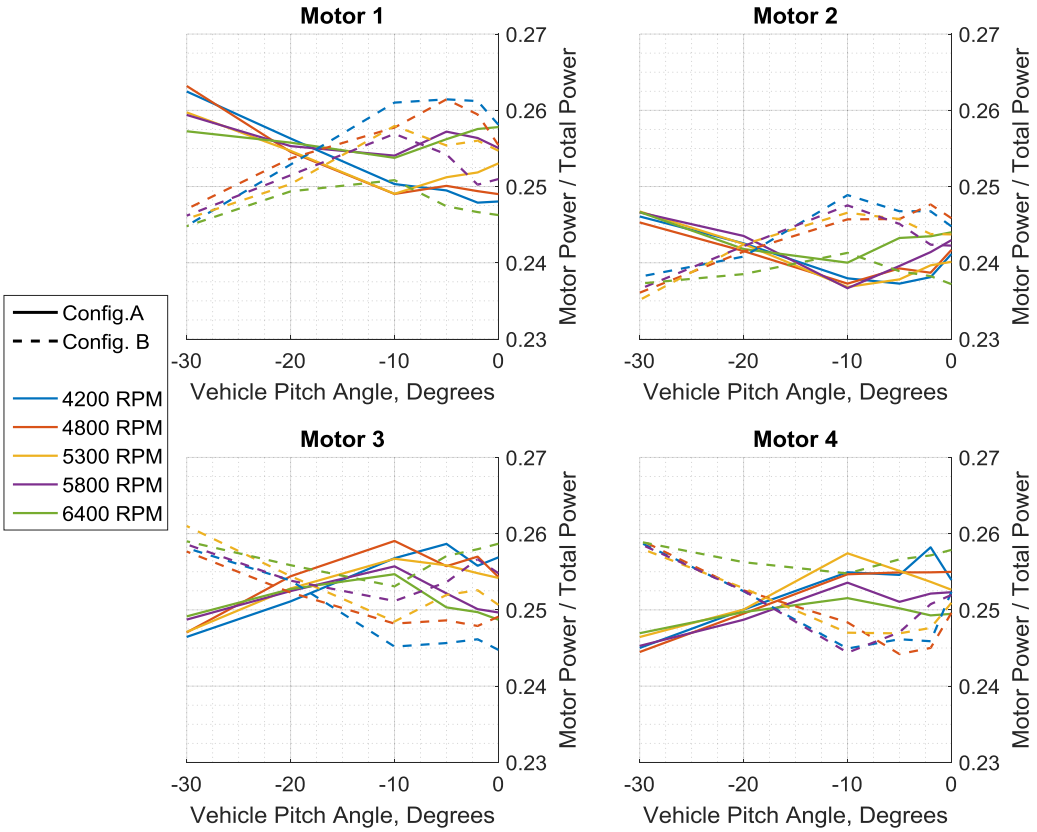

Figure 27. Motor Power as a Fraction of Total Input Power – Collective RPM Tests.

Motor power as a fraction of total input power is shown for the Cyclic RPM tests in Figure 28. As expected, the primary driver of relative motor power usage is RPM, with the fastest driven motors consuming proportionally more power. The trend seen in the Collective RPM tests is echoed here, with the motors consuming proportionally more power when in the front mounted position as the vehicle downward pitch angle increases.

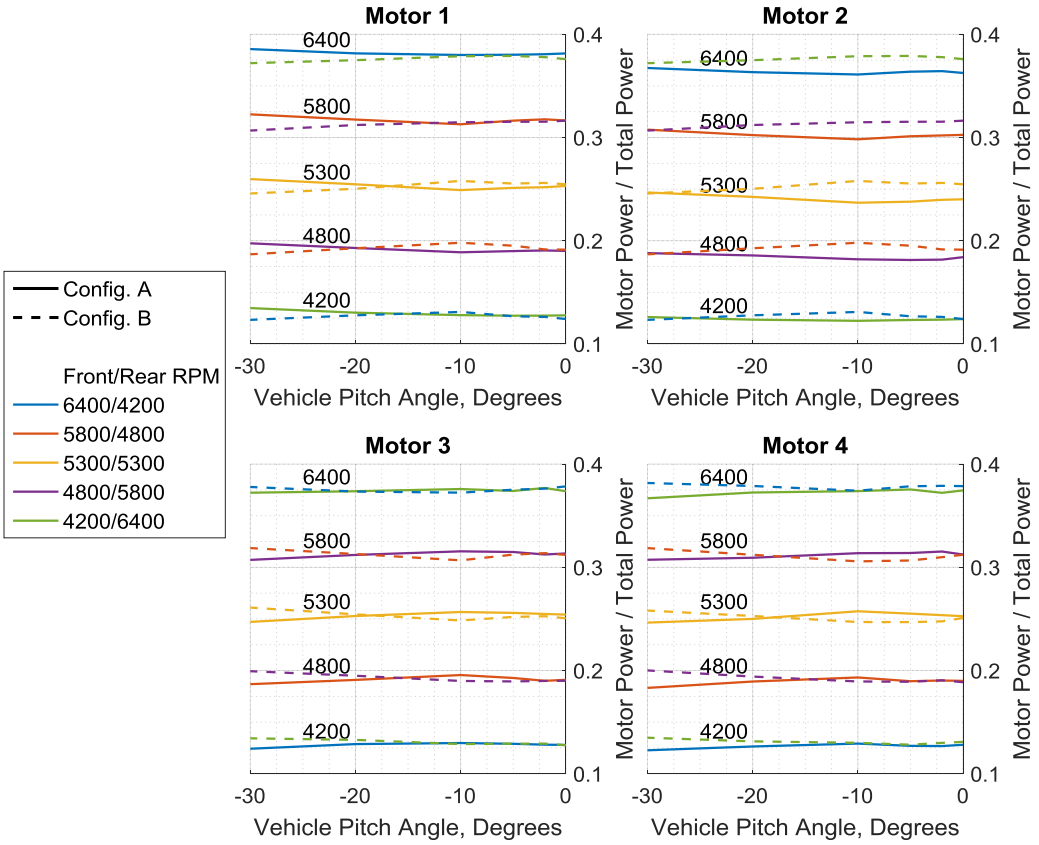

Figure 28. Motor Power as a Fraction of Total Input Power – Cyclic RPM Tests.

5.4 Estimating the Equivalent Lift-to-Drag

The equivalent lift-to-drag metric described in Equation 2.7 is only valid at the operating point where the net primary forces and moments are all zero. Within the constraints of this project, a steady-level flight-like condition is identified as an operating point where the F_Z, F_X, and T_Y forces are near-zero. Contours were generated for the net lift (F_Z), drag (F_X), and pitching moment (T_Y) data across the vehicle pitch angle and motor speed test space.

The F_Z and F_X force contours from the NASA Ames test data are shown in Figure 29. Because of the low fidelity of the test space, a linear interpolant method was needed to generate enough sample points to generate legible contours. The zero-net force contour indicates that the trim condition is satisfied along that primary axis. These contours are overlaid in Figure 30 along with a red circle indicating the point within the test space at which both the net lift and net drag forces are zero.

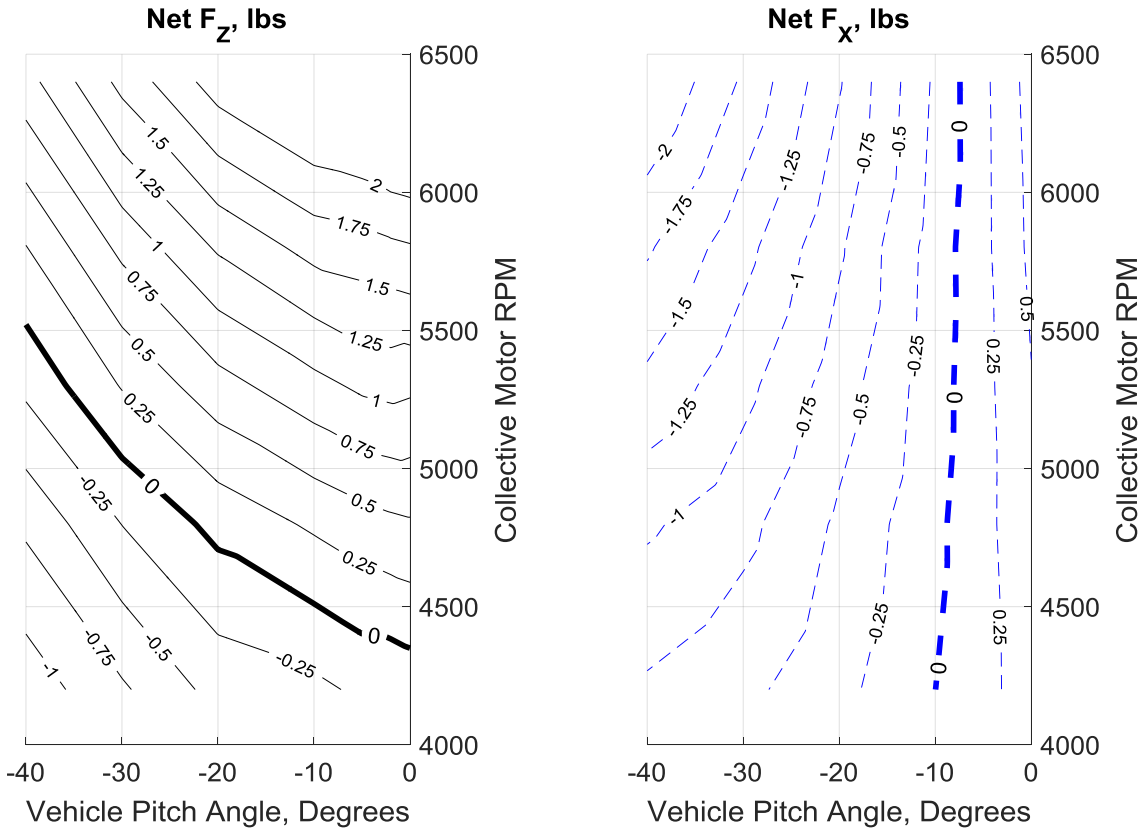

Figure 29. Contours of Net F_Z and F_X Forces Across Test Space (NASA Ames Tests) [5].

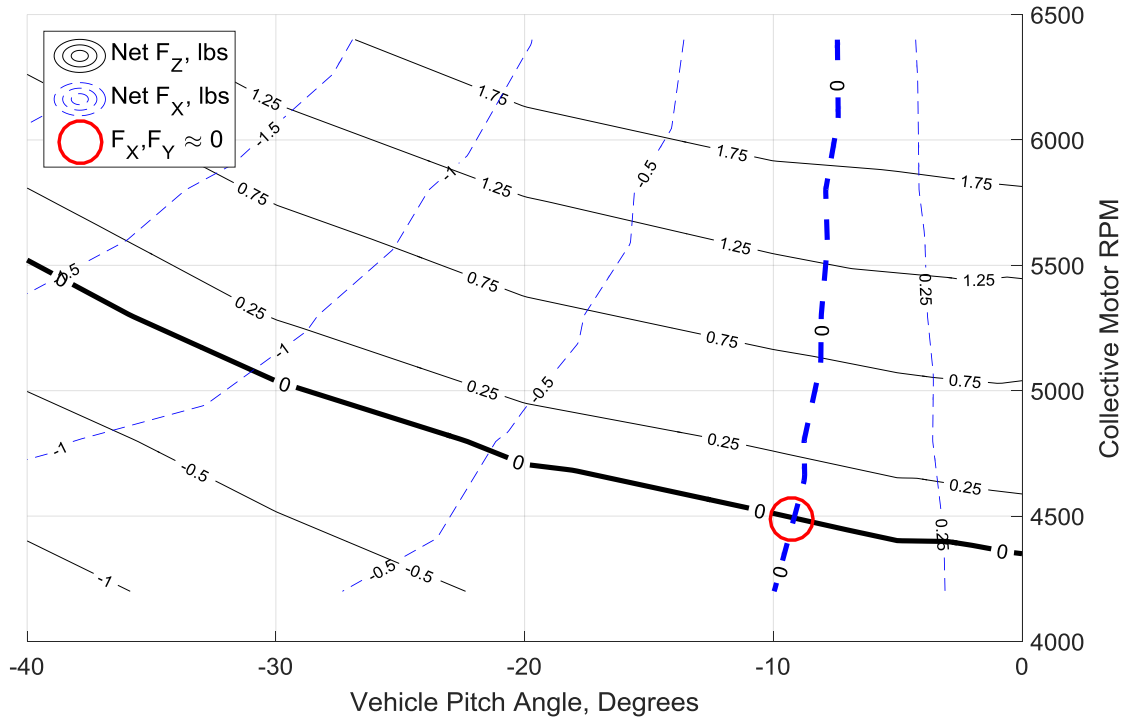

Figure 30. Net Force Contours across Test Space (NASA Ames Tests) [5].

As demonstrated in Section 5.1, all of the Collective RPM data points from the Ames tests had a net positive pitching moment, indicating that the vehicle did not satisfy all of the trim conditions at any point within the test space. However, if an assumption is made that offsetting the uniform RPM of the front and rear rotors by equivalent and opposite amounts doesn't greatly change the overall vehicle power usage, than the Collective RPM test data can be used to estimate the power required to maintain a 20 ft/s steady, level forward flight. The corresponding input power contours for the NASA Ames Collective RPM tests are shown in Figure 31. The red circle indicates the zero force contour convergence location within the test space. Under the assumption that the uniform RPM tests provide an acceptable approximation for the power required to maintain steady, level flight, the Ames data indicates that the vehicle requires 122 W to maintain a forward flight speed of 20 ft/s. Based on Equation 2.7 and a vehicle weight of 2.82 lbs, at this speed $L/D|_{Eq}$ is approximately 0.63.

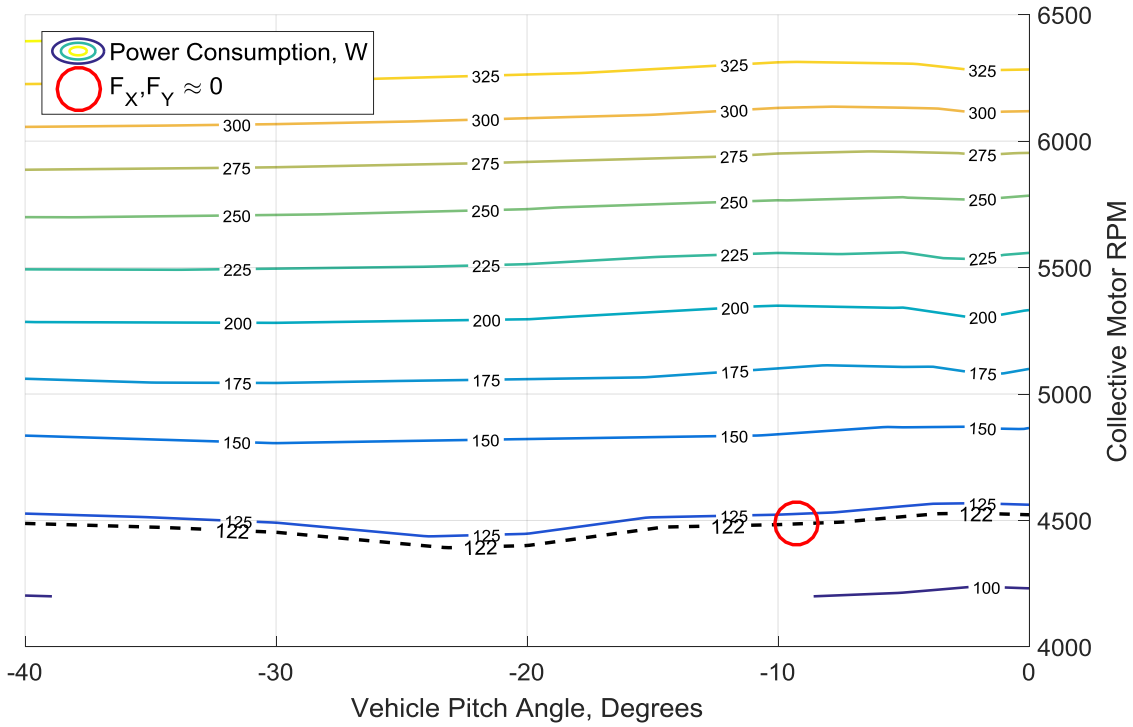

Figure 31. Input Power Contours across Test Space (NASA Ames Tests) [22].

The corresponding data from the Configuration A Collective RPM tests performed in the Cal Poly Low-Speed wind tunnel is shown in Figure 32. The F_Z and F_X contours present similar trends as before, but the contour minimums are shifted relative to the NASA tests. The negative drag at 0° pitch angle seen in the force plot data manifests itself here as the zero F_X contour not being encompassed by the test space. Considering the unlikelihood of the vehicle exhibiting a net forward force when at 0° pitch angle, the F_X data should be considered erroneous. The magenta contours represent the pitching moment data across the test space; as was seen in Figure 22, there was no zero-pitching moment point within the Collective RPM test space. The coincident point of the principal force minimum contours is marked by a red circle.

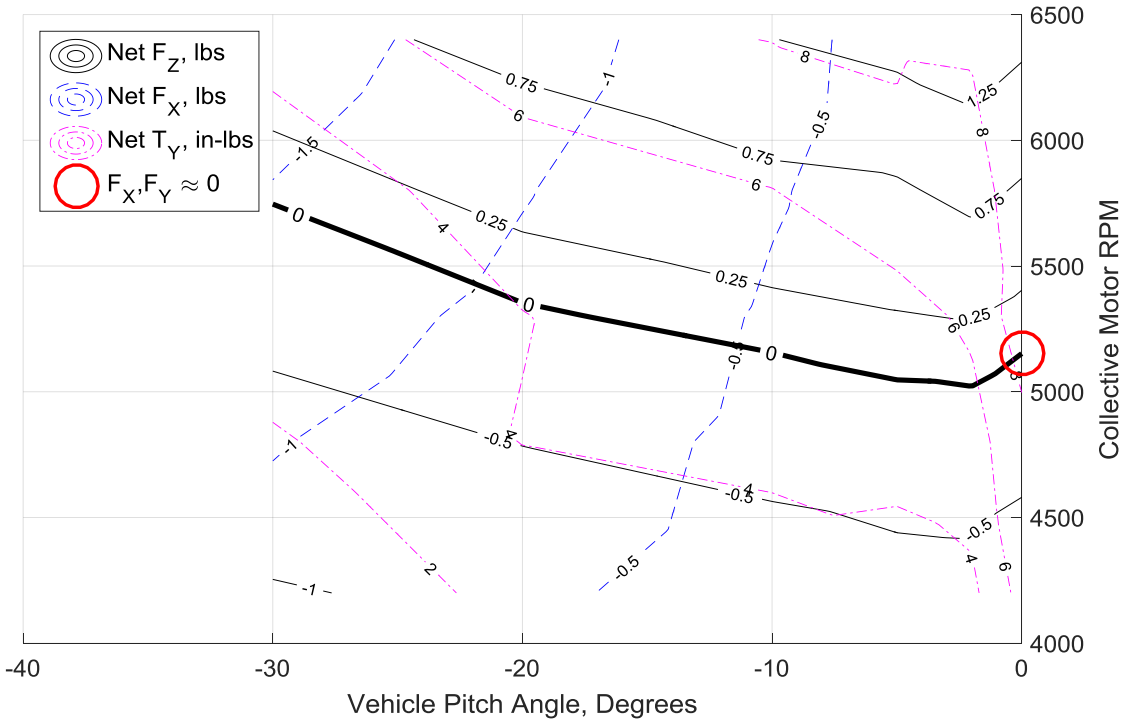

Figure 32. Net Force and Pitching Moment Contours across Test Space (Collective Tests).

Power contours across the test space for the Configuration A Collective RPM tests are shown in Figure 33. Under the same assumption as before that the Collective RPM tests provide an adequate approximation of the power required to trim the vehicle in steady, level flight, the test data gathered in the Cal Poly wind tunnel indicates an a power draw of 129 W and a $L/D|_{Eq}$ of approximately 0.59 at an airspeed of 20 ft/s.

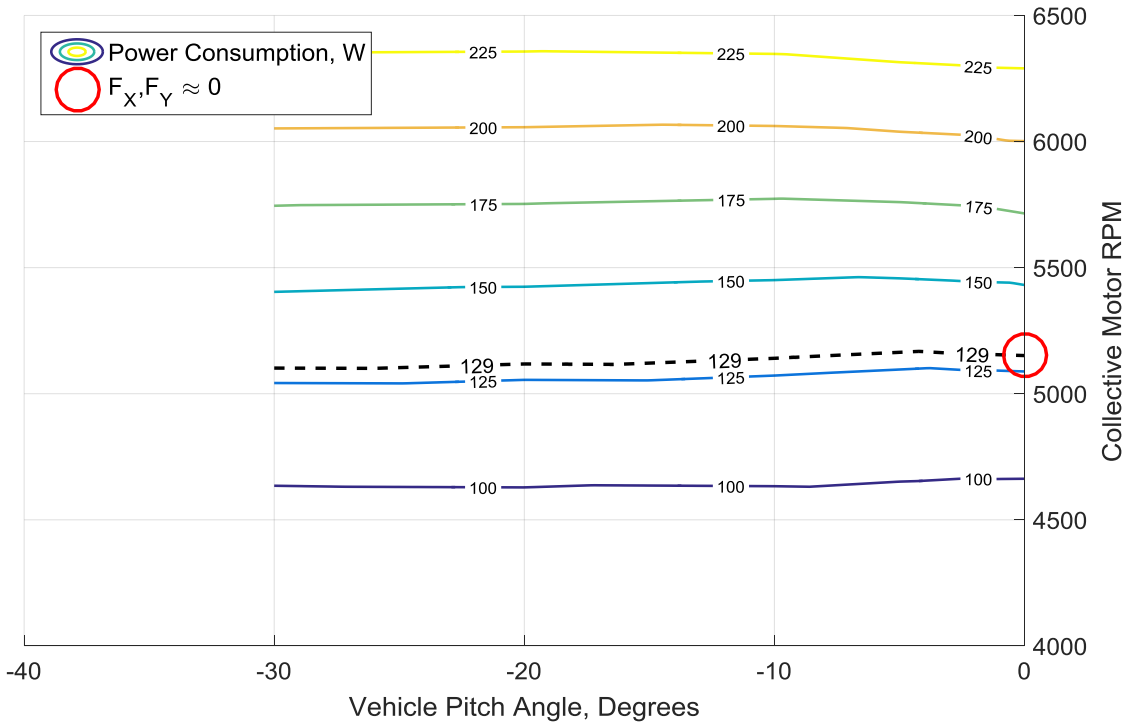

Figure 33. Net Force Contours across Test Space (Collective Tests).

Force and pitching moment contours for the Cyclic RPM tests are shown in Figure 34. Note that the y-axis on this figure describes the RPM differential between the front and rear motors. No zero-net force coincident point was found within the test space; however, the zero-net lift and pitching moment contours have an intercept at -20.5° vehicle pitch angle with the front motors at 4280 RPM and the rear rotors at 6320 RPM, indicating a flight state under which the vehicle would be flying level, but accelerating forward. Because no zero-force contour intercept could be found within this test space, no attempt was made to approximate equivalent lift-to-drag ratio.

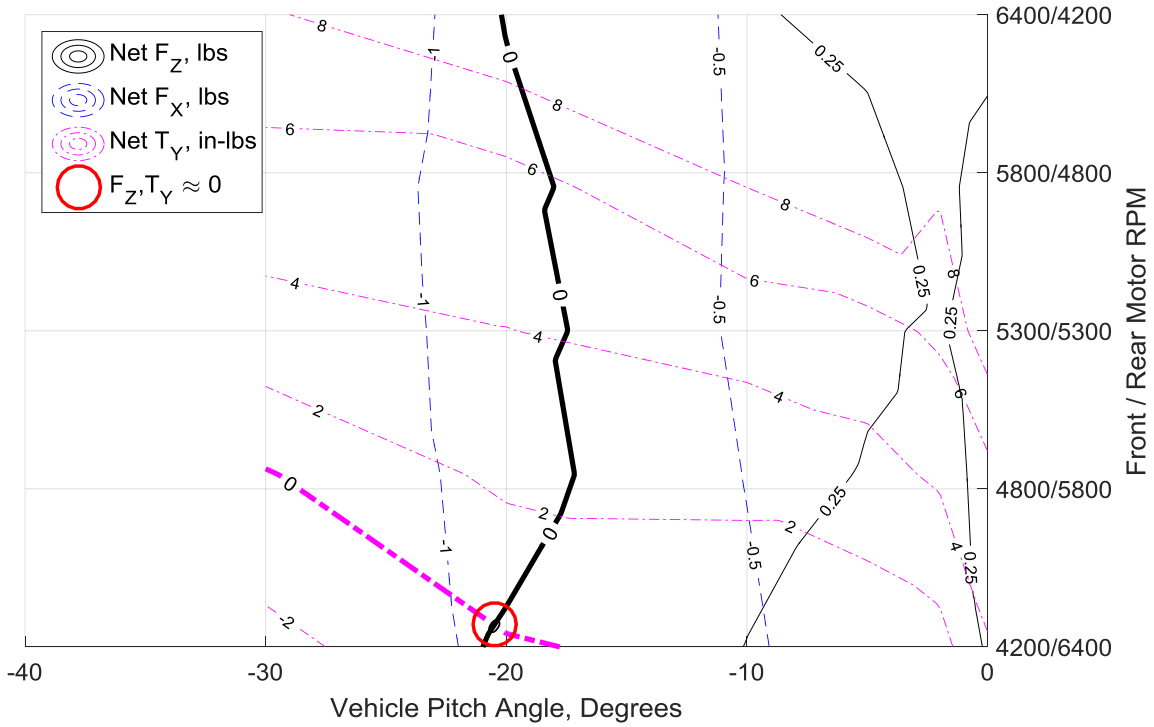

Figure 34. Net Force and Pitching Moment Contours across Test Space (Cyclic Tests).

5.5 Wind Tunnel Interference Tests

5.5.1 Z-Height Tests

The Z-Height tests were an attempt to better characterize the effect of tunnel interference on the results of the powered motor tests. The tests consisted of a subset of the powered motor tests repeated with the rotor plane at different heights above the tunnel floor, providing an indication of how vertical positioning of the vehicle affected the strength of tunnel interference effects.

The effect of vehicle mounting height on lifting force is shown Figure 35. Change in lifting force with vehicle mounting height is most pronounced when the rotor plane is horizontal. Mounting the vehicle with the rotor plane at centerline resulted in higher lift measurements than when the rotor plane was 4-inches above centerline. This is possibly a ground-effect-like phenomenon boosting the effective lift produced. However, with the rotor plane at 8" above centerline there is no consistent trend in lifting forces relative to a centerline mounting, possible indicating a rotor inflow interference effect along the tunnel ceiling. Pitching the vehicle forward greatly diminishes the effect of vertical mounting position on the measured lift forces. The effect of vehicle mounting height on pitching moment is shown Figure 36. The pitching

moment data exhibits similar trends as the lifting force to rotor plane height above centerline. The effect of vehicle mounting height on total input power is shown Figure 37. Additional plots demonstrating the effect of rotor plane Z-height on test measurements are provided in the appendix.

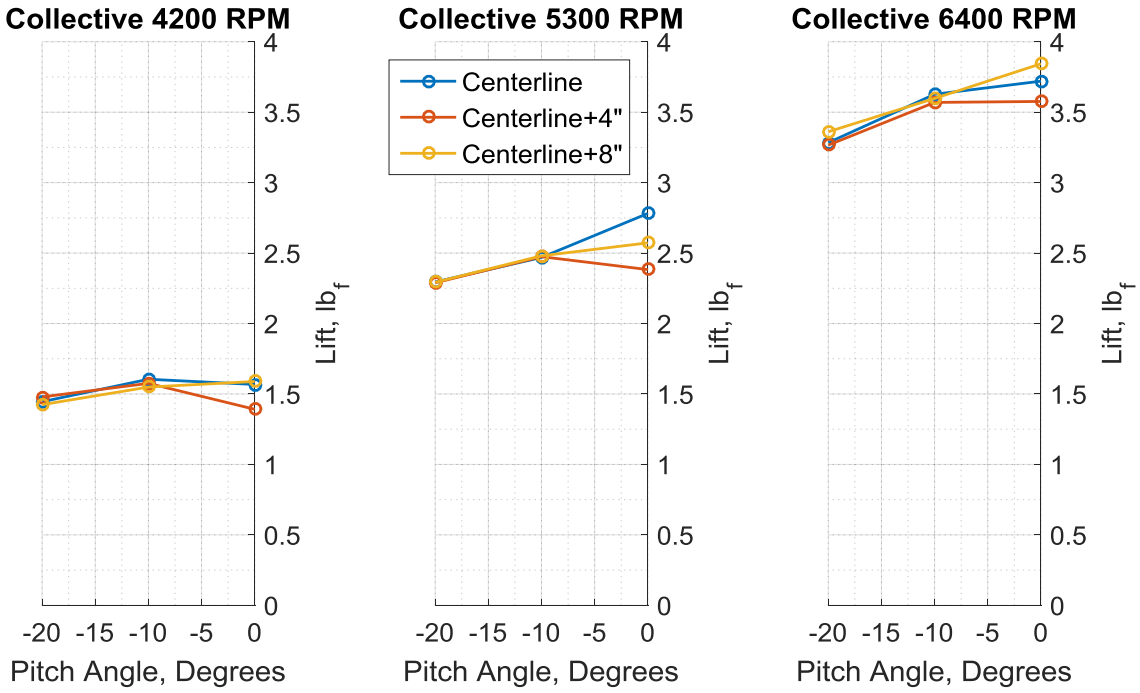

Figure 35. Effect of Rotor Plane Z-Height on Lifting Force.

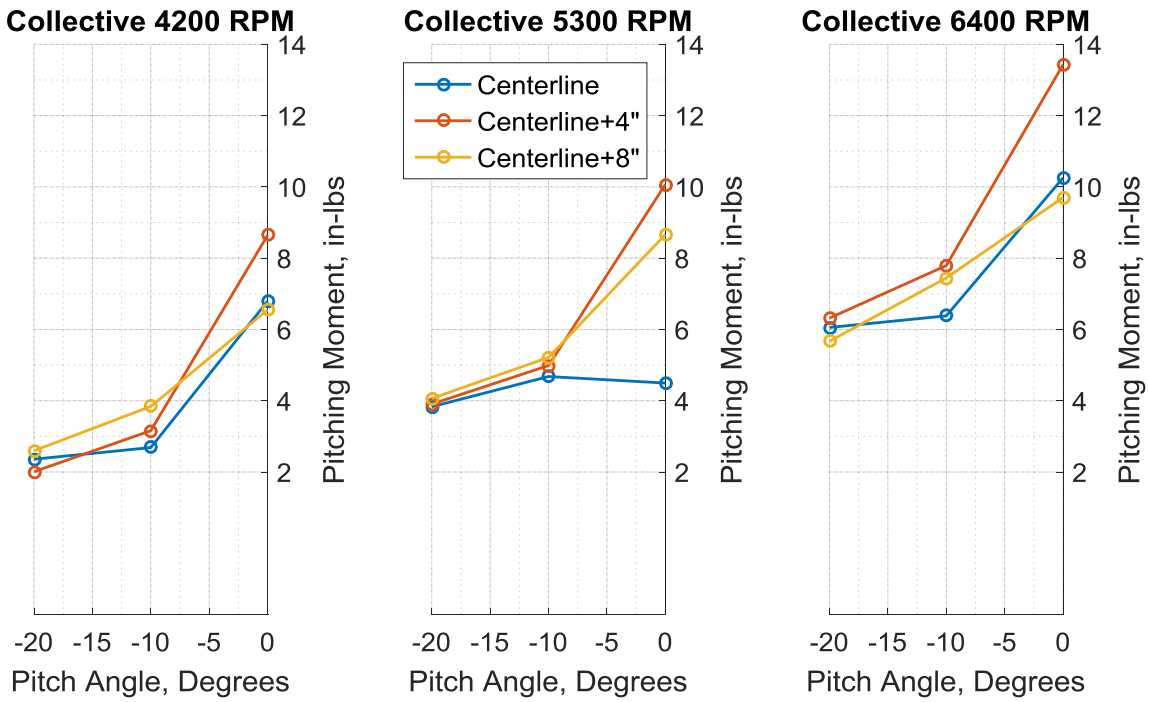

Figure 36. Effect of Rotor Plane Z-Height on Pitching Moment.

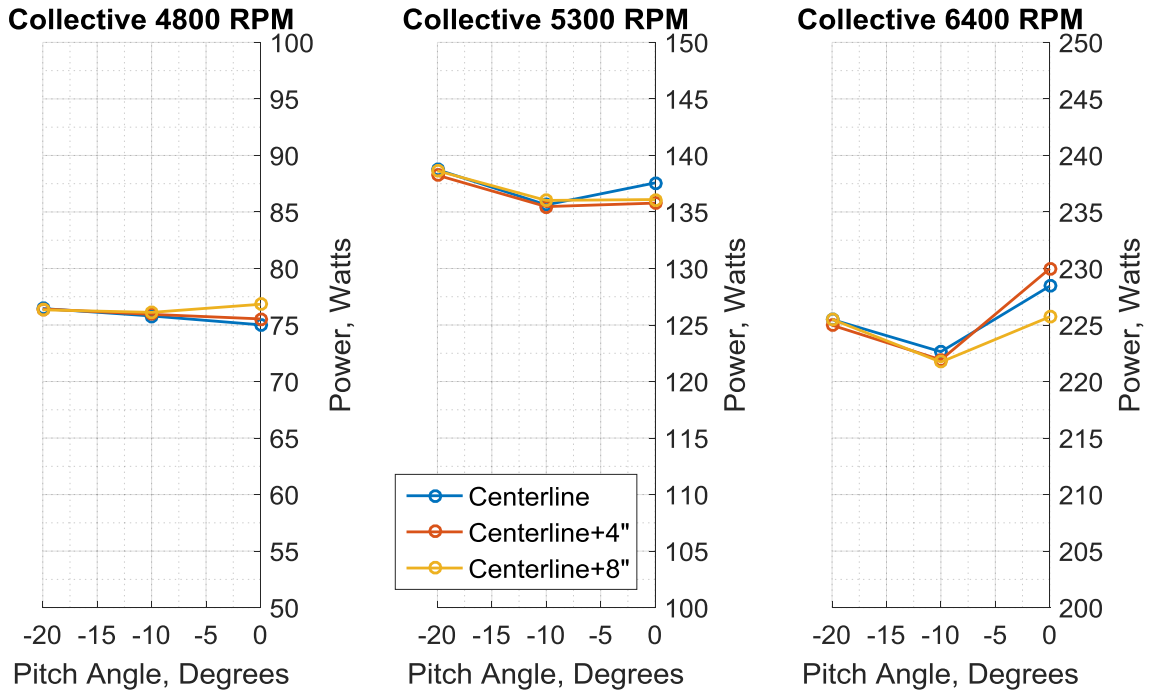

Figure 37. Effect of Rotor Plane Z-Height on Total Input Power.

5.6 Airflow Visualization

The smoke and tuft tests were a series of powered tests attempting to better characterize the nature of the rotor wake when constrained within a wind tunnel. The floor tufts provided a means for estimating the location of wake impingement on the tunnel floor, which can provide an indication of the strength of tunnel interference effects. Deflection and dispersal of a smoke slipstream by rotor wake rolling up the tunnel walls also provided a qualitative measurement of the strength of tunnel interference and provided understanding of the nature of flow in the tunnel aft of the test vehicle.

5.6.1 Tuft Visualization of Rotor Wake

Hardware for the tuft tests consisted of two 2 by 4-foot, 1/16-inch plyboards with a smooth, white enamel surface. Tufts of red yarn 3-inches long were taped to the board at 3-inch increments. As seen in Figure 38, the tufts are aligned with the tunnel flow when the motors are not powered. Note that the front of the tuft board is at the same x-axis position as the front edge of the forward motor disk planes. An outline of the test vehicle, as seen from above, is overlaid approximately where the test vehicle was mounted above the tuft boards. Note that the lighting conditions caused the test rig's shadow to be offset from its actual position over the tuft boards.

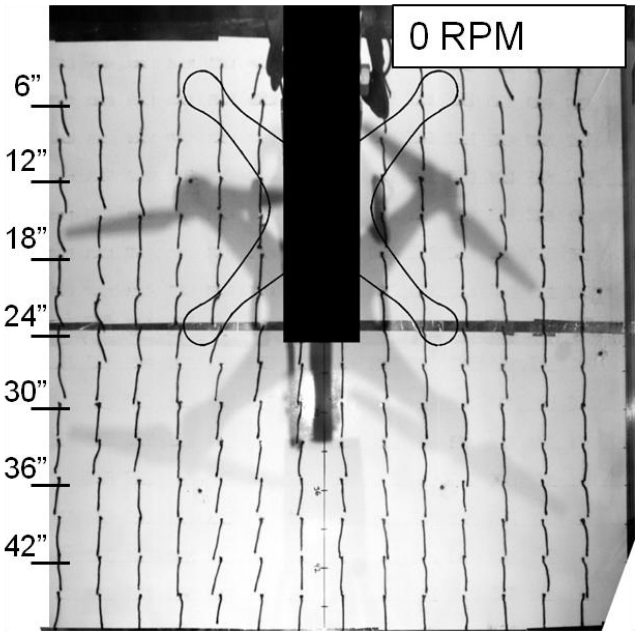

Figure 38. Position of Floor Tufts with Motors Off.

With the motors powered on, rotor wake impinges on the tunnel floor and flows backwards and outwards towards the walls, which causes the tufts to deflect. The angle between the rotor axis and the direction of the wake stream tube is known as the rotor wake skew angle. The wake skew angle is determined by the momentum exchange between the tunnel flow and the wake flow, with an increase in rotor thrust relative to the speed of the tunnel decreasing the wake skew angle and vice-versa. Within the confines of a wind tunnel test section, the wake skew angle and the height of the model determine how far back from the rotor the wake will impinge on the tunnel floor, and how much energy the wake will have when it reaches the floor. Increasing rotor thrust therefore decreases the wake skew angle and causes both greater tuft deflection and tuft deflection to occur further upstream within the test section. These visual flow effects can be understood to correspond to an increase in the impact of tunnel wall effects on any aerodynamic data collected for that test state.

Tuft deflection at several collective motor speeds with the vehicle rotor plane at the centerline of the tunnel and at a pitch angle of 0° can be seen in Figure 39. The tunnel airspeed is at a nominal 20 ft/s (q = 0.48 lb/ft^2). Increasing the motor RPM - and resulting rotor thrust - both increases the magnitude of tuft deflection and moves the wake impingement location upstream. At 6400 RPM, the wake appears to be impinging on the floor only about 12-inches behind the leading edge of the front rotor disks.

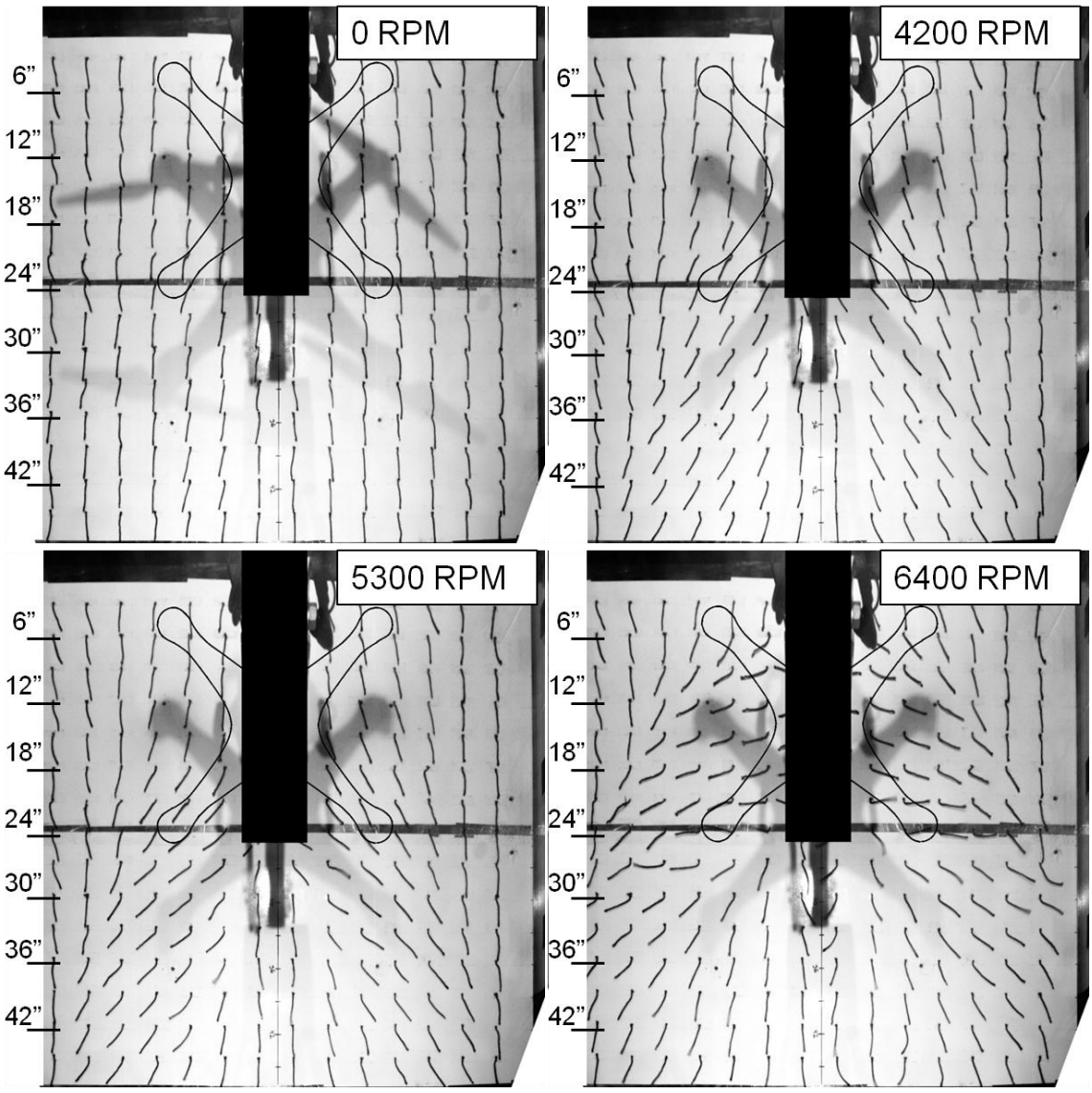

Figure 39. Effect of Motor Speed on Wake Impingement Location at 0° Vehicle Pitch Angle.

Figure 40 shows tuft deflection at a collective motor RPM of 6400 across several vehicle pitch angles. Pitching the vehicle forward tilts the rotor plane and corresponding wake off the vertical axis of the tunnel, which moves the wake impingement location further downstream along the tunnel floor.

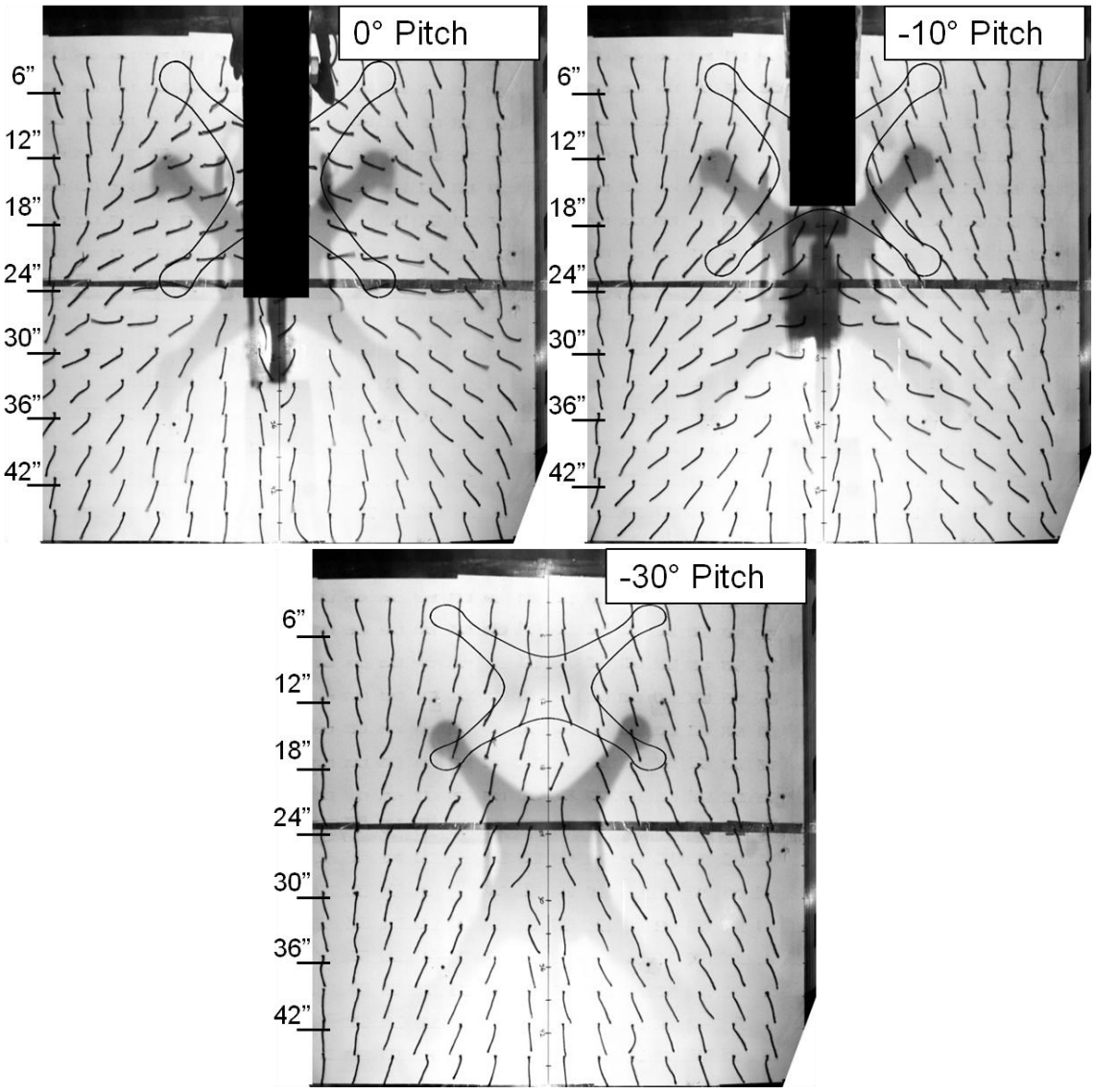

Figure 40. Effect of Vehicle Pitch Angle on Wake Impingement Location at 6400 RPM.

Since the wake skew angle is determined from the momentum exchange between the rotor wake and the oncoming flow, increasing the dynamic pressure of the tunnel airflow will increase the wake skew angle and move the wake floor impingement location further downstream. As seen in Figure 41, at 0° pitch angle and a motor RPM of 6400, increasing the tunnel from a nominal airspeed of 20 ft/s (q = 0.48 lb/ft^2) to 40 ft/s (q = 1.90 lbf/ft^2) moved the rotor wake floor impingement location beyond the distance of the tuft boards – at least 4-feet downstream of the front rotors.

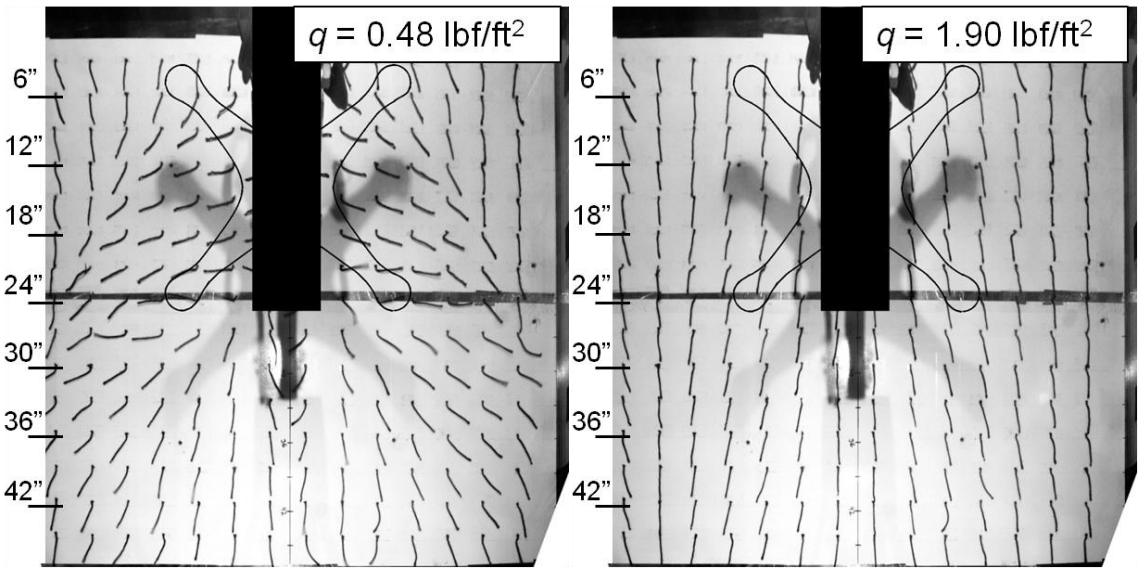

Figure 41. Effect of Tunnel Speed on Wake Impingement Location at 0° pitch and 6400 RPM.

These tests suggest that a subset of multirotor flight conditions can be investigated even in a relatively small tunnel without violating a threshold of rotor wake impingement-induced tunnel interference by carefully balancing the motor speed, vehicle pitch angle, and tunnel speed test inputs.

5.6.2 Smoke Visualization of Rotor Wake

As discussed in Section 2.1, after impinging on the tunnel floor the rotor wake spreads out towards then up the tunnel walls behind the test vehicle. An attempt was made to evaluate this behavior for the quadcopter tests through the use of smoke streamlines. A smoke trail was introduced to the tunnel along one tunnel wall, at approximately the midway point between the rotor disc and the tunnel floor. Rotor wake flowing up the walls of the tunnel demonstrates the relative strength of wake recirculation behind the model.

Figure 42 shows the deflection of the smoke streamlines at different collective RPM settings with wind tunnel at a nominal airspeed of 20 ft/s and the vehicle at a 0° pitch angle. The red lines indicate the centerline of the smoke stream for each test. Increasing the RPM was seen to cause the streamlines along the tunnel wall to deflect more sharply, with smoke reaching the top of the tunnel at the rear of the test section in the 6400 RPM test. Deflection of the slipstream is seen forward of the model, indicating that the wake recirculation effect is strong enough to influence airflow forward of the model. No full recirculation

and subsequent rotor wake ingestion is seen in any of the tested cases; however, the low volume of smoke and turbulent tunnel flow made visualization of tunnel flow phenomena difficult.

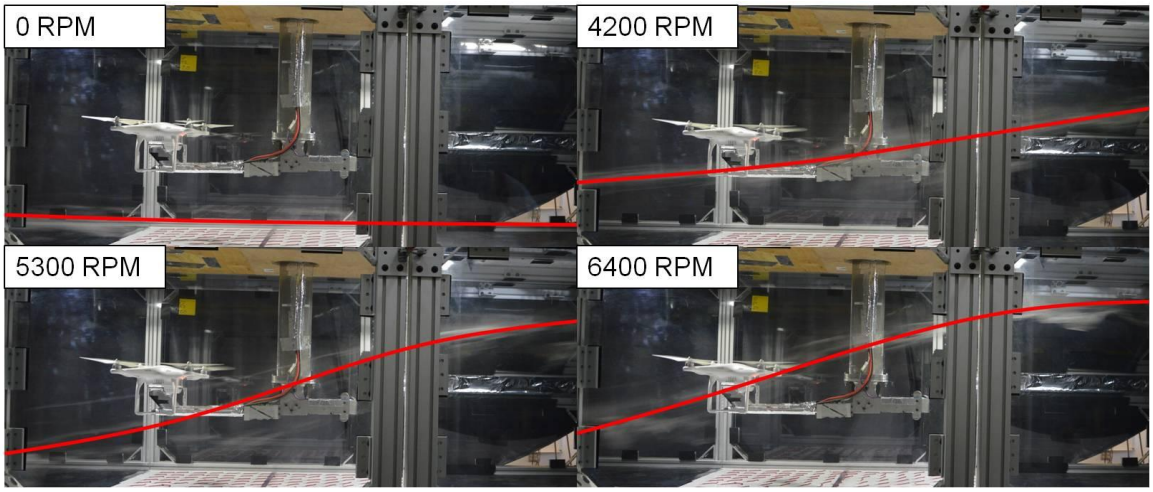

Figure 42. Effect of Motor Speed on Wall Streamline Deflection at 0° Vehicle Pitch Angle.

The effect of vehicle pitch angle on smoke slipstream deflection is shown in Figure 43 for a nominal airspeed of 20 ft/s and a collective motor speed of 6400 RPM. As seen in the tuft tests, pitching the vehicle down offsets the wake skew angle, resulting in a reduction in the deflection of the smoke streamlines.

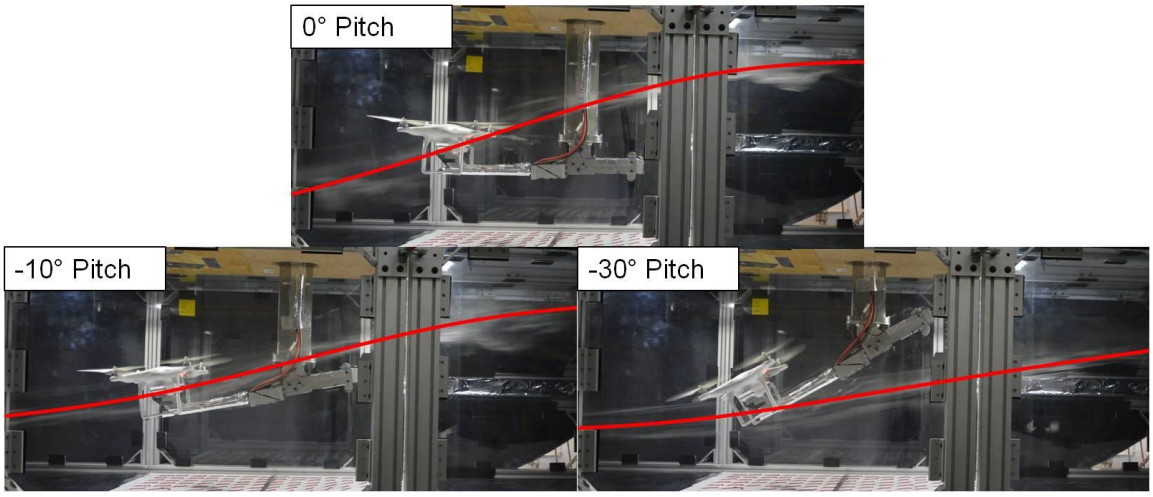

Figure 43. Effect of Vehicle Pitch Angle on Wall Streamline Deflection at 6400 RPM.

Finally, the effect of tunnel speed on wall streamline deflection is shown in Figure 44 for nominal 20 ft/s (q = 0.48 lb/ft^2) and 40 ft/s (q = 1.90 lbf/ft^2) cases. As seen in the tuft tests, increasing the momentum of the tunnel flow relative to the rotor wake decreases the magnitude of smoke deflection.

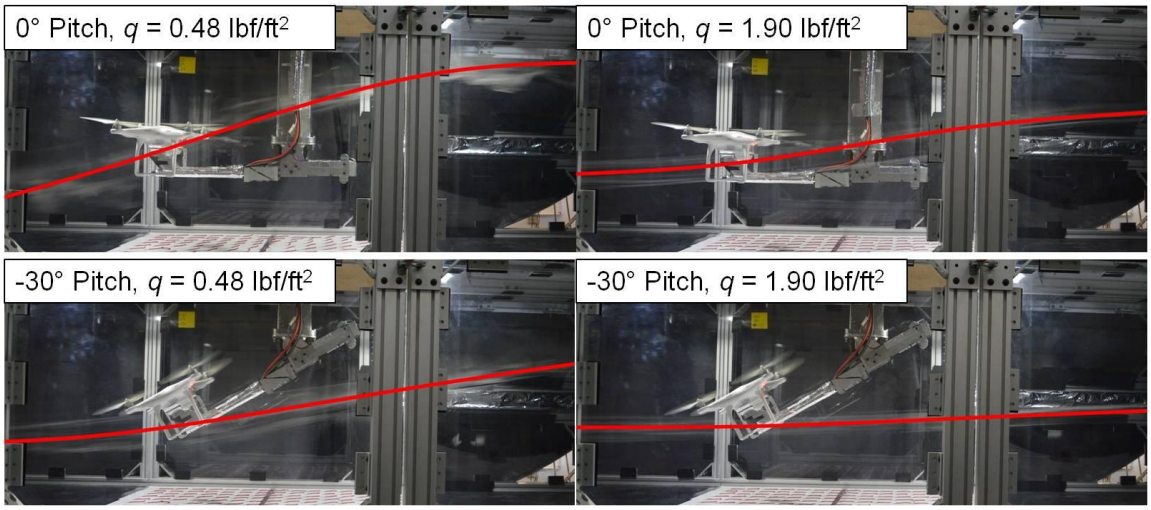

Figure 44. Effect of Tunnel Speed on Wall Streamline Deflection at 6400 RPM.

5.6.3 Rotor Inflow Visualization

Finally, an attempt was made to visualize the rotor inflow by using a line laser to illuminate a vertical cross section of smoke streamline ingested by the rotors. Unfortunately, the test equipment was not capable of producing adequate smoke or illumination to reliably photograph the airflow through the rotors. However, illuminating a cross section of flow aligned with the centerline of the vehicle revealed the highly unsteady, vortex-producing nature of the mutual wake interaction region between the rotors, as seen in Figure 45.

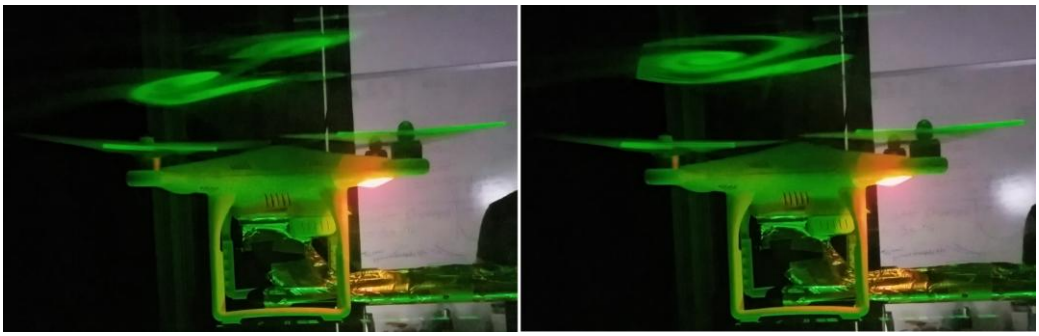

Figure 45. Laser Illuminated Smoke Vortices Generated by Rotor Interactions at the Vehicle Centerline.

6. UNCERTAINTY ANALYSIS

6.1 Motor Speed

Motor speed data was logged to verify that the closed-loop motor controller was working as expected. The standard deviation (σ) in motor speed across a single 30-second test run varied drastically across test points, but typically remained between 5-20 RPM. A small number of tests saw greater divergence, with a max recorded σ of 57.5 RPM. These outliers were characterized in the raw test data by a discontinuity followed by a surge in RPM, likely indicating that the FFT analyzer momentarily lost a lock on the BEMF signal. A typical time series of motor RPM measurements is shown in Figure 46 for both a front-mounted and rear-mounted rotor. Rotor speed was seen to regularly alternate between max divergence values of roughly equal magnitude across the test period; this was likely due to the minimum step-size in PWM duty cycle the controller board was capable of generating.

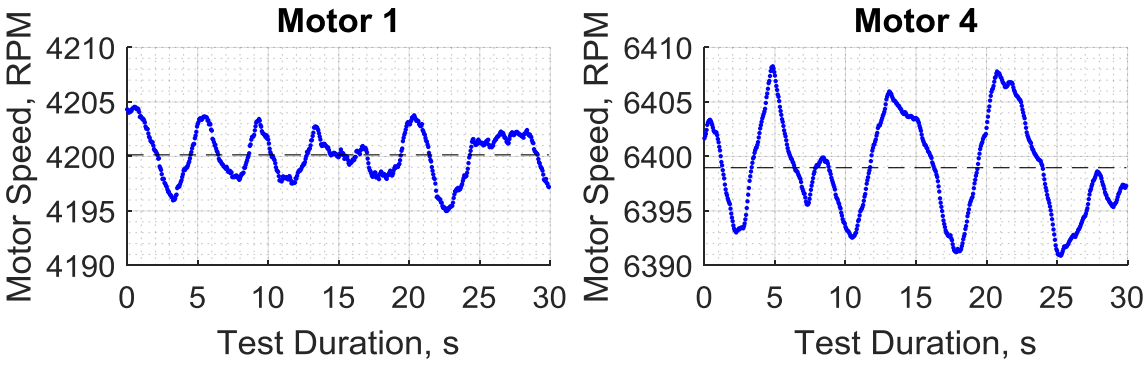

Figure 46. Measured RPM across Test Run (Pitch Angle = 0°, Front/Rear Commanded RPM = 4200 / 6400).

6.2 Power Usage

An example of the variance in total power usage across a test run is shown in Figure 47. The typical standard deviation in individual motor power of a time-averaged test point was 0.2-0.4W, with a greatest σ value across the set of test data of 0.991W. Power usage measurement uncertainty was highly sensitive to instrument tolerance as calculating the power at each ESC required three resistors – or a dozen resistors in total to measure the overall vehicle power usage. The resistor tolerances were propagated to determine the power measurement uncertainty, as shown in Figure 48. Note that DAQ sensing resolution was several magnitudes lower than resistor tolerance and was ignored. The black bars represent the measurement

uncertainty calculated using the manufacturer rated 0.1% tolerance of the voltage divider resistors. The color bars represent the measurement uncertainty calculated using the refined tolerance determined by multimeter testing. Clearly, the tolerance of the voltage divider resistors is a primary driver of power measurement certainty.

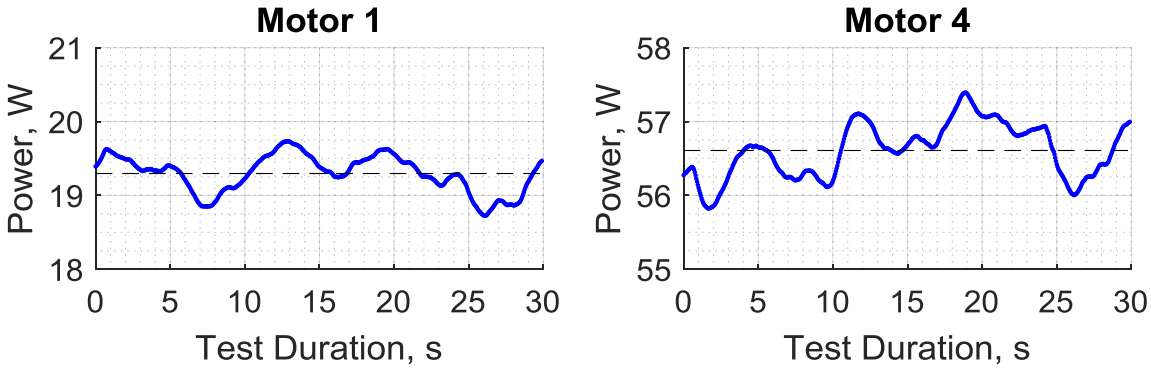

Figure 47. Measured Power Consumption across Test Run (Pitch Angle = 0°, Front/Rear Commanded RPM = 4200 / 6400).

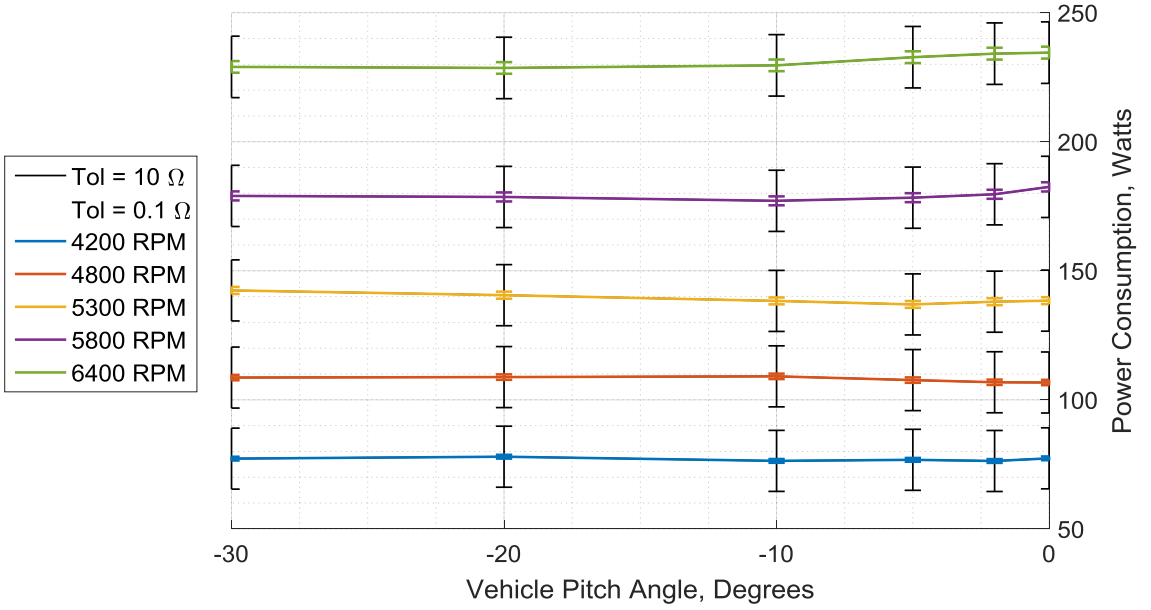

Figure 48. Total Vehicle Input Power Measurement Uncertainty – Collective RPM Tests (Configuration A).

Due to a lack of homogenous test points, the effect of repeatability on power measurement uncertainty was neglected. Overall uncertainty is likely subject to significant unmodeled errors, such as the effect of varying temperature or connector seating resistance. The larger uncertainty bounds are at the same magnitude as the

comparative motor power results, indicating the uncertainty should be refined prior to future similar tests. Future tests should perform more repeatability test points, which will better characterize the system and provide some reconciliation between the current two extremes of measurement uncertainty. If a future test setup retains voltage dividers, accommodation should be made to easily measure the resistances prior to beginning a test suite. Eliminating the need for voltage dividers by either switching to a low-side implementation or using more specialized current sense hardware will greatly reduce the measurement uncertainty and unmodeled error. Additionally, measuring the total power separately, rather than computing it as a sum of individual ESC power, would reduce the total power measurement uncertainty due to propagated instrument tolerance by a factor of four, as well as provide a useful point of comparison for the individual ESC power measurements.

6.3 Forces and Torques

The load cell's non-characterizable drift behavior was the largest source of force and torque measurement uncertainty. No consistent method was determined for correcting or predicting the linear but highly variable drift behavior. As such, the utility of aerodynamic loads measured during this project towards characterizing multirotor flight performance was much diminished. An example of significant drift behavior across a test run is shown in Figure 49.

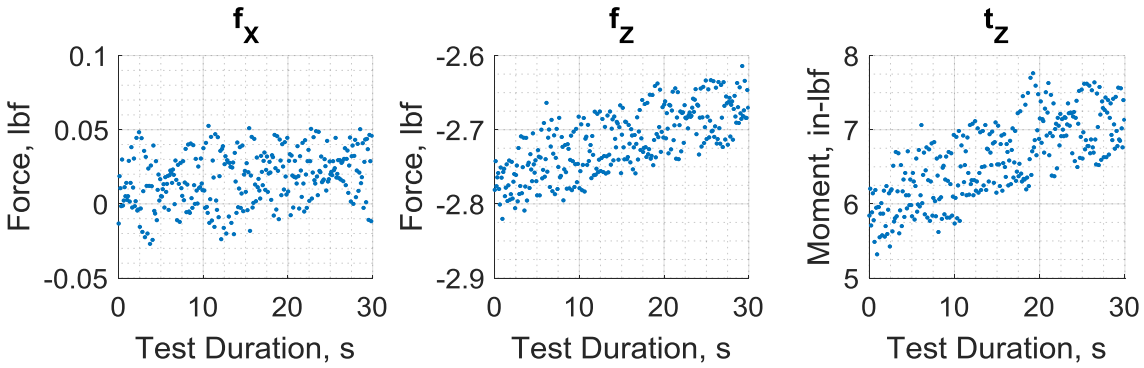

Figure 49. Measured Aerodynamic Loads across Test Run (Pitch Angle = 0°, Front/Rear Commanded RPM = 4200 / 6400).

The force measurement uncertainty arising from only the load cell measurement resolution is shown in Figure 50. Note that this is not representative of the combined uncertainty which, due to the drift behavior,

is much larger. However, note that the error bars encompass nearly all of the data points taken in either motor layout configuration test.

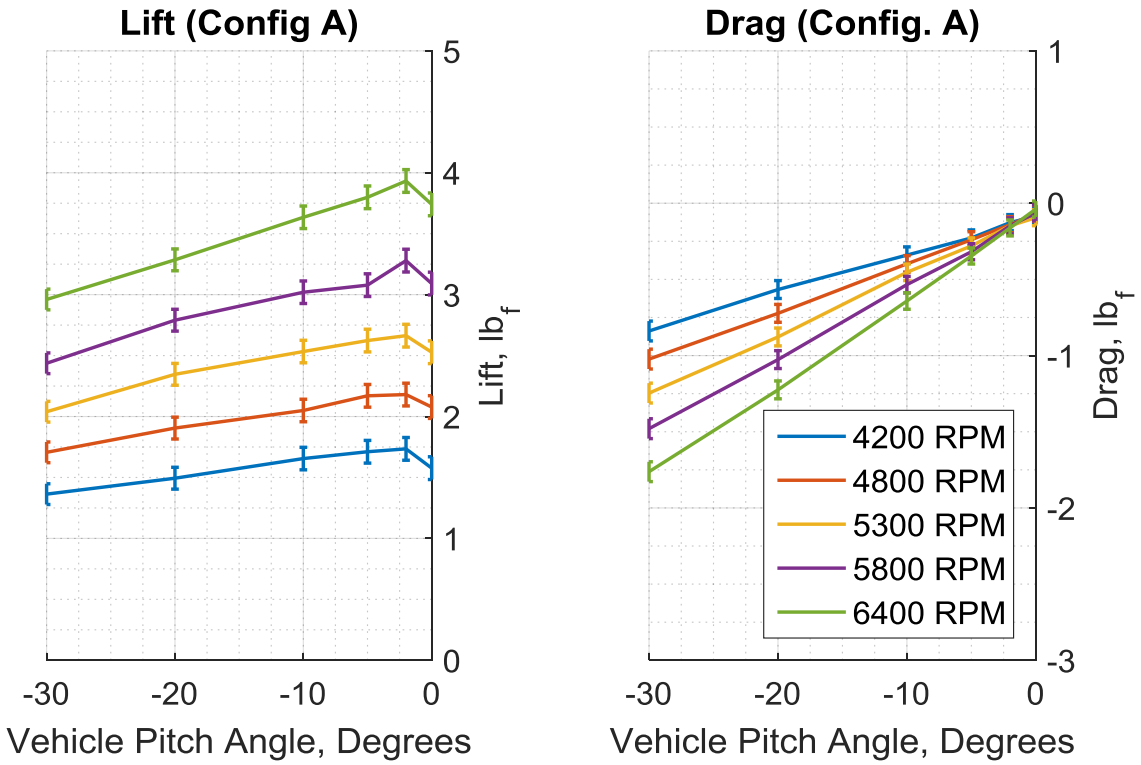

Figure 50. Force Measurement Uncertainty due Solely to Load Cell Resolution Collective RPM Tests (Configuration A).

7. CONCLUSIONS

7.1 Quadcopter Performance

The test setup was able to measure and record force and torque data as well as individual motor power and speed for all test conditions. A side-by-side comparison with data from similar tests performed in a NASA Ames tunnel demonstrated that the two sets of test data exhibited similar trends but at significantly different magnitudes. Similar discrepancies between the data sets for both aerodynamic and power measurements may be due to a disparity between measured and actual RPM in one or both of the sets of test data. Additional discrepancies arise from instrument measurement uncertainty and the non-characterizable drift behavior of the load cell used for these tests. Results such as negative drag measurements at 0° vehicle pitch angle highlight the load cell as a primary source of error.

Total vehicle power usage for the Collective RPM tests was seen to be overwhelmingly driven by motor RPM with a much weaker inverse trend with increasing vehicle downwards pitch. Determining the impact of motor mounting position on motor power consumption was complicated by Motor 1 and Motor 2 drawing significantly more power when mounted in the front positions, a trend which was not seen with Motor 3 and Motor 4. Vehicle pitch angle was seen to affect whether the front or rear motors drew a larger fraction of the overall input power for a given RPM setting. At small vehicle pitch angles, rear mounted motors drew more power than the front mounted rotors. This trend was reversed as downward pitch increased. These trends were also seen in the Cyclic RPM tests.

Determination of the vehicle's forward flight performance was hampered by the lack of a region within the test space which satisfied all three zero net lift, drag, and pitching moment requirements. The point at which the zero net lift and zero net drag contours converged was used to estimate the vehicle's equivalent lift-to-drag ratio at a forward speed of 20 ft/s. Calculating $L/D|_{Eq}$ from the NASA Ames test data provided a value of 0.63. Calculating $L/D|_{Eq}$ with the Collective RPM test data set provided a similar value of 0.59. The Cyclic RPM tests did not demonstrate a force contour intersection from which an equivalent lift-to-drag ratio estimate could be calculated. While these lift-to-drag numbers ostensibly suggest at the multirotor configuration's relatively poor aerodynamic performance, several considerations must be made.

First, the equivalent lift-to-drag ratio metric suffers a penalty relative to the conventional lift-to-drag ratio due to the incorporation of propulsive system inefficiencies of the ESC, motor, and propeller. Secondly, there is a lack of published data on small scale rotorcraft with which to make an appropriate comparison.

7.2 Performing Powered Testing of Multirotor Vehicles in Limited Cross-Sectional Area Wind Tunnels

The tests performed in the Cal Poly Low Speed Wind Tunnel did not show close agreement with the results from the NASA Ames tests. With a total rotor area of 1.95 ft^2, the ratio of rotor area to the cross-sectional area of the 7-by 10-ft tunnel was 0.028. The ratio of rotor area to the cross-sectional area of the 3-by 4-ft Low Speed Wind Tunnel was 0.163, representing a 5.82-fold increase. With such a significant decrease in tunnel size, a drastic change in performance measurements due to tunnel interference effects should be expected. The contribution of tunnel effects to the differences between the Cal Poly and NASA Ames test results cannot be quantified due to the measurement uncertainties in the data collected in the 3-by 4-ft wind tunnel. Similar trends in force and power measurements were seen between the tests, and flow visualization indicated that the strength of tunnel interference can vary drastically across the test space of a powered multirotor test rig. The lessons learned summarized below will assist in the test plan development and test rig design of future multirotor wind tunnel test programs.

7.2.1 Minimum Instrumentation Requirements

Power Sensing

The use of a current sense resistor (CSR) is an effective method for tracking the power usage of an ESC-motor pair. Input current is calculated via the difference in voltage across the resistor, and if the resistor is placed on the high side of the load then the low-voltage CSR signal lead can also provide the input voltage. A high tolerance component is essential as the low resistance of a CSR makes independent verification of resistance generally impractical. The voltage difference is directly proportional to the resistance of the CSR, so selecting a high resistance will generally reduce any error associated with the minimum resolution of the analog-to-digital converter. The upper limit on resistance is limited by the CSR's max power and operating temperature specifications. A 4-terminal design provides a convenient second set of terminals for attaching sensor leads.

The current sense resistor is placed in series with the ESC DC leads, preferably near the ESC board. The resistor can be placed on either the high-side or the low-side of the ESC. The primary benefit of low-side sensing is that the voltages are near ground and potentially could be connected directly to the DAQ device with no additional circuitry. Because a low-side implementation places a resistor between the primary load and the ground, it introduces a risk of causing ground loops within the system. Additionally, a third sensor lead would be needed to track the ESC input voltage. This project relied on high-side sensing. The primary drawback of high-side sensing is the need to reduce the bus voltage down to the input voltage range of the DAQ. This project handled the bus voltage step-down through the use of voltage dividers near the DAQ to split the voltage. While ostensibly effective, the use of a resistor network of voltage dividers is sub-optimal from a system level perspective. The first challenge is that resistor selection must balance contradictory design requirements - a high resistance is desirable for minimizing leakage current, but imposes high impedance on the signal terminations at the DAQ device. Since high impedance on the signal terminations can cause signal ghosting between channels, the DAQ sample rate must be lowered accordingly. Secondly, because the voltage difference across the CSR is relatively small (particularly at low current) a lab-grade ohmmeter may be required to determine the voltage divider ratio and ensure accurate power measurements. If high-side sensing remains preferable for future experiments, than some alternate methods of handling the bus voltage step-down should be investigated. For example, the use of a differential op-amp would allow both CSR voltage measurements to be reduced to a single DAQ channel. Finally, current shunt monitors or other chip-level sensing methods should be considered if a higher degree of accuracy is required [23].

Motor Speed Sensing

Motor speed can be accurately measured via FFT tone detection of the back electromotive force signal on one of the motor leads. The method employed in this project was validated via measurements taken with a laser tachometer. However, as discussed in Section 5.1 the mismatch in test results compared to the Ames test data suggests that additional verification should be performed. Future validation of motor speed sensing should take place under more test-like conditions: tunnel on, vehicle pitched down, and multiple motors running at difference commanded speeds. Care should be taken that optical or laser tachometer measurements aren’t being affected by high-frequency light sources such as fluorescent bulbs. Notably, the FFT method was able to maintain consistent detection of the BEMF frequency with a DAQ sample rate at

4000 Hz and a motor speed of up to 6400 RPM (corresponding to a f_{BEMF} of 747 Hz), a sample-rate-to-signal frequency ratio of 5.4.

Force/Torque Sensor

Powered multirotor testing imposes strenuous capability requirements on the selection of an adequate load cell transducer for measuring force and torque. The sensor must be capable of measuring loads many times the weight of the test rig - yet sensitive enough to measure small differences caused by incremental changes to motor RPM or vehicle pitch. Additionally, powered testing produces a high vibration and electrically noisy environment. Tunnel flow and rotor wake can also cause rapid thermal fluctuations. Full characterization of load cell behavior to these phenomena should be considered a prerequisite to performing powered multirotor testing.

7.2.2 Avoiding Wind Tunnel Interference

The Z-Height test suite examined the effect of raising the test rig's rotor plane above the vertical centerline of the tunnel's test section, thereby increasing the distance between the rotors and the tunnel floor. Rotor plane height had a notable impact on force, torque, and power test data at a vehicle pitch angle of 0°. The effect of Z-height on test results was severely reduced when pitching the vehicle downwards to -10° then -20°. Additionally, tuft boards and smoke provided an effective means for visualizing rotor wake impingement and wake recirculation within the test section. The proximity of wake impingement to the test vehicle and the strength of wake recirculation along the test section walls were highly sensitive to tunnel speed, vehicle pitch angle, and motor speed. Thus, the impact of tunnel interference effects on multirotor test data can be inferred to vary greatly within the flight envelope of these vehicles.

7.2.3 Developing a Test Methodology

The primary challenge in developing a test plan for an electric multirotor vehicle is reducing the number of individual test cases to a manageable number. The forward flight performance space of a multirotor vehicle is comprised of flight path speed, vehicle pitch angle, and any combination of motor speeds; attempting to test across these parameters without careful design of experiment will result in an unfeasibly large test plan unless extensive tradeoffs are made in terms of parameter scope and fidelity. The number of test cases can be reduced by only performing tests around flight states of interest – for example, only testing

combinations of airspeed, vehicle pitch, and motor speeds that correspond to steady, level forward flight. The set of test parameters that correspond to the flight states of interest must be estimated prior to development of the test plan. This represents an opportunity to integrate other methods of analysis into a wind tunnel test program, such as the use of instrumented free-air test flights or CFD analysis to determine the trim state of the vehicle across different airspeeds.

BIBLIOGRAPHY

[1] R. C. Busan, W. J. Fredericks and M. D. Moore, "Benefits of Hybrid-Electric Propulsion to Achieve 4x Increase in Cruise Efficiency for a VTOL Aircraft," in *AIAA Aviation Technology, Integration, and Operations (ATIO) Conference*, Los Angeles, Aug 12-14, 2013.

[2] A. M. Stoll, B. JoeBen, M. D. Moore, W. J. Fredericks and N. K. Borer, "Drag Reduction Through Distributed Electric Propulsion," in *Aviation Technology, Integration, and Oeprations Converence*, Atlanta, GA, 16-20 June, 2014.

[3] Workhorse, "http://workhorse.com," 2018. [Online]. Available: http://workhorse.com/surefly. [Accessed January 2018].

[4] Volocopter, "Design Specifications for Volocopter 2X," April 2017. [Online]. Available: https://www.volocopter.com/en/. [Accessed February 2018].

[5] C. Russell, J. Jung, G. Willink and B. Glasner, "Wind Tunnel and Hover Performance Test Results for Multicopter UAS Vehicles," in *American Helicopter Society (AHS) International Annual Forum and Technology Display*, West Palm Beach, FL, May 16-19, 2016.

[6] W. Johnson, Helicopter Theory, Princeton, New Jersey: Dover, 1980.

[7] O. Rand and V. Khromov, "Compound Helicopter: Insight and Optimization," in *American Helicopter Society 69th Annual Forum*, Phoenix, Arizona, May 21-23, 2013.

[8] F. D. Harris, "Twin Rotor Hover Performance," *Journal of the American Helicopter Society*, vol. 44, no. 1, pp. 34-37, January 1999.

[9] M. S. Selig, "Modeling Propeller Aerodynamics and Slipstream Effects on Small UAVs in Realtime," in *AIAA Atmospheric Flight Mechanics 2010 Conference*, Toronto, Ontario, 2-5 Aug, 2010.

[10] J. B. Brandt and M. S. Selig, "Propeller Performance Data at Low Reynolds Numbers," in *45th AIAA Aerospace Sciences Meeting*, Orlando, FL, 4-7 January 2011.

[11] L. A. Young, "Conceptual Design Aspects of Three General Sub-Classes of Multi-Rotor Configurations: Distributed, Modular, and Heterogenous," in *Sixth AHS International Specialists Meeting on Unmanned Rotorcraft Systems*, Scottsdale, AZ, January 20-22, 2015.

[12] S. Yoon, H. C. Lee and T. H. Pulliam, "Computational Analysis of Multi-Rotor Flows," in *AIAA SciTech*, Reston, VA, 4-8 Jan, 2016.

[13] H. H. Heyson, "Wind-Tunnel Wall Effects at Extreme Force Coefficients," NASA Langley Research Center, Hampton, VA, 1968.

[14] W. H. Rae, "Limits on Minimum-Speed V/STOL Wind-Tunnel Tests," in *AIAA Aerodynamic Testing Conference*, Los Angeles, CA, September 21-23 1966.

[15] R. C. Busan, P. M. Rothhaar, M. A. Croom, P. C. Murphy, S. B. Grafton and A. W. O-Neal, "Enabling Advanced Wind-Tunnel Research Methods Using the NASA Langley 12-foot Low Speed Tunnel," in *14th AIAA Aviation Technology, Integration, and Operations Conference*, Atlanta, GA, 16-20 June 2014.

[16] M. Maisel, J. Giulianetti and C. Dugan, The History of the XV-15 Tilt Rotor Research Aircraft: From Concept to Flight, Washington, D.C.: NASA Office of Policy and Plans, NASA History Division, 2000.

[17] M. D. Maisel, D. J. Giulianetti and D. C. Dugan, "The History of The XV-t5 Tilt Rotor Research Aircraft: From Concept to Flight," NASA History Division, Washington, D.C., 200.

[18] G. J. Leishman, Principles of Helicopter Aerodynamics - Second Edition, Cambridge: Cambridge University Press, 2005.

[19] Cal Poly Aerospace Engineering, "Cal Poly Aerospace Low Speed Wind Tunnel," Cal Poly College of Engineering, 2016. [Online]. Available: https://aero.calpoly.edu/facilities/windtunnel/. [Accessed December 2017].

[20] DJI, "Phantom 3 Standard Specs," 2017. [Online]. Available: https://www.dji.com/phantom-3-standard/info.

[21] J. Zhao and Y. Yu, *Brushless DC Motor Fundamentals: Application Note*, Monolithic Power Systems, Inc, July 2011.

[22] C. Russell, G. Willink, C. Theodore, J. Jung and B. Glasner, "Wind Tunnel and Hover Performance Test Results for Multicopter UAS Vehicles," NASA/TM—2018–219758. Ames Research Center, Moffett Field, California, 2018.

[23] P. Seming and C. Wells, "EDN Network," Texas Instruments, 15 February 2012. [Online]. Available: https://www.edn.com/design/industrial-control/4236380/A-Current-Sensing-Tutorial-Part-II--Devices. [Accessed 30 March 2018].

[24] C. R. Green, "Modeling and Test of the Efficiency of Electronic Speed Controllers for Brushless DC Motors," M.S. Thesis, Dept. Aero.Eng., CSU, San Luis Obispo, California, 2015.

A. Additional Plots

A.1. Forces and Torques (Configuration A and B Powered Tests)

Side Force, FY

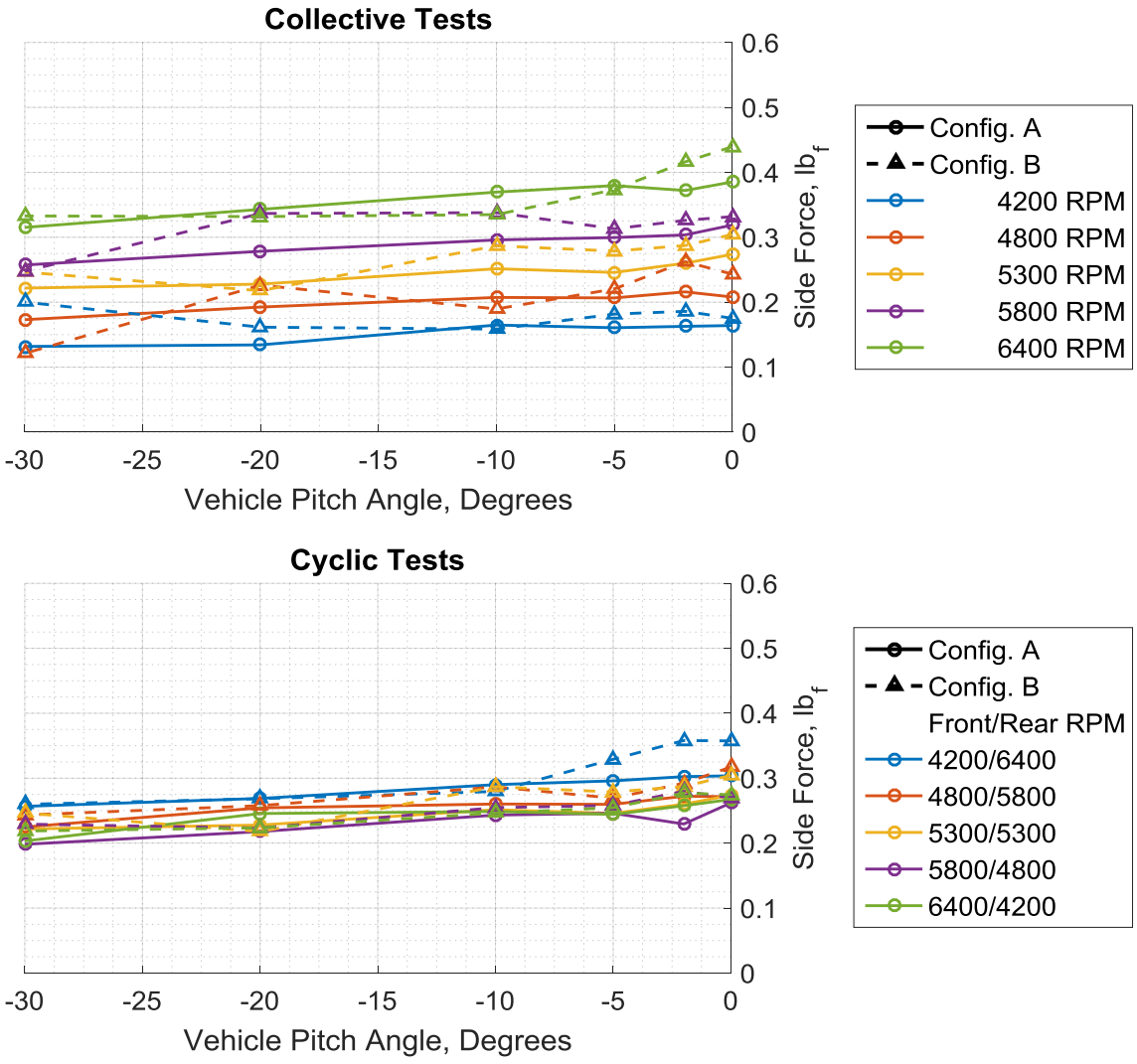

Rolling Moment, TX

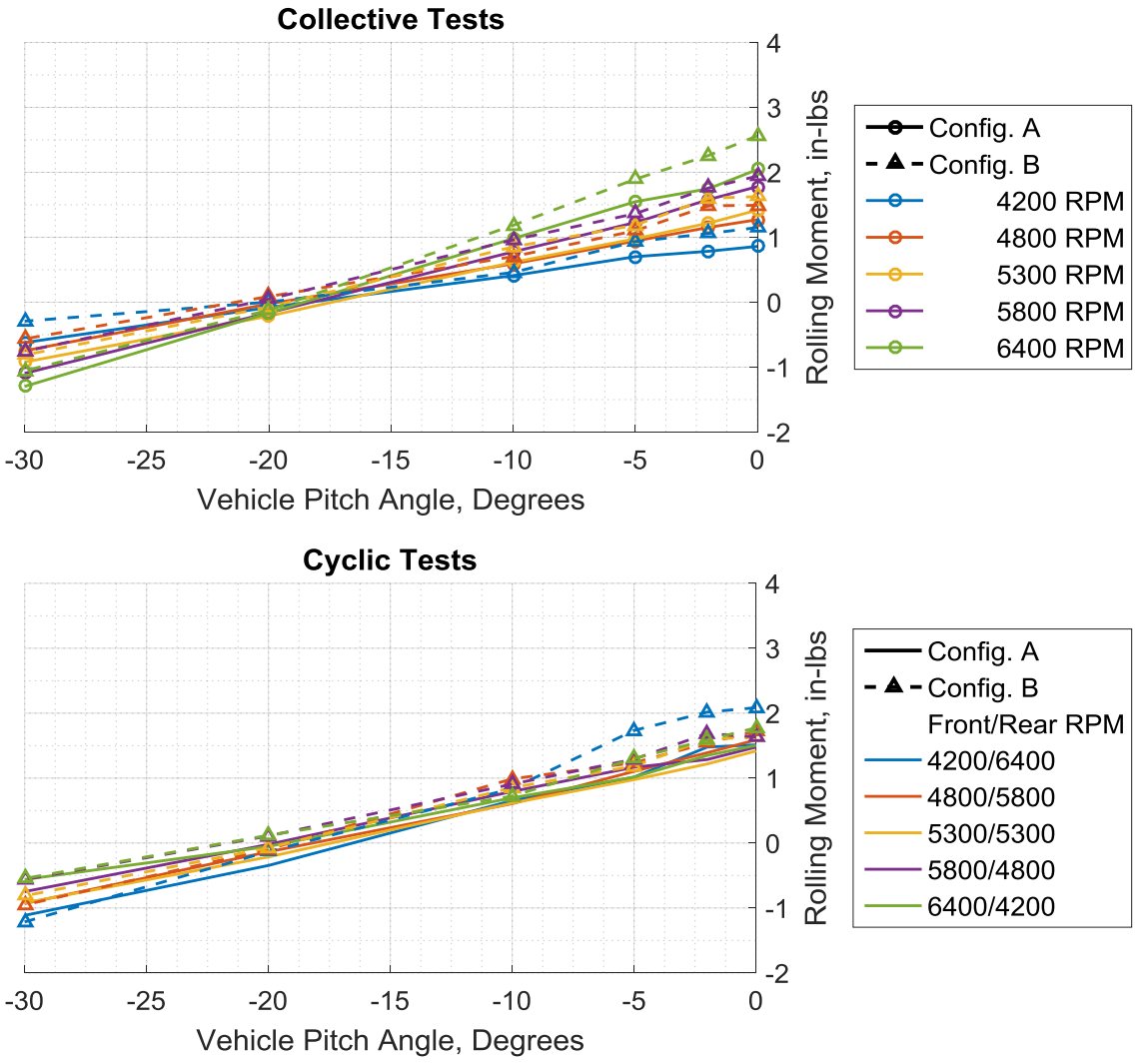

Yawing Moment, TZ

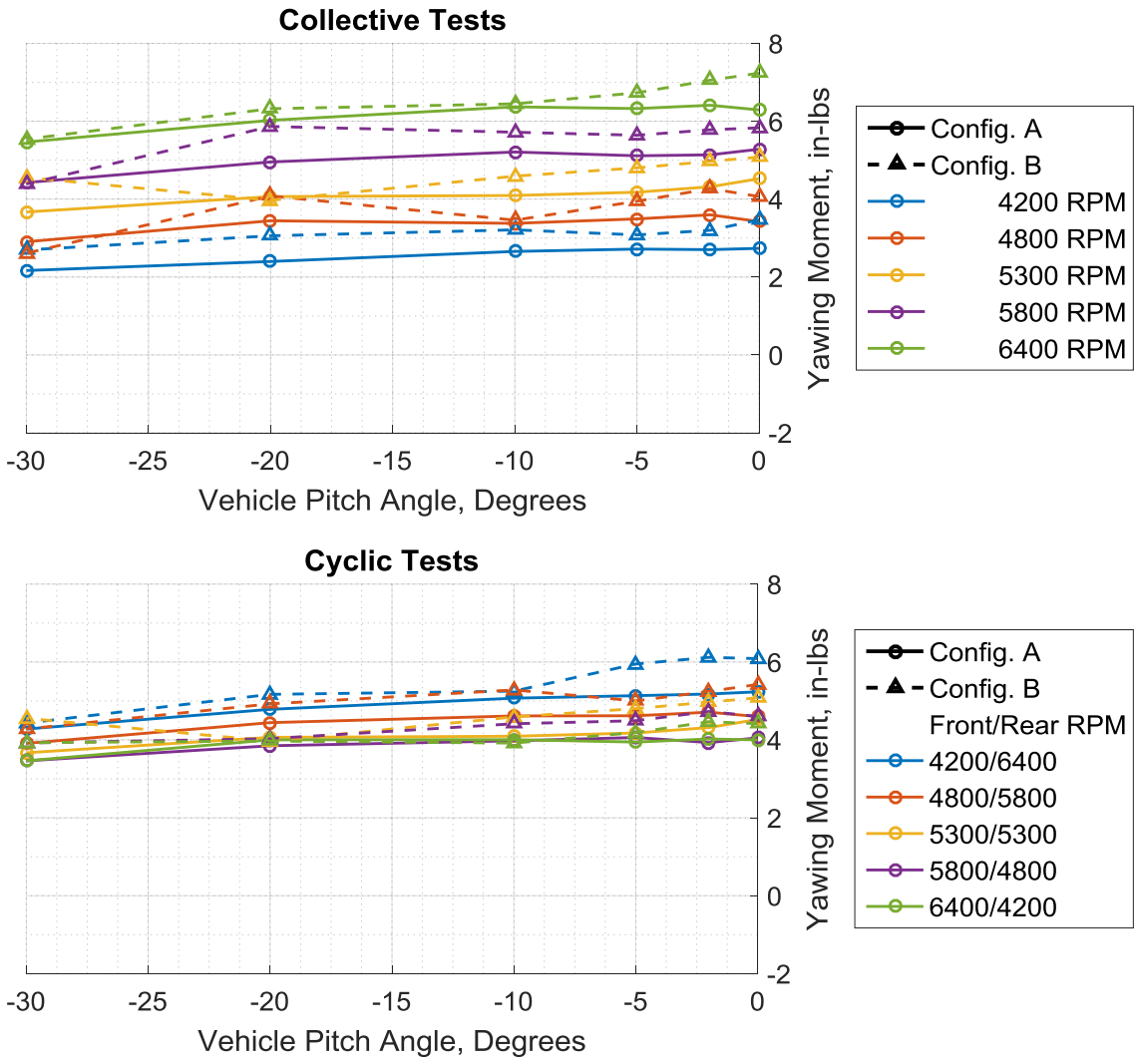

A.2. Power Usage (Configuration A and B Powered Tests)

Motor Power Usage, Collective RPM Tests

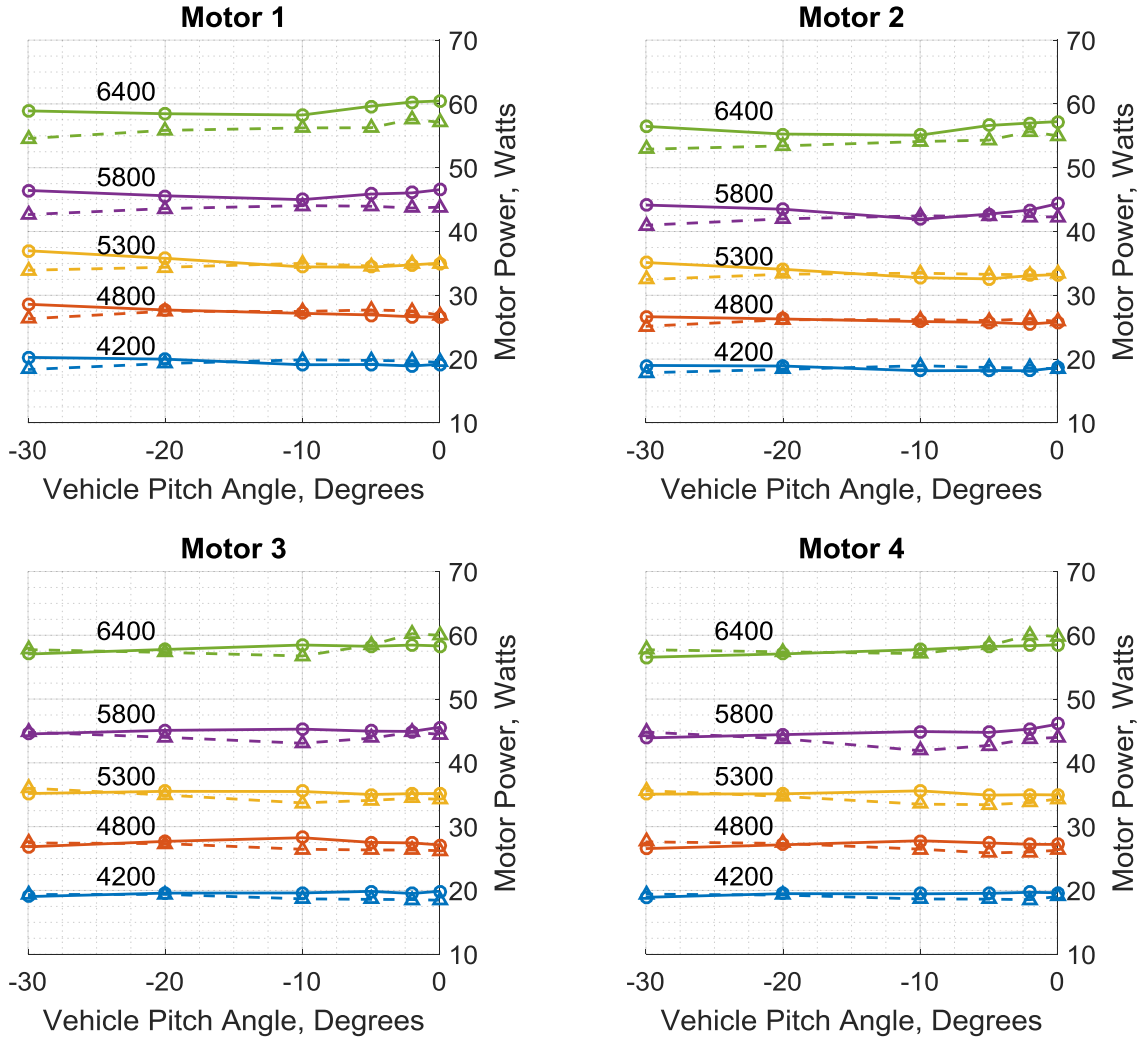

Motor Power Usage, Cyclic RPM Tests

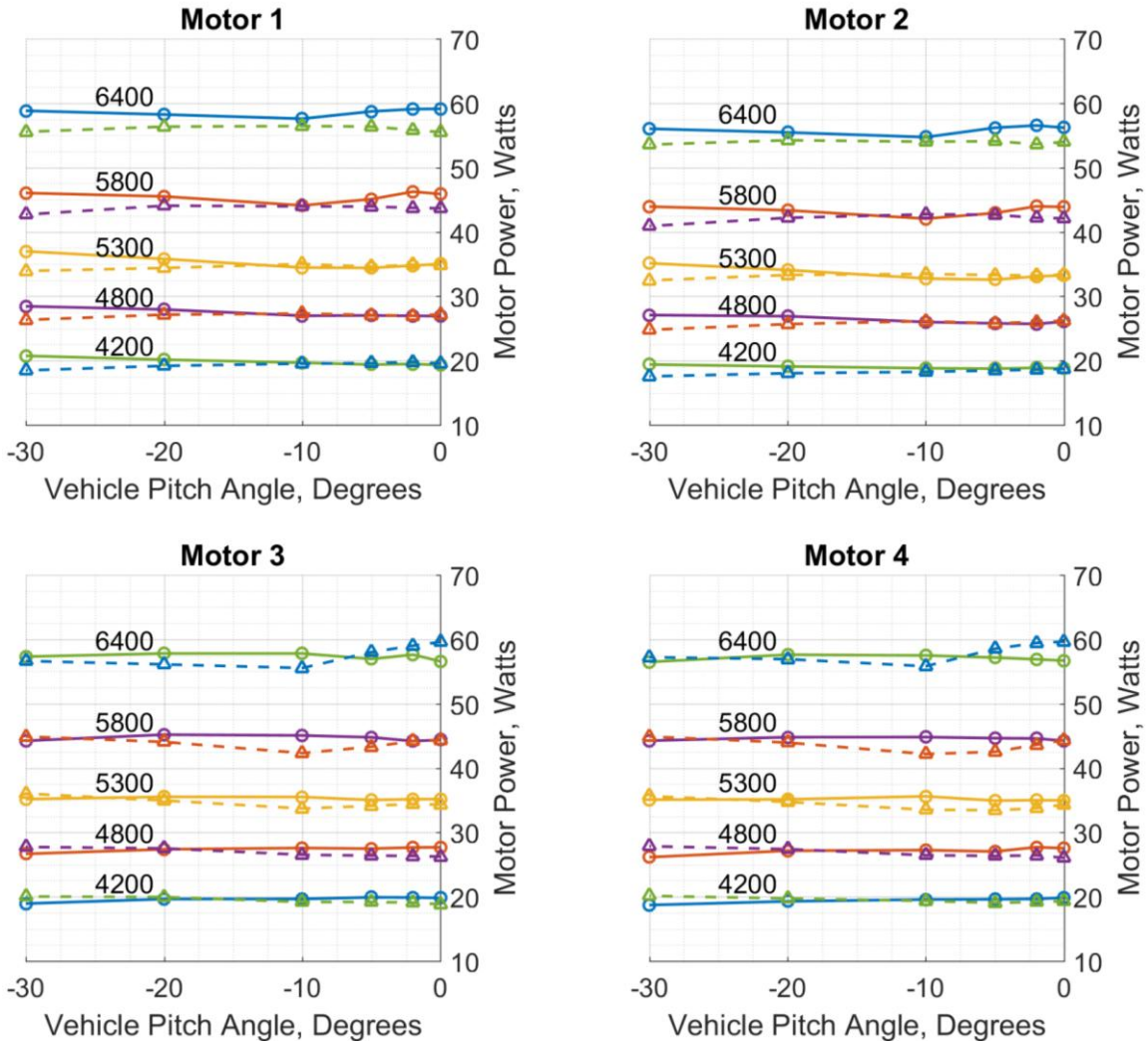

Δ Power (Configuration A – Configuration B), Collective Tests

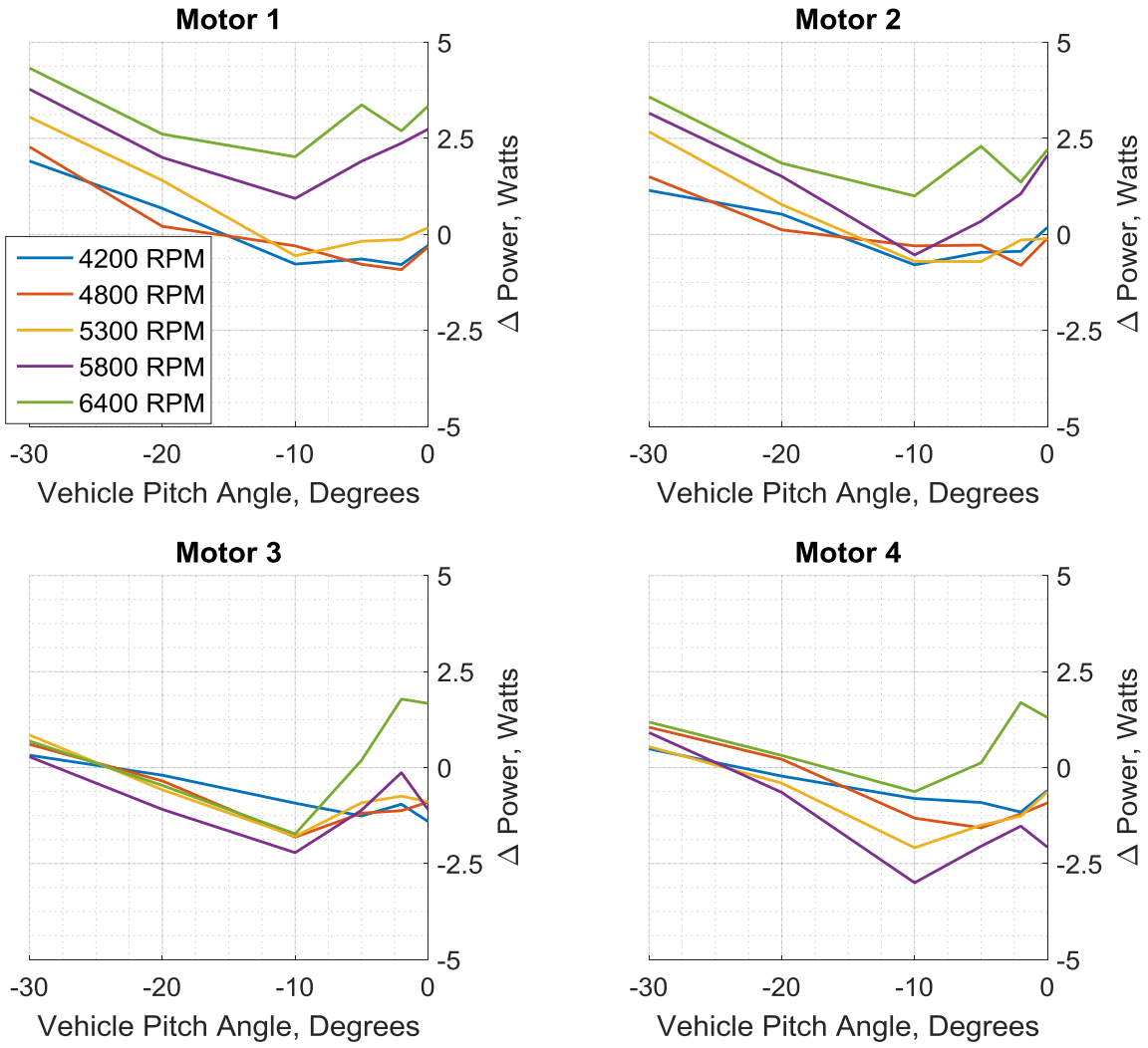

Δ Power (Configuration A – Configuration B), Cyclic Tests

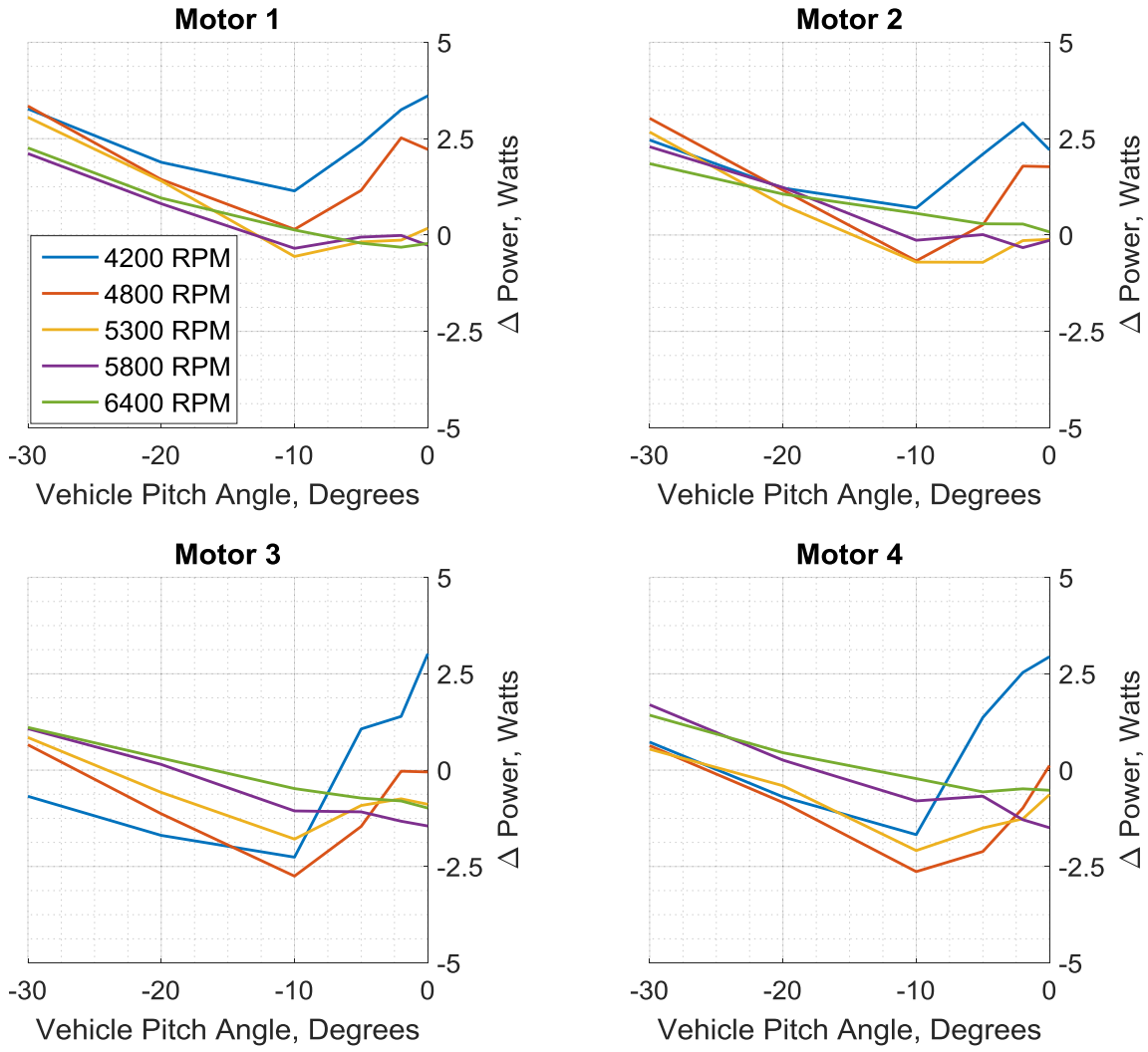

A.3. Z-Height Tests

Drag, F_X

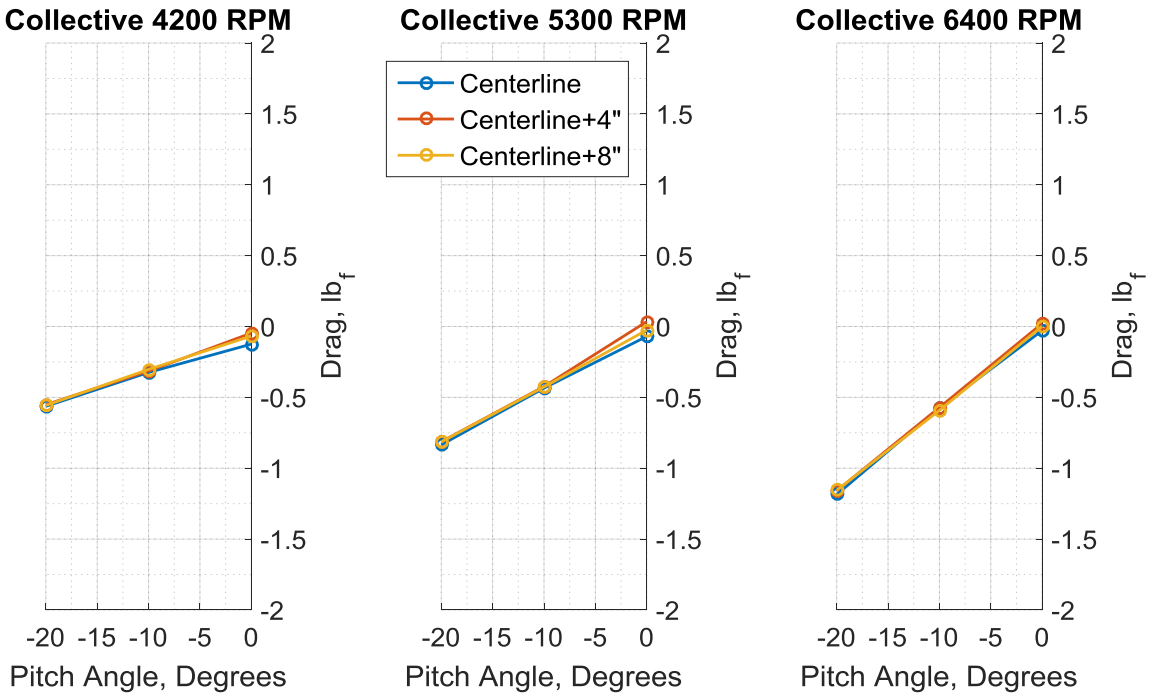

Side Force, F_Y

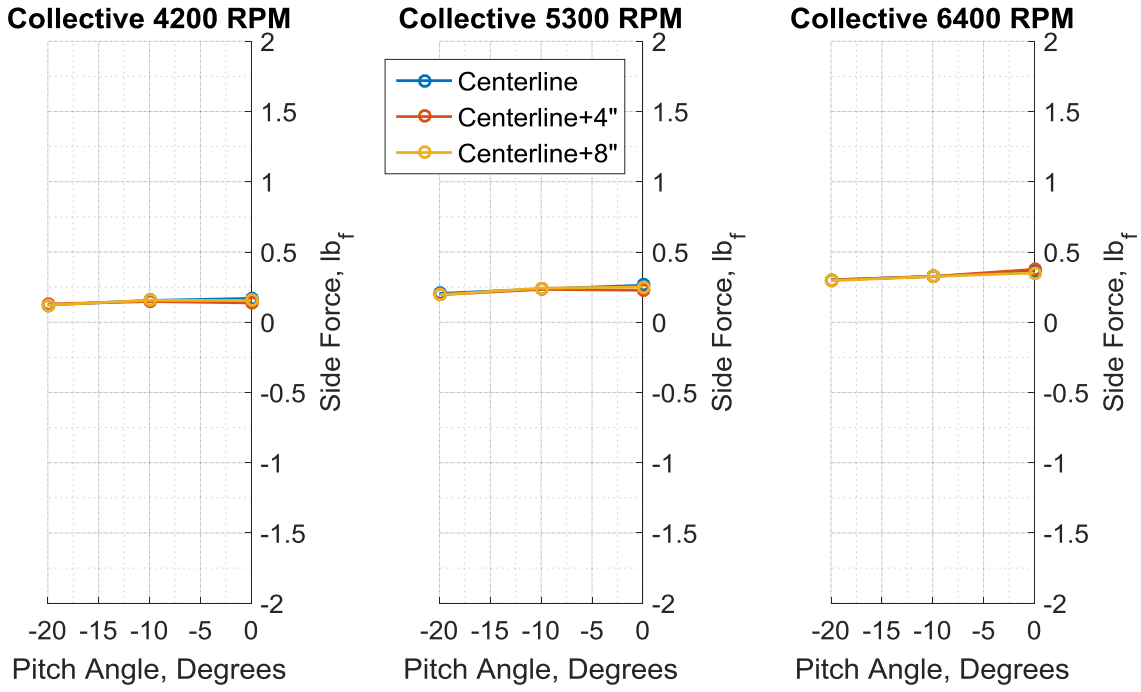

Rolling Moment, T_X

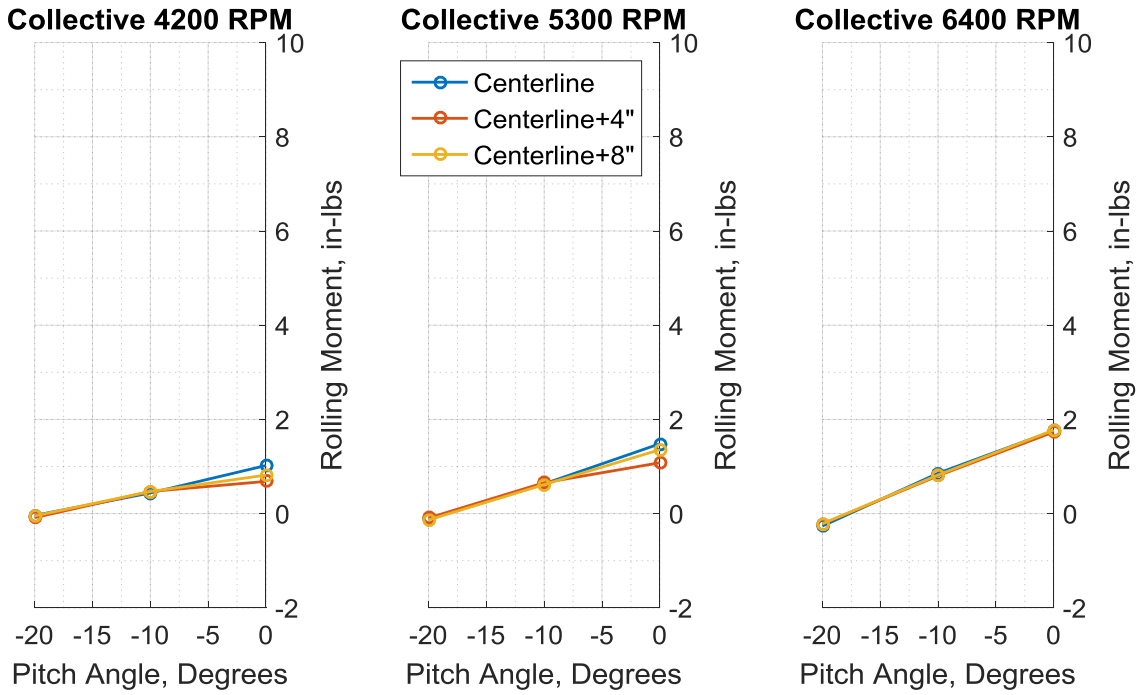

Yawing Moment, T_Z

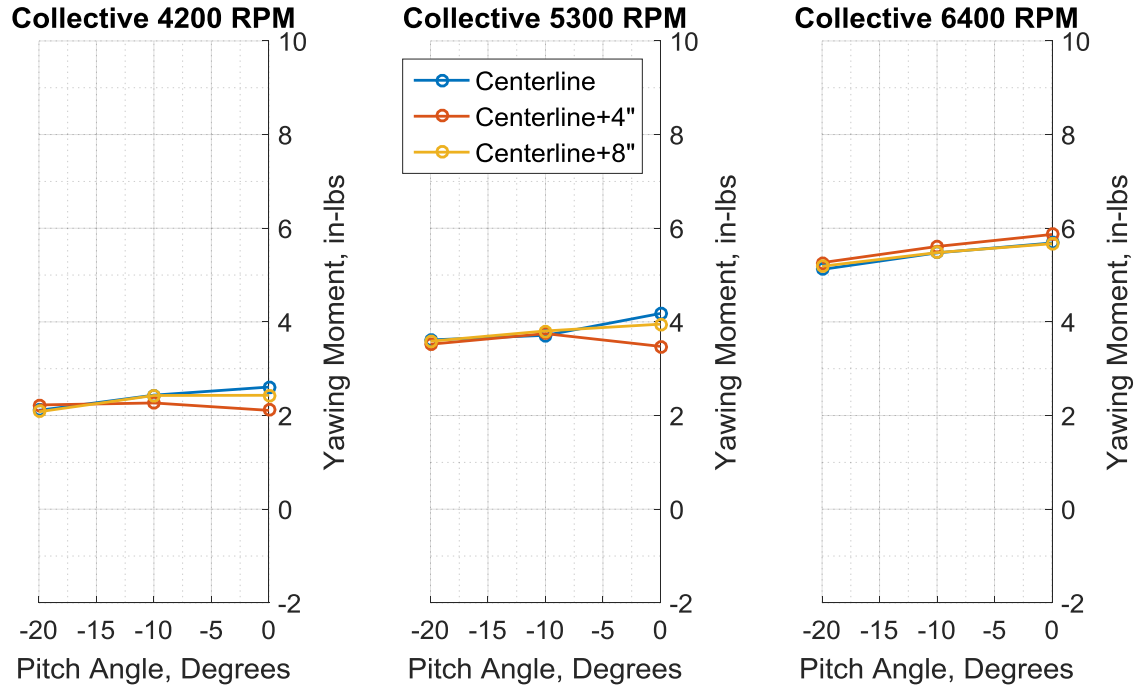

Motor 1 Power

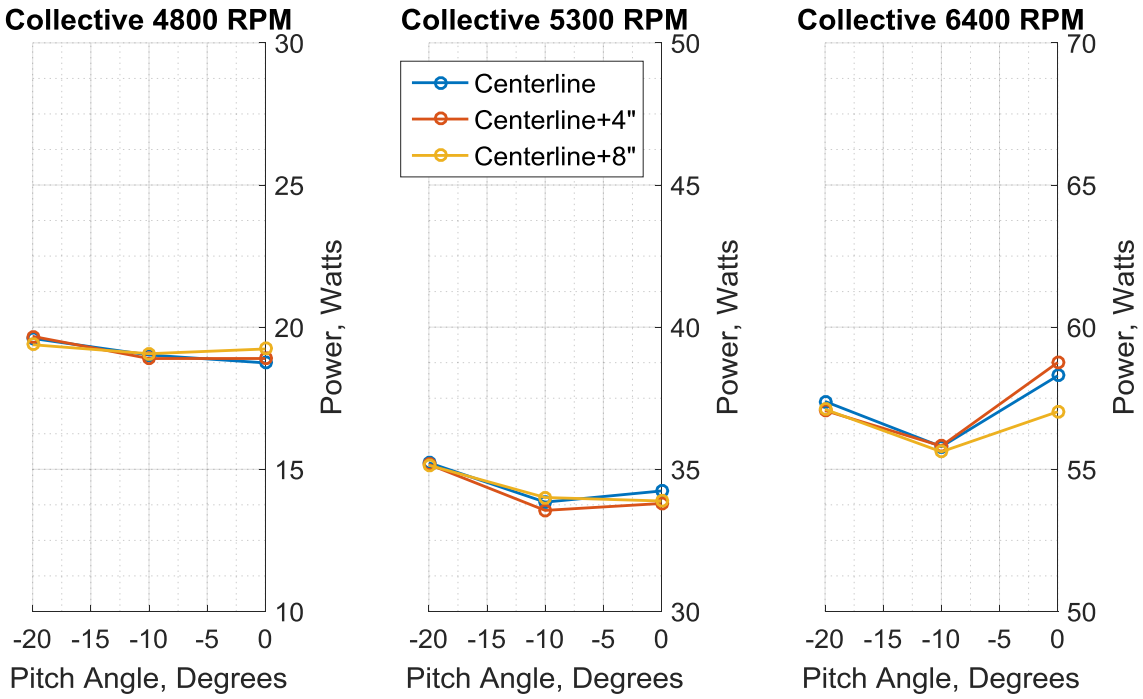

Motor 4 Power

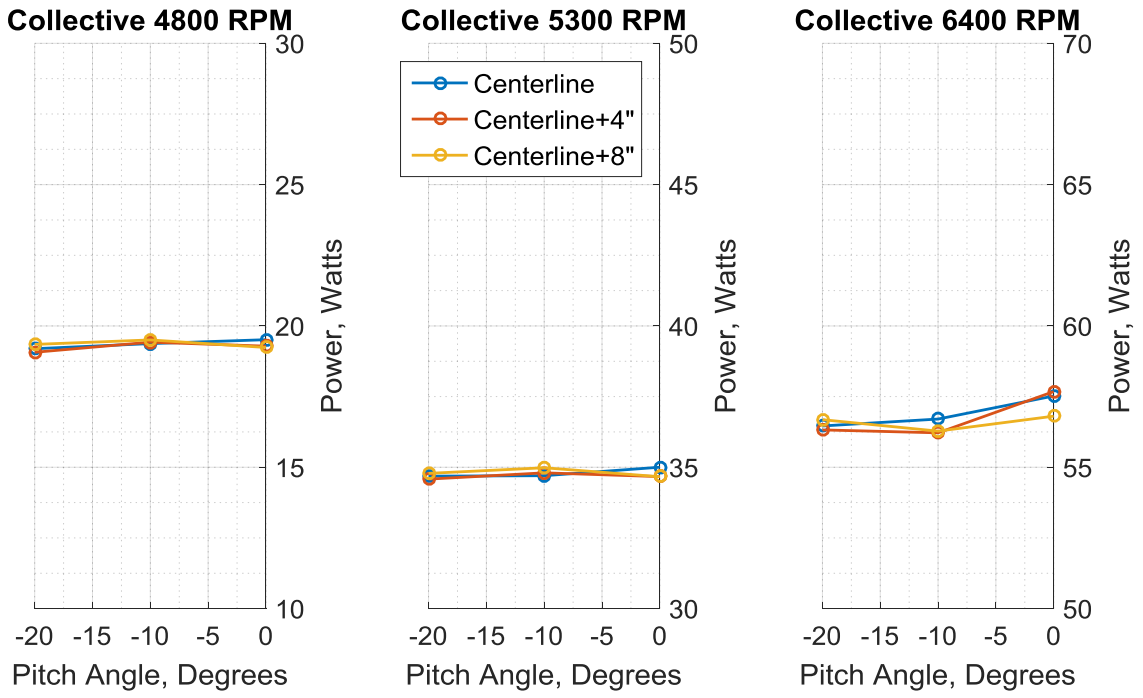

A.4. Additional Notes on Motor Speed Mismatch with Ames Tests

The plot below shows contours of lift and drag forces mapped against vehicle input power and pitch angle for both the Ames data set and the Configuration A, Collective RPM data set. The lift force contours between the data sets shows much better agreement than when they were plotted as RPM isolines. The drag contours also demonstrate greater similarity, although offset by the Ames data by about -0.5 lbs. This demonstrates possible evidence that the two tests may not have been performed at similar motor speeds, although more analysis would be needed to confirm this hypothesis. An alternative cause of this discrepancy could be a difference in rotor geometry between the two test rigs. However, both test rigs used OEM propellers that were visually identical.

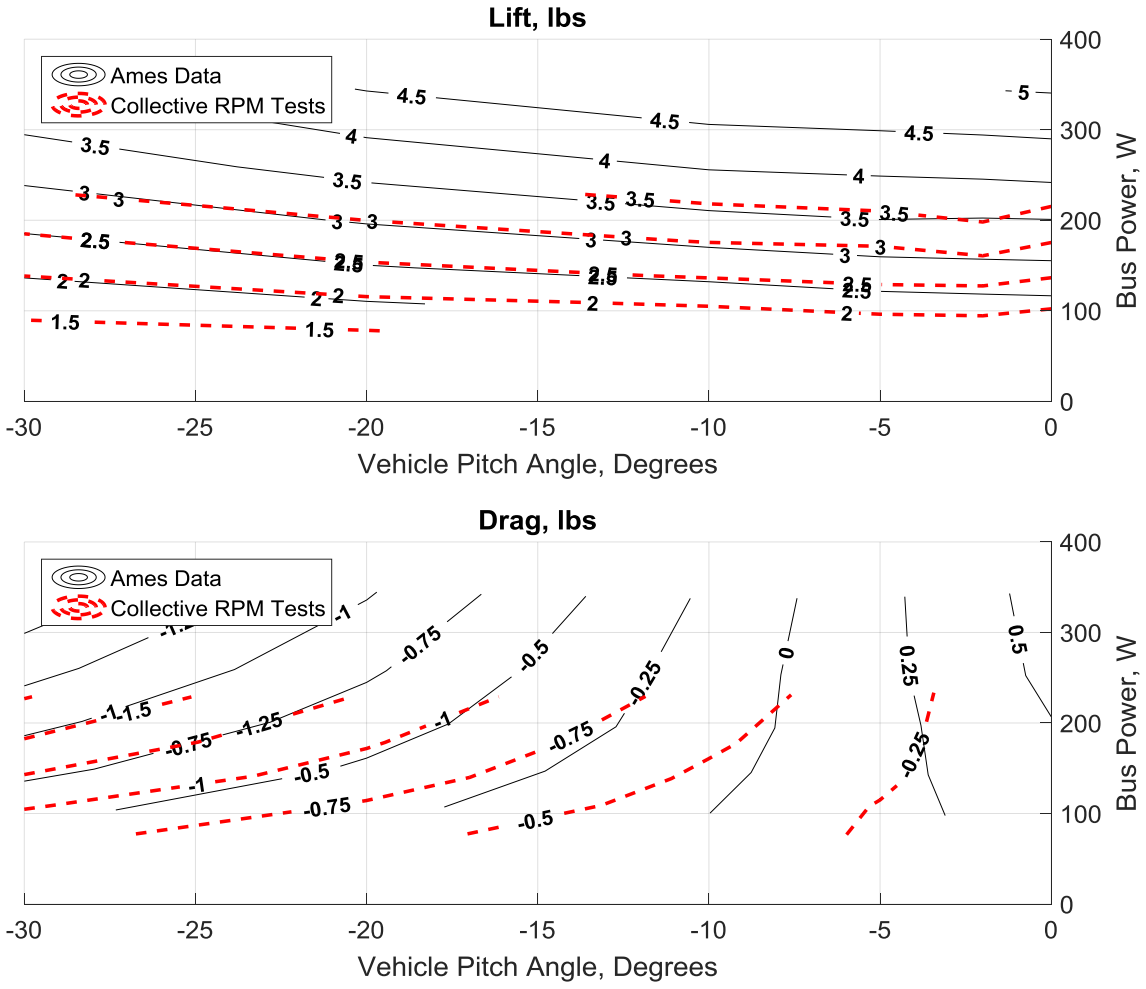

B. Load Cell Drift Behavior

Several examples of the load cell's drift behavior are shown below. Despite a significant amount of time spent attempting to characterize the drift behavior to tunnel or test conditions, no method of reliably predicting and accounting for drift was discovered. Drift was generally linear across all axes, but the magnitude and even direction changed unpredictably from test-to-test. F_Z and T_Y measurements demonstrated the most drift. Shown below is a typical example of tunnel-off static force and torque drift across 100 seconds. The inability for the load cell to maintain a tare is what prompted the decision to bias force and torque data for every powered test immediately beforehand.

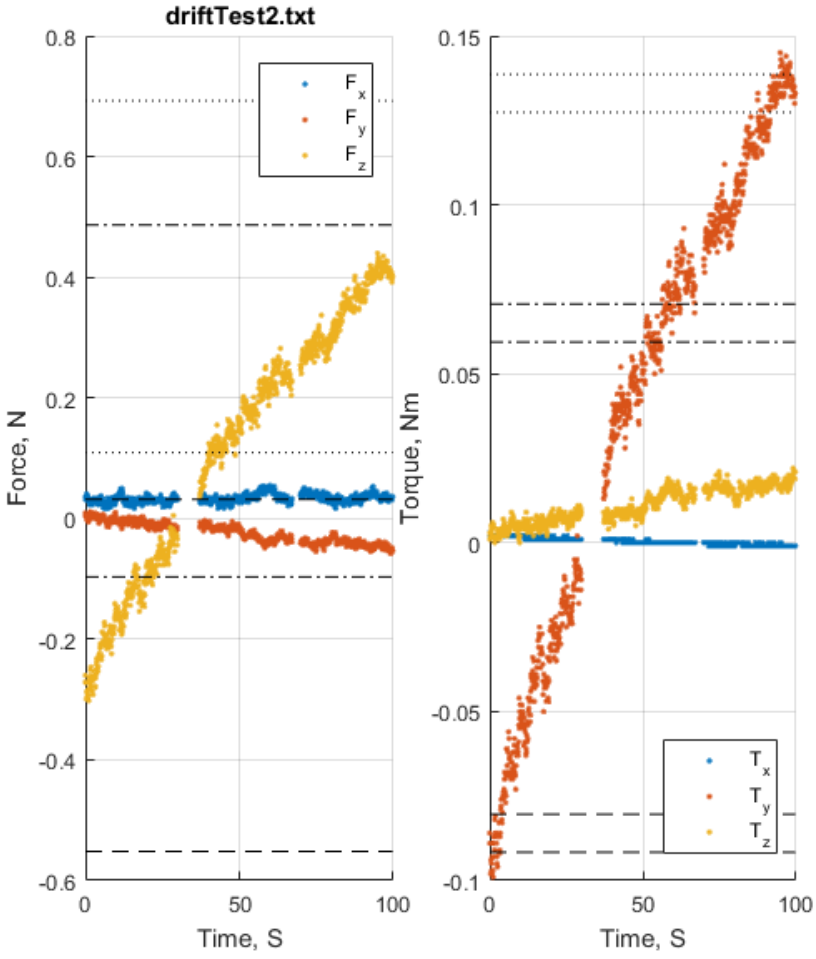

Data for a typical powered test point is plotted below. This test was taken with the vehicle pitch at -5° and all motors running at 6400 RPM. Unpowered test data is gathered both before and after the 30-second powered test run to determine a corrective offset for the powered tests. The linear drift behavior is easily visible across all three sets of data. The effect of mechanical vibration can also be seen in the scatter of data points during powered testing. The spread of dynamic pressure data and resulting tunnel airspeed is shown on the right – the spacing between values is caused by the minimum resolution of the Scanivalve sensor.

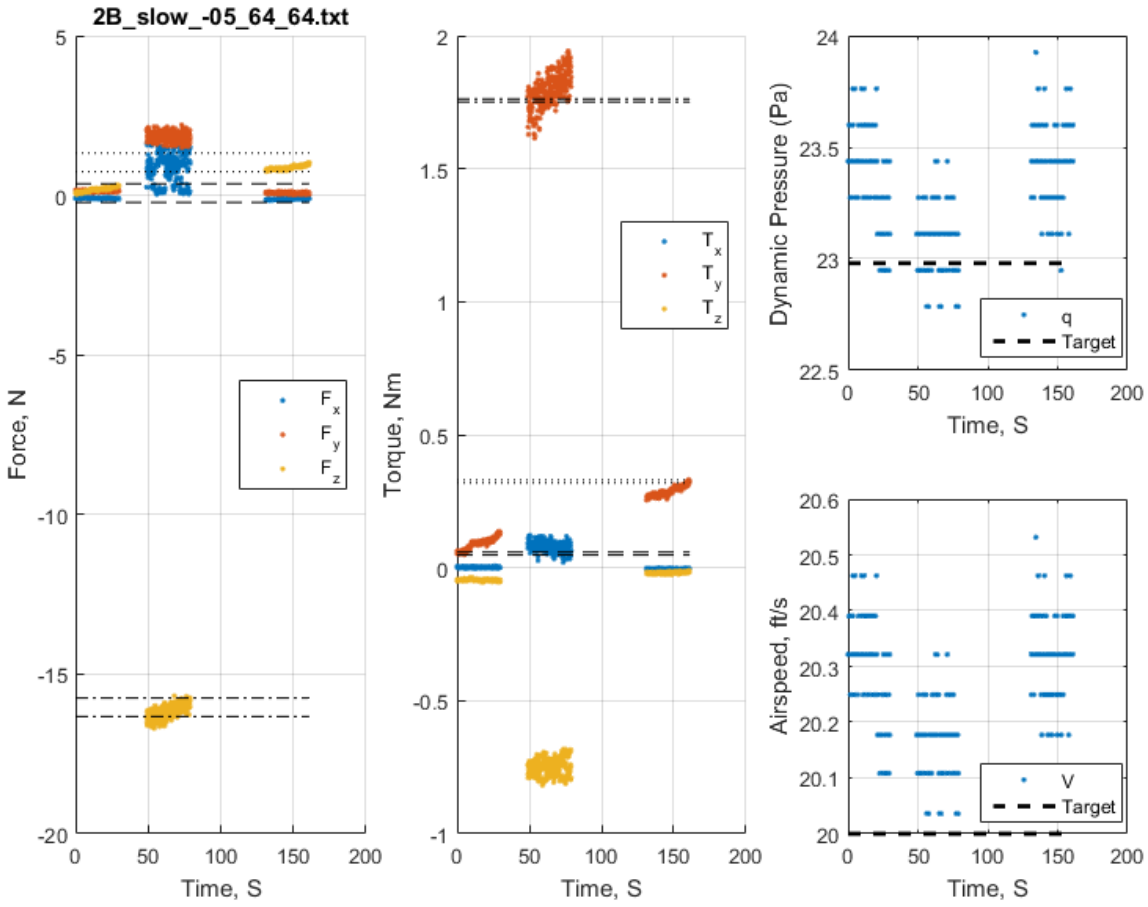

C. Test Procedures

C.1. Hardware Setup

#	(02) Hardware Setup Instructions
1	**Install force-balance mount**
2	Connect F/T transducer to sting harness hookup
3	Mount force-balance to sting mounting plate
4	Route force-balance cable through notch in mounting plate
5	**Mount quad test rig**
6	Slide test rig blade on to force-balance mounting pole
7	Adjust quad to horizontal by using an electronic level placed on the flat underside of the fuselage
8	Tighten bolt securing blade to force-balance
9	**Secure harness**
10	Adjust quad output cables so that connectors are flat along force-balance
11	Adjust embedded instrument circular cable so that connectors meet at pitch axle
12	Tape cables as flat as possible along force-balance and sting
13	**Assemble instrumentation external harness**
14	Refer to DAQ wiring diagrams to verify DAQ signal connections
15	Following items are plugged into power strip:
16	Power Supply
17	Force-Torque sensor DAQ
18	Force-Torque PS box
19	USB Hub
20	Following items are plugged into USB hub
21	Force-Torque Sensor DAQ USB cable
22	Quad sensor DAQ USB
23	Quad USB hookup cable
24	USB extension cable plugged into hub output
25	Following items are plugged into Force-Torque PS box
26	D-sub cable plugged into rear
27	12V power cable plugged into rear
28	Force-Torque sensor cable plugged into front
29	Following items are plugged into Quad Sensor DAQ
30	USB cable
31	Following items are plugged into Force-Torque Sensor DAQ
32	USB cable
33	Power cable
34	AC power extension cable plugged into power strip
35	AC power extension cable plugged into wall outlet

C.2. Pre-Test Procedures

#	(03) Pre-Test Procedure Instructions - Morning of Test
1	**Power on VFD**
2	**Disconnect motor power from quad prior to pre-test procedures**
3	**Verify external harness connections:**
4	Refer to DAQ wiring diagrams to verify DAQ signal connections
5	Following items are plugged into power strip:
6	Power Supply
7	Force-Torque sensor DAQ
8	Force-Torque PS box
9	USB hub
10	Following items are plugged into USB hub
11	Force-Torque Sensor DAQ USB cable
12	Quad sensor DAQ USB
13	Quad USB hookup cable
14	USB extension cable plugged into hub output
15	Following items are plugged into Force-Torque PS box
16	D-sub cable plugged into rear
17	12V power cable plugged into rear
18	Force-Torque sensor cable plugged into front
19	Following items are plugged into Quad Sensor DAQ
20	USB cable
21	Following items are plugged into Force-Torque Sensor DAQ
22	USB cable
23	Power cable
24	AC power extension cable plugged into power strip
25	AC power extension cable plugged into wall outlet
26	**Turn on power strip**
27	Verify system power-on status:
28	Power strip switch LED is on
29	All occupied ports on the USB hub are lit up blue
30	Power LED on Force-Torque sensor DAQ is on
31	Green LED on back of Force-Torque PS box is on
32	Allow sensor electronics at least 15 minutes to reach equilibrium temperature
33	**Set power supply voltage**
34	***Verify motor power cable is disconnected from Quad test rig***
35	Turn on power supply
36	Adjust voltage to 14.85V
37	Turn off power supply
38	**Connect the following cables to the quad test rig**
39	Motor power DC cable

40	Motor controller USB cable
41	Onboard sensor circular cable
42	Stepper motor leads
43	**Prepare computer software environment**
44	Plug in USB extension cable
45	Plug in Scanivalve network cable
46	Verify network connection
47	Start MC DAQ calibration tool
48	Verify the MC DAQ appears in the hardware list as “Dev0”
49	Open Quad Tunnel Test LabVIEW project
50	Open Quad Tunnel Test Controller LabVIEW simulation
51	Open MC-DAQ version of atisensor controller
52	Open modified scanivalve controller
53	**Test software environment**
54	Run scanivalve controller simulation
55	Send calibration command
56	Verify instrument reads 0 PSI differential pressure
57	Run F/T controller simulation
58	Verify simulation is reading Force/Torque values
59	Run Quad Tunnel Test simulation
60	Verify simulation is reading voltage and power values
61	**Power-on test**
62	Turn on motor power supply - verify supply LED reads ~14.85
63	Verify simulation is reading motor voltage
64	Wait for input voltage to settle
65	Adjust motor power supply until all motors read slightly over 14.8V
66	Tare motor power on simulation front panel
67	Test each motor independently by ramping each throttle up to 1700 PWM and back to 0
68	Verify motor RPM starts tracking once the throttle is over 1350 PWM
69	Turn off motor power supply
70	Stop simulations
71	**Calibrate Quad test rig position**
72	Use Tunnel control PC to command pitch and height adjustment
73	Calibrate force-balance pitch to horizontal
74	Tare pitch to 0 angle of attack
75	Measure and adjust rotor plane to target height
76	Input linear and rotation transformations into the F/T LabVIEW simulation

C.3. Post-Test Procedures

#	(04) Post-Test Procedures
1	Power off motor power supply
2	Power off wind tunnel fan
3	Power off wind tunnel linear drive and pitch mechanism
4	Stop all LabVIEW simulations
5	Power off external hardware power strip
6	Disconnect extension cable from power strip
7	Test rig hardware is now safe to handle
8	If necessary, remove test rig from tunnel following installation steps in reverse order

D. Pictures of Hardware

Test Vehicle - Front

Test Vehicle – Port Side

Test Vehicle - Rear

Tunnel Installation - Data Acquisition Hardware Pallet and Power Supply